USFOS

Verification

Manual
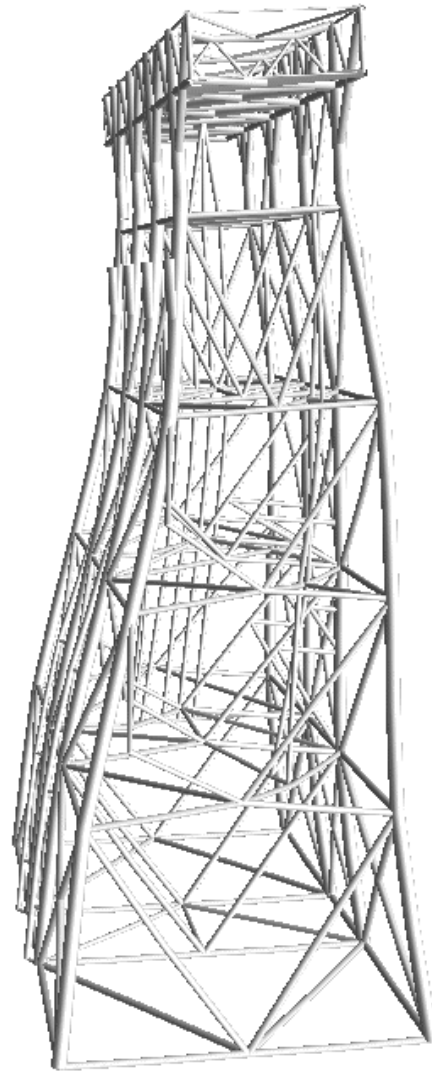
Contents

1 INTRODUCTION

The computer program system USFOS is an efficient tool for progressive collapse analysis of space framed structures.

The USFOS frame analysis includes both non-linear geometry and material behaviour.

USFOS allows for the same finite element discretization as used in elastic analyses. Only minor modifications of the data set are necessary.

The purpose of the USFOS analysis module, its capabilities and theoretical basis are described in the USFOS Theory Manual /1/.

The practical use of the analysis program is described in the USFOS User's Manual /2/.

This part of the USFOS documentation concerns the verification of the program. The basic features of the program are described, followed by a short presentation of the theoretical basis. In Section 2.1, the implemented element formulations are verified for the simple case of linear material behaviour. The performance of plasticity model is verified in Section 2.3. Chapters 3-9 document the various special features. Chapter 11 focuses on verification of numerical procedures and is followed by a section containing various verification examples of system collapse analysis.

The main purpose of this manual is, besides the verification of all major aspects of the analysis program USFOS, to serve as an example manual where the user may look up worked examples and recommended values of various input parameters.

Each verification example contains a brief description of the problem and a data listing of the USFOS control input file. USFOS analysis results are verified against independent available sources such as analytical predictions, alternative FEM solutions or experimental results from large-scale tests.

2 ELEMENT VERIFICATION

2.1 BEAM ELEMENT

2.1.1 Elastic behaviour, simply supported elastic beam

The beam element in USFOS accounts for large displacements and rotations. This verification example evaluates the representation of membrane effects when assuming linear elastic material behavior.

GEOMETRY AND LOADING

This example shows a simply supported beam, axially restrained at both ends, and subjected to uniformly distributed loading, as shown in Figure 2.1.1. The beam is analyzed with USFOS using two beam elements over the 500 mm span. The solution procedure used is the simple Euler-Cauchy incrementation procedure. Third-order polynomial deflection functions are used for the beam element.

RESPONSE

The load-displacement relationship at the beam midspan is shown in Figure 2.1.1 /4/. This clearly demonstrates a considerable stiffness increase due to membrane effects, which are mobilized as deflections increases. The response is observed to be in close agreement with the solution obtained analytically by Timoshenko /5/.
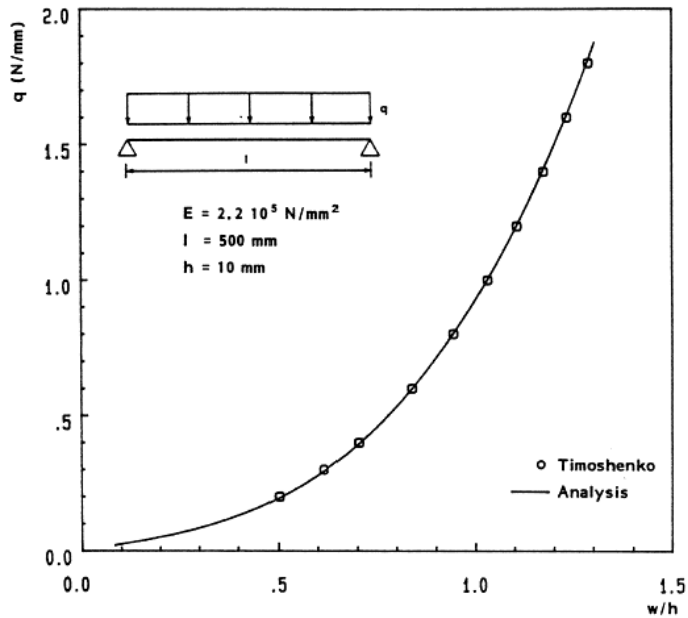
Figure 2-1 *Load-deflection relationship for axially restrained elastic beam*

```
HEAD      ELASTIC  BEAM  BENDING
          USFOS progressive collapse analysis
          SINTEF Structures and Concrete

'         inpri  outpri  termpri
CPRINT    1       2       1
'
'         epssol  gamstp  ifunc  pereul  ktrmax  dentsw  cmax  ifysw
CPROPAR  1.0E-20  0.02    2      0.05    5       0       999   0
'         kunfal  itmax   isol   koplas
          0       0       1      0
'
'         nloads  npostp  mxpstp   mxpdis
CUSFOS    10      10      1.00      0.10
'         lcomb   lfact   mxld   nstep    minstp
          1       0.1     2.0     75       0.001
'
'         ncnods
CNODES    1
'         nodex   idof    dfact
          3       2       1.
'         matno   E-mod   poiss    yield   density     term. expantion
MISOIEP   1      0.210E+12  0.3   0.330E+11  0.7850E+04    0.0

'         nodeno  ndof    dx dy dz rx ry rz
BNBCD     1       6       1  1  1  0  0  0
BNBCD     2       6       1  1  1  0  0  0
```

List 2.1.1   Listing of USFOS control input file

2.2 INELASTIC COLUMN BUCKLING

The ability to model column buckling is of major importance in order to simulate global collapse of space framed structures realistically. The present verification case documents the ability of USFOS to simulate column buckling including the influence of initial imperfections as well as material nonlinearities.

Figure 2.1.1 summarizes the theoretical basis for the elastic beam element stiffness relationship implemented in USFOS, including the Livesly stability functions /1/. As USFOS employs exact element displacement functions satisfying the governing differential equation, USFOS should predict the elastic buckling load for the three basic cases depitched in Figure 2.1.2. It is observed that singularity of the element equilibrium relationship, corresponding to structural instability, results in the exact Euler buckling formulas.

Examples:

$$k = \frac{2EJ}{\ell}\begin{bmatrix} 2\varphi_3 & \varphi_4 \\ \varphi_4 & 2\varphi_3 \end{bmatrix}$$

$$\det k = 0 \text{ for } \varphi_3 = \tfrac{1}{2}\varphi_4$$

$$P_{crit} = P_E$$

$$k = \frac{4EJ}{\ell} \cdot \varphi_3$$

$$\det k = 0 \text{ for } \varphi_3 = 0$$

$$P_{crit} = 2.04\, P_E$$

$$k = \frac{2EJ}{\ell^3}\begin{bmatrix} 6\varphi_5 & 3\ell\varphi_2 \\ 3\varphi_2 & 2\ell^2\varphi_3 \end{bmatrix}$$

$$\det k = 0 \text{ for } 12\varphi_5\varphi_3 = 9\varphi_2^2$$

$$P_{crit} = 0.25\, P_E$$

$$p = \frac{P}{P_E} = \frac{P\ell^2}{\pi^2 EI}$$

$$k = \frac{2EI}{\ell^3}\begin{bmatrix} 6\varphi_5 & -3\ell\varphi_2 & -6\varphi_5 & -3\ell\varphi_2 \\ -3\ell\varphi_2 & 2\ell^2\varphi_4 & 3\ell\varphi_2 & \ell^2\varphi_6 \\ -6\varphi_5 & 3\ell\varphi_2 & 6\varphi_5 & 3\ell\varphi_2 \\ -3\ell\varphi_2 & \ell^2\varphi_6 & 3\ell\varphi_2 & 2\ell^2\varphi_3 \end{bmatrix}$$
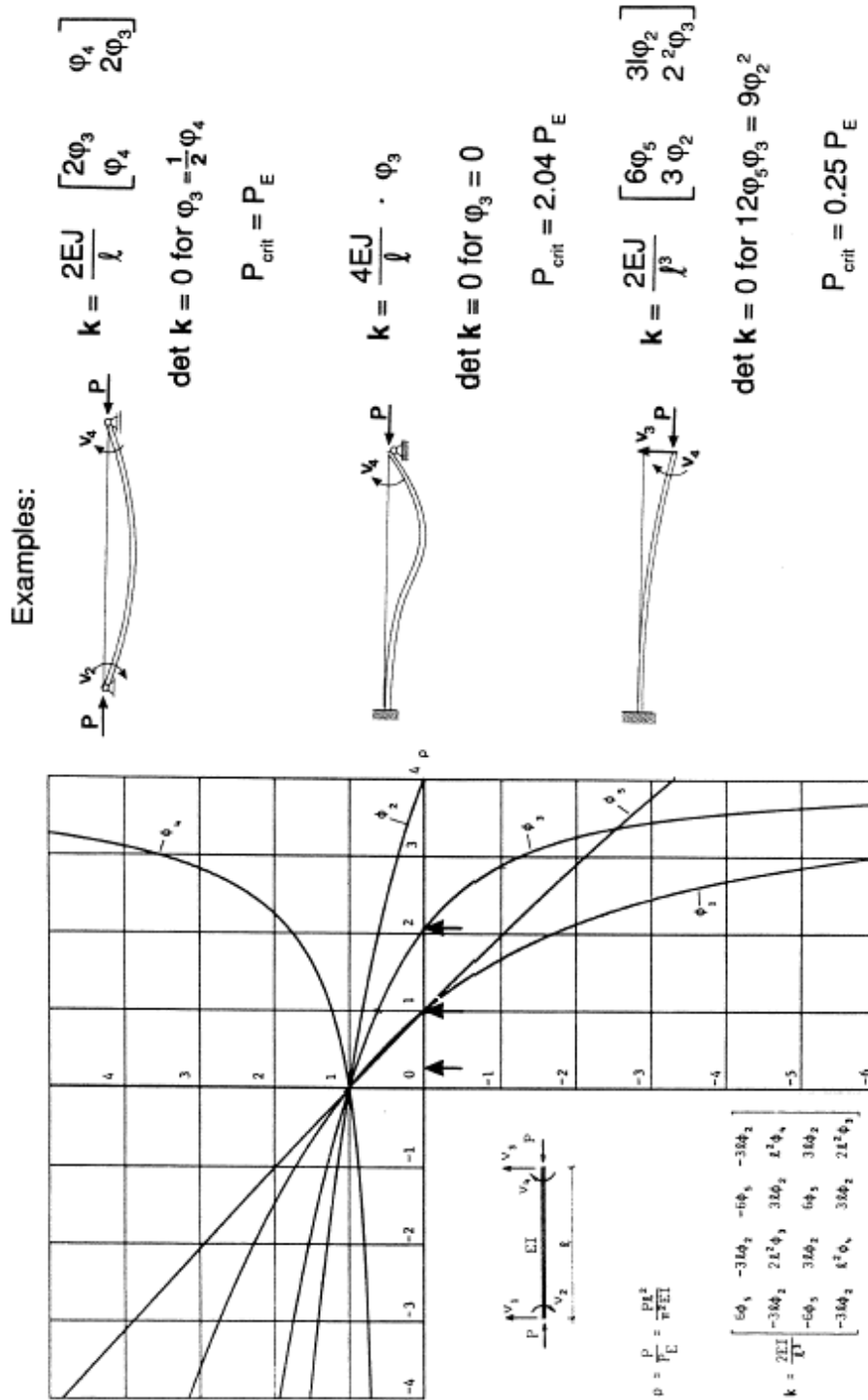
Figure 2.1.2   Elastic column buckling

GEOMETRY AND LOADING:

The case considered, shown in Figure 2.1.3, comprise an axially loaded pinned column for different values of slenderness and initial out-of-straightness. Cross sectional geometry and material properties are also given in Figure 2.1.3. Initial imperfections are chosen as a half sine wave for all cases.

In the analysis the simplified elastic-perfectly-plastic material model was used, and local buckling of the tube wall is excluded from the model.
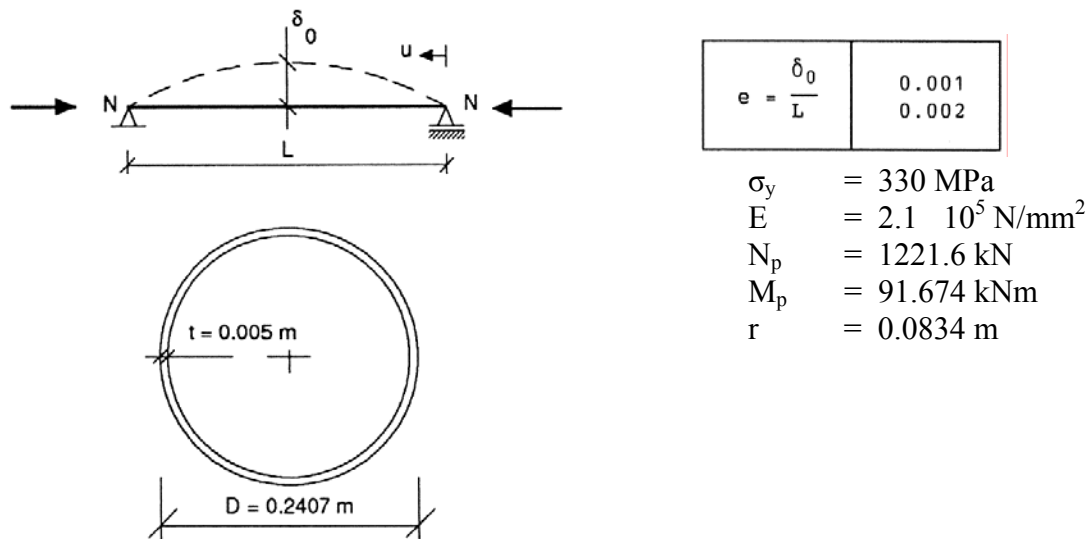

$e = \dfrac{\delta_0}{L}$	0.001
	0.002

σ_y = 330 MPa
E = 2.1 10^5 N/mm^2
N_p = 1221.6 kN
M_p = 91.674 kNm
r = 0.0834 m

Figure 2.1.3   Axially compressed columns with initial imperfections

The slenderness, defined by L/r, is varied by changing the column length. The column is in the FEM model idealized as one single beam element.

RESPONSE:

The results obtained by USFOS are summarized in Figure 2.1.4 and Figure 2.1.5. Figure 2.1.4 shows the axial load level versus a normalized axial displacement for variable initial imperfections.

The compressive strength of the column, represented by the peak of the load- displacement relationships, is compared to the Lehigh design curve /10/ in Figure 2.1.5. The buckling load, normalized with the yield load, is plotted versus the column reduced slenderness for the cases with initial imperfections equal to e = 0.001 and e = 0.002.

The numerical simulations trace the analytical predictions quite well. Usually members in a jacket structure have a reduced slenderness less than 1.0, and it is concluded that USFOS predicts the column buckling load accurately.
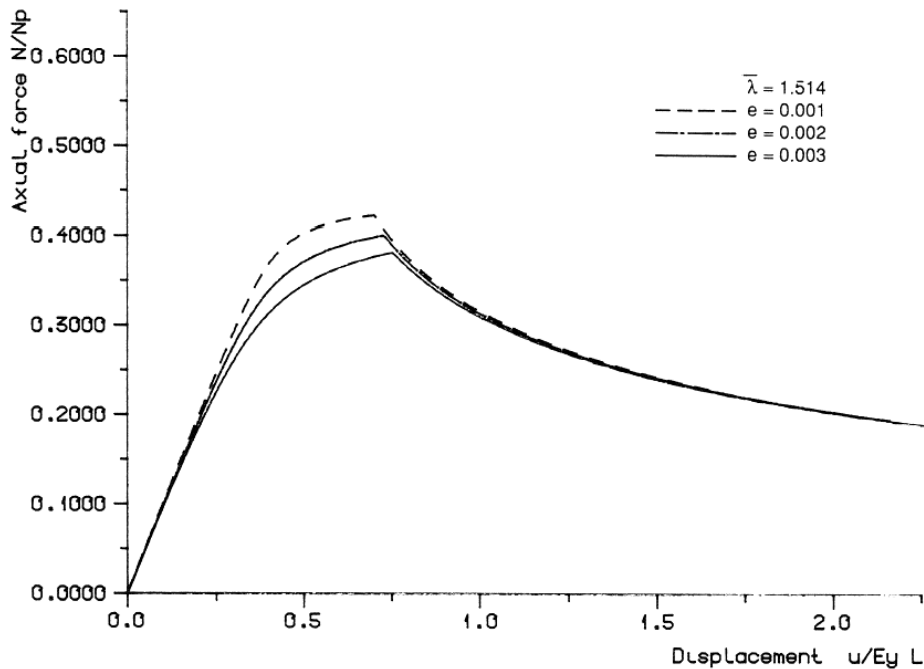

Figure 2.1.4   Pinned column load-displacement relationship

Figure 2.1.5   Pinned column buckling load

```
HEAD        ELASTO - PLASTIC  COLUMN  BUCKLING
            USFOS progressive collapse analysis
            SINTEF Structures and Concrete
'
'       inpri    outpri  termpri
CPRINT    1        2        1
'       epssol  gamstp  ifunc  pereul  ktrmax  dentsw  cmax  ifysw
CPROPAR 1.0E-20   0.3      2     0.01      5       0     1.2   1.0
'       nloads  npostp  mxpstp    mxpdis
CUSFOS    10      40     1.00      0.20
'       lcomb   lfact   mxld  nstep    minstp
          2      0.02    0.0   100      0.01
'       ncnods
CNODES    1
'       nodex    idof    dfact
          2        1       1.
'     impgroup impshape  angle   offset   dent1   dent2   dentmid
GIMPER    1        1       90     0.001     0.0     0.0     0.0
'       elnox  impgroup
GELIMP    1        1
'       matno   E-mod    poiss   yield    density
MISOIEP   1.   0.210E+12   0.3  0.330E+12  0.7850E+04
```

List 2.1.2   Listing of USFOS control input file

2.3 PLASTICITY MODEL VERIFICATION, CLAMPED BEAM WITH DISTRIBUTED TRANSVERSE LOADING

This section verifies the nonlinear material model implemented in USFOS. The basis of the bounding surface model is outlined in detail in Section 3 in /1/. The present formulation accounts for gradual plastification as well as strain hardening.

GEOMETRY AND LOADING

This example considers a 10 meter long beam clamped at both supported ends as shown in Figure 2.1.6. Geometrical data and material properties are also given in Figure 2.1.6. A thin walled tubular cross section with a D/t ratio equal to 48 is used. Local wall buckling is neglected. The beam is subjected to a vertical load uniformly distributed along the beam. The loads are gradually increased according to the history defined in analysis control input file, see List 2.1.3.

The beam in Figure 2.1.6 is modeled as two equally sized elements, allowing for the formulation of totally 5 plastic hinges.

The analyses are performed using both the simple elastic-perfectly-plastic material model (ifysw=1) as well as the bounding surface model including gradual plastification and material hardening (ifysw=0). For the tube cross section, the yield surface (yield criterion) and bounding surface (capactiy criterion) are defined by:

$$F_y(\ N, M_x, M_y, M_z, \beta_i, z_y\ ) = (1 - m_x^2\ )^{1/2} \cdot \cos\left(\frac{\pi}{2} \cdot \frac{n}{(1 - m_x^2\ )^{1/2}} \right) - (\ m_y^2 + m_z^2\ )^{1/2} = 0$$

where n, m_x, m_y and m_z are defined by:

$$n = \frac{N - \beta_1}{N_p\ z_y}, \quad m_x = \frac{M_x - \beta_4}{M_{px}\ z_y}, \quad m_y = \frac{M_y - \beta_5}{M_{py}\ z_y}, \quad m_z = \frac{M_z - \beta_6}{M_{pz}\ z_y}$$

$$F_b(\ N, M_x, M_y, M_z, \alpha_i, z_y\ ) = (1 - m_x^2\ )^{1/2} \cdot \cos\left(\frac{\pi}{2} \cdot \frac{n}{(1 - m_x^2\ )^{1/2}} \right) - (\ m_y^2 + m_z^2\ )^{1/2} = 0$$

where n, m_x, m_y and m_z are defined by:

$$n = \frac{N - \alpha_1}{N_p\ z_y}, \quad m_x = \frac{M_x - \alpha_4}{M_{px}\ z_y}, \quad m_y = \frac{M_y - \alpha_5}{M_{py}\ z_y}, \quad m_z = \frac{M_z - \alpha_6}{M_{pz}\ z_y}$$

In the present verification case the default value 0.79 of the yield surface size z_y is used and the bounding surface size is always equal to unity. For the elastic-perfectly-plastic model the two surfaces are coincident with a size equal to unity.

For the present example the plastic parameters are selected the same for each direction in force space. The transition parameter is selected to 0.25 and the kinematic hardening parameter c is chosen to 0.015. These parameters determines the plastic hardening matrix characteristics, which for the one dimensional case may be written as:

$$\bar{k}^h = \left(c + a \, \frac{\delta}{\delta_\in - \delta} \right) k^E$$

Here δ denotes the distance between the force point on the yield surface and the corresponding conjugate point situated on the bounding surface, see /1/.

Generally, the material parameters defining the model properties should be calibrated for the actual cross section based on experimentally measured force- displacement relationships for the different cross sections /4/, /6/.

The beam element is substituted by a pure membrane element at a axial force equal to 99 % of the beam axial plastic capacity.
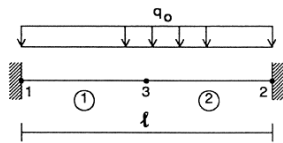
Beam model

Beam length	ℓ	=	10.000 m
Pipe diameter	D	=	0.2407 m
Pipe thickness	t	=	0.005 m
Yield stress	σ_y	=	330 MPa
Youngs modulus	E	=	$2.1 \, 10^5$ MPa
Initial load	q_0	=	10 kN/m
Area	A	=	$3.702 \, 10^{-2}$ m²
Moment of inertia	I	=	$2.572 \, 10^{-5}$ m⁴
Sectional modulus	W_p	=	$2.778 \, 10^{-4}$ m³
Axial force capacity	N_p	=	1221.6 kN
Bending moment capacity	M_p	=	91.674 kNm
Yield load (linear theory)	q_y	=	$12/\ell^2 \, M_p = 1.100 \cdot q_0$
Mechanism load (linear theory)	q_y	=	$16/\ell^2 \, M_p = 1.467 \cdot q_0$

Figure 2.1.6   Clamped beam with distributed load

RESPONSE

The midspan deflection is plotted versus load level in Figure 2.1.7 for the two different cases of material behavior. The dotted line, corresponding to the elastic-perfectly-plastic case, indicates that sharp edges occur in the response curve as a plastic hinge is introduced. This corresponds to sudden changes in the overall stiffness.

Analytical solutions give plastic hinges at the element ends and element midspan at load level 1.1 qo and 1.467 qo, respectively. These values correlate well with the results in Figure 2.1.7. At position 3 in the plot, plastic hinges are introduced at each of the elements middle sections and at this stage 5 plastic hinges have developed. During further loading the bending moment decreases and the membrane action increases.

The load-displacement relationship corresponding to the bounding surface model is shown by the solid line in Figure 2.1.7. This shows a more realistic response behavior than the simplified case. It is observed that when taking into account the gradual plastification of the cross section, the global response becomes smoother at the stage when a plastic hinge is introduced.

Furthermore, the overall effect of strain hardening is seen to increase the load-carrying capacity compared to the elastic-perfectly-plastic case.
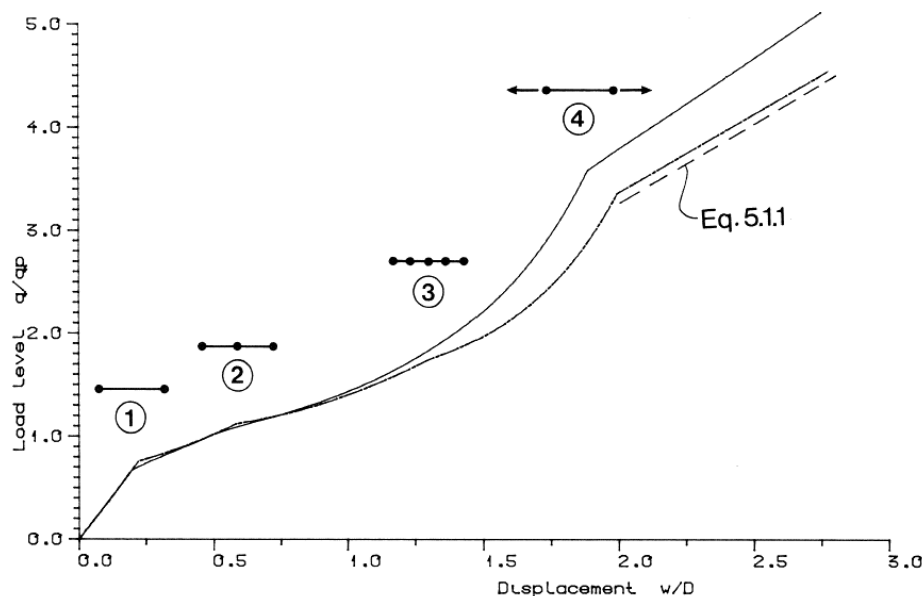

Figure 2.1.7   Beam response

The behaviour of the bounding surface model during loading is depicted in Figure 2.1.8. Here the force state defined by the bending moment and axial force at a cross section located near to one of the beam supports is examined. Figure 2.1.8 (a) shows the initial (unloaded) position of the yield surface and the bounding surface.

The force path, defining the current state of forces at the cross section, is also plotted. A plastic hinge is introduced when the yield surface is reached. This corresponds to state 1 in Figure 2.1.7. As seen the beam carries the external load mainly by bending and the axial forces are small.

When the external load is increased, Figure 2.1.8 (b) shows that the yield surface translates with the force state, and approaches the bounding surface.

The bounding surface also moves, but at a much smaller rate. At this stage, the plastic stiffness depends on the normalized distance between the surfaces as discussed above. As seen from Figure 2.1.8 (b) the force point translates mainly along the axial force axis. This reflects the increasing membrane action of the beam.

In Figure 2.1.8 (c) the yield surface has reached the bounding surface, which corresponds to full plastification of the cross section. From this state, the bounding surface and the yield surface translates in the force space at the same rate.

As seen, the force point has during loading moved along the bounding surface. At the final state the axial force approach the cross sectional plastic capacity in pure tension and a membrane element is introduced.
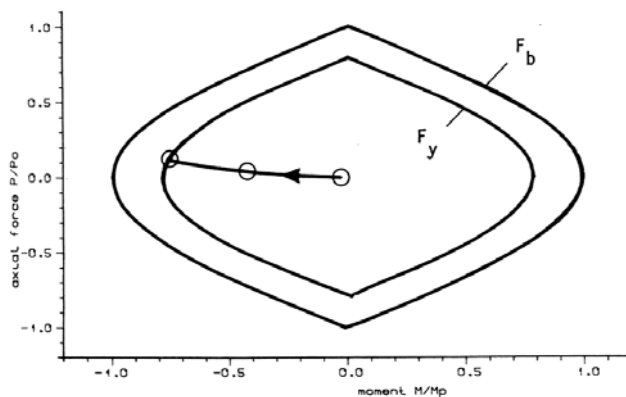

Figure 2.1.8a   Behaviour of bounding surface model
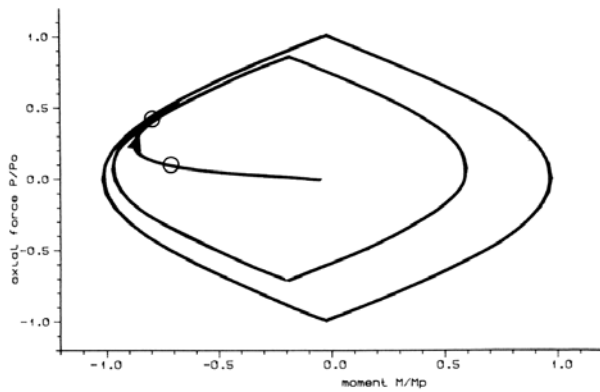
Figure 2.1.8b   Behaviour of bounding surface model
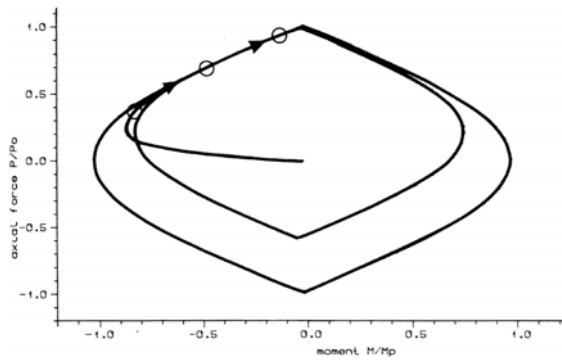

Figure 2.1.8c   Behaviour of bounding surface model

```
HEAD        ELASTO - PLASTIC  BEAM  BENDING
        USFOS progressive collapse analysis
        SINTEF Structures and Concrete

'       epssol  gamstp   ifunc  pereul  ktrmax  dentsw  cmax  ifysw
CPROPAR 1.0E-20  0.02      2     0.05       5       0    999     0
'       kunfal  itmax    isol  koplas
          0       0        1      0


'       nloads  npostp  mxpstp  mxpdis
CUSFOS    10      10     1.00    0.10
'       lcomb    lfact   mxld  nstep  minstp
          1       0.1    7.5     75   0.001
'

'       ncnods
CNODES    1
'       nodex     idof  dfact
          3         2     1.
'

'       matno  E-mod poiss yield density    term. expantion
 MISOIEP   1  0.210E+12  0.3  0.330E+09  0.7850E+04  0.0 0.015 0.25
'

'       geono   z-yield
 GBOUND    1      0.79
```

List 2.1.3   Listing of USFOS control input file

2.4 NONLINEAR SPRING ELEMENT

USFOS provides both 1 and 2 noded nonlinear springs. The MREF material card is used to specify material properties for the spring in both cases. Properties in the 6 DOF's are specified by referring to other material input, the MISOPL card. References to material number 0 means that the element has no stiffness in the actual degree of freedom.

Input on the MISOPL card is material type (elastoplastic with kinematic hardening or nonlinear hyperelastic) and force - displacement curve.

If SESAM element type 18 refer to a MREF card, the element will be handled by USFOS as a nonlinear spring to ground. If SESAM element type 15 refer to a MREF card, the element will be handled as a 2 node nonlinear spring.

2.4.1 Spring to ground(1 node)

The jackup-structure shown in Figure 2.2.1 is used to verify the nonlinear spring to ground element. Each leg is supplied with a nonlinear spring-to-ground. The USFOS control file is shown in List 2.2.1

As seen in List 2.2.1, only the first three DOF's are given material properties. The rotational DOF's will have zero stiffness in this example. Spring characteristics used for horizontal and vertical element loading are shown in Figure 2-2.
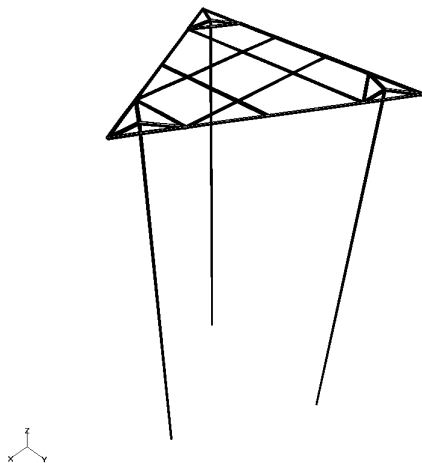

Figure 2-2 JackUp structure used in the examples

```
HEAD                        JACK-UP Model
                    USFOS Progressive Collapse Analysis
                       SINTEF Structures and Concrete
'
'        nloads   npostp   mxpstp   mxpdis
CUSFOS    5        250     0.001     1.00
'         lcomb    lfact    mxld     nstep     minstp
          1       10.0     75.0      100      0.001
          3        0.5     50.0      100      0.001
          3       -0.5    -50.0      100      0.001
          3        0.5     70.0      300       0.001
'
'        ncnods
CNODES    1
'         nodex   idof    dfact
          51       1       1
'
'     matno E-mod       poiss   yield   density          therm. exp.
MISOIEP  1  0.21E+6     0.3     687     0.49069000E-01    0.12E-4
MISOIEP  2  0.21E+6     0.3     687     0.10000003E-01    0.12E-4
'
'        Material properties for nonlinear springs
'        ----------------------------------------
'     matno       refx   refy   refz   refrx   refry  refrz
MREF  50          1000   1000   3000    0       0      0
'
'        matno   matyp
MISOPL 3000      4      0      0
          0      0      0      0
          6
       -265.91   -3.8
       -175.0    -1.8
       -100.0    -0.15
        100.0     0.15
        175.0     1.8
        265.91    3.8
'        matno   matyp
MISOPL 1000      4      0      0
          0      0      0      0
          6
        -11.0    -8.6
         -9.0    -3.0
         -8.0    -0.20
          8.0     0.20
          9.0     3.0
         11.0     8.6
```

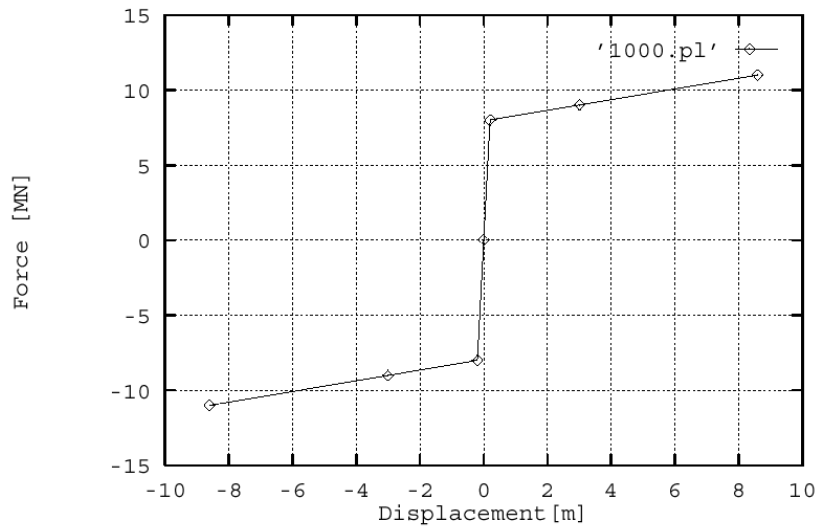*List 2.2.1 Listing of USFOS control input file*

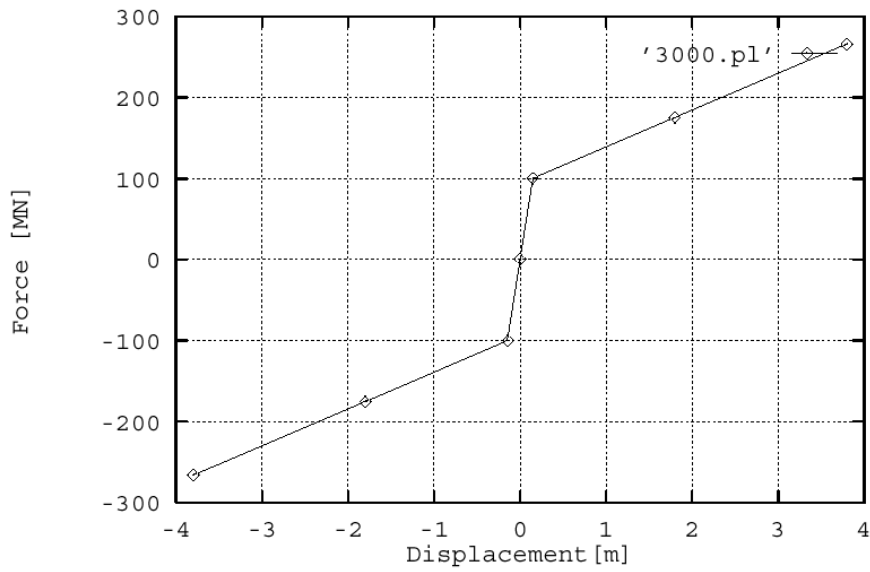*Figure 2.2.2-3 Spring characteristic for horizontal loading.*

Figure 2.2.2-4   Spring characteristic for vertical loading.

2.4.2   Material type 4, elastoplastic with kinematic hardening

GEOMETRY AND LOADING

The Jackup structure is preloaded with a gravity load. Then a horizontal node load is applied in top of the front leg. This load is reversed twice to investigate the elastoplastic behaviour of the element.

The analysis show that the element reaction forces follow the specified spring characteristics, and that the applied loads at any time equals the sum of the global reaction forces. In Figure 2.2.5 the element x-force is plotted against the element x-displacement for element 1100.

As seen from Figure 2.2.5, in the X-dof the element is first plastified and then undergoes elastic unloading when the global load is reversed. The element remains elastic in this dof until the shift in element force equals the force range of the elastic area in the actual spring characteristic.

From Figure 2.2.6, we see that in the Z-dof the element remains elastic and follow the elastic part of the spring characteristic throughout the analysis.
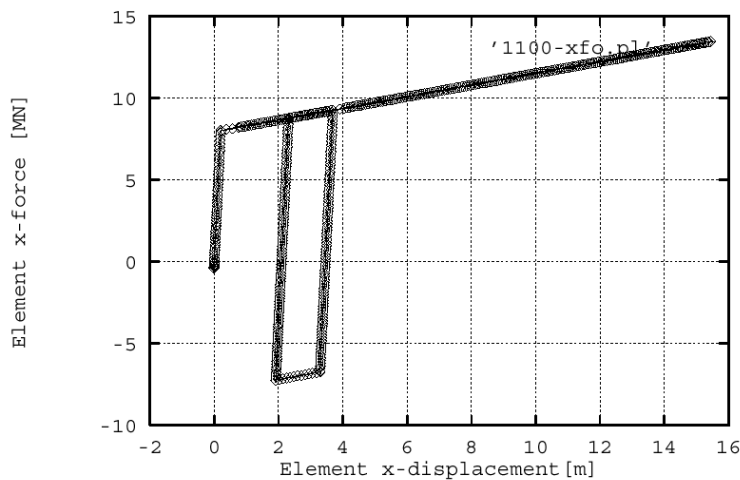
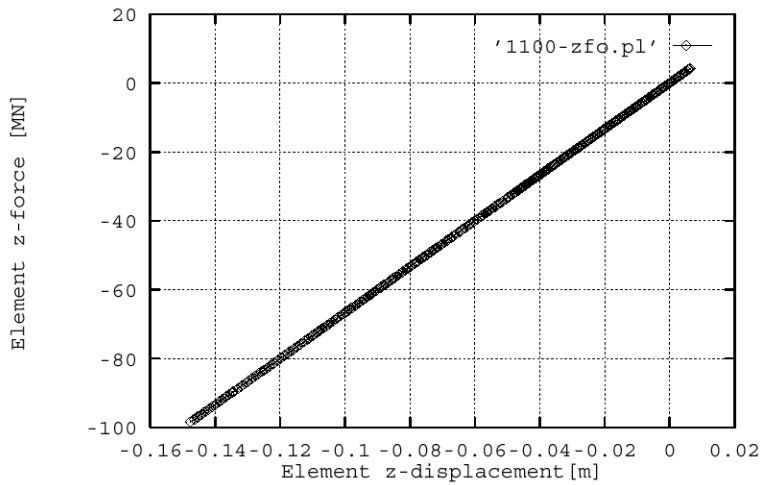Figure 2.2.2-5 X-force versus X-displacement for element 1100.

Figure 2.2.2-6 Z-force versus Z-displacement for element 1100.

2.4.3 Material type 2, nonlinear hyperelastic

The results are shown in Figure 2.2.7 and Figure 2.2.7. As seen from the plots, the force-displacement curves follow the specified spring characteristic throughout the analysis.

There is no change in stiffness caused by unloading when the load is reversed.
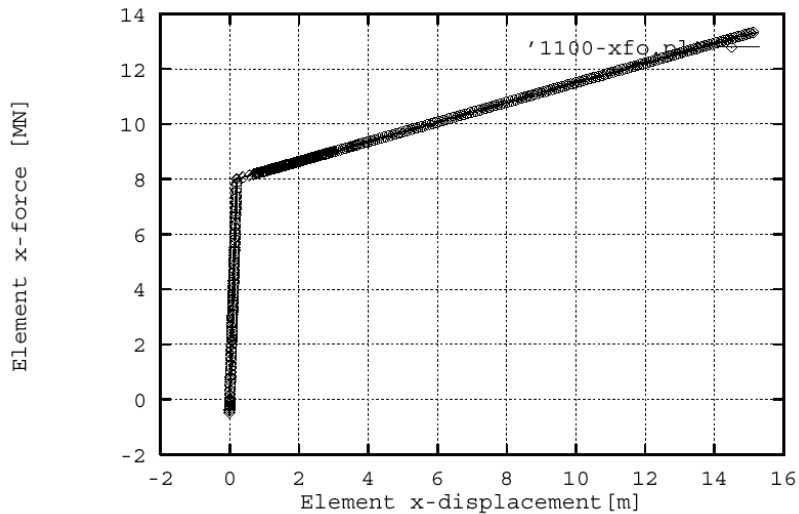

Figure 2.2.2-7 X-force versus X-displacement for element 1100.
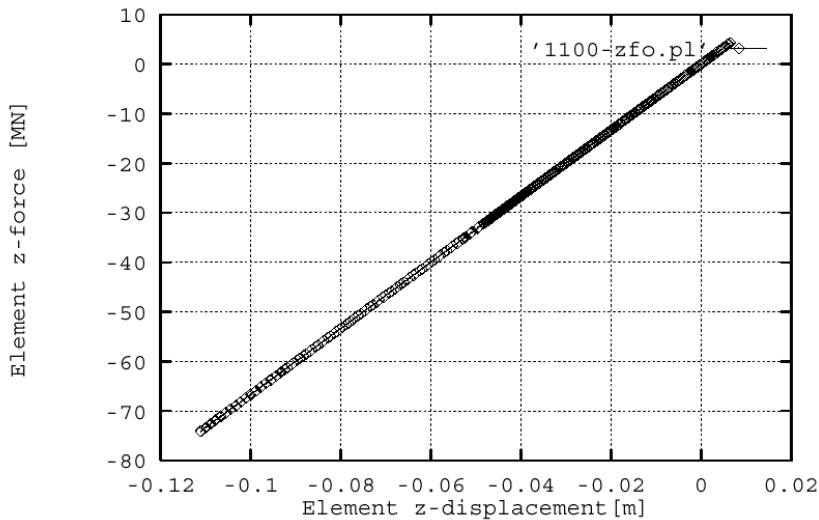
Figure 2.2.2-8   Z-force versus Z-displacement for element 1100.

2.4.4   2-noded nonlinear spring

This version of the element may be used between nodes within a structure. The element should be used with care, as there is no coupling between the dofs of the element. The element is verified as an axial spring.
The structure shown in fig.. is used in this example. A 2-noded spring element is connected to the deck structure in front of the first leg. The free node of the spring is fixed in all dofs except the axial one. The spring characteristic is shown in ..
A horizontal load is applied through this element.

3   JOINT BEHAVIOUR

In this section the variable joint features implemented in USFOS are verified.

3.1   TUBULAR JOINT FLEXIBILITY

In this section the performance of the shell property element is verified. The element is implemented in USFOS to model tubular joint flexibility. This element type is automatically generated by the program when the user specify the nodal flexibility option in the analysis control file.

GEOMETRY AND LOADING:
Figure 3.1.1a) shows a simple space framed structure which consists of one center cord member and two bracing members /7/. The geometry and dimensions of the structure is given in Figure 3.1.1. The system is subjected to a concentrated load acting horizontally at the free end of one of the bracing members. The structure is modelled with 4 beam elements and one shell property element as illustrated in Figure 3.1.1b).


```
Data for the frame:

Total chord length: 20.000 m
Brace length       : 10.000 m
Chord diameter     :  1.000 m
Chord thickness    :  0.025 m
Brace diameter     :  0.670 m
Brace thickness    :  0.025 m
```
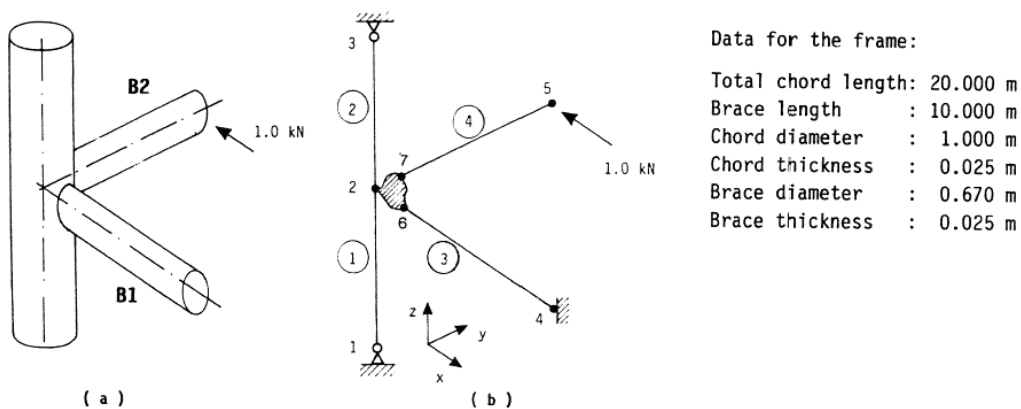
Figure 3.1.1   Three-dimensional frame structure with joint flexibility

RESPONSE

The forces acting on the shell property element is shown in Figure 3.1.2a) for the case when node 4 is free. The forces satisfy the equilibrium conditions.
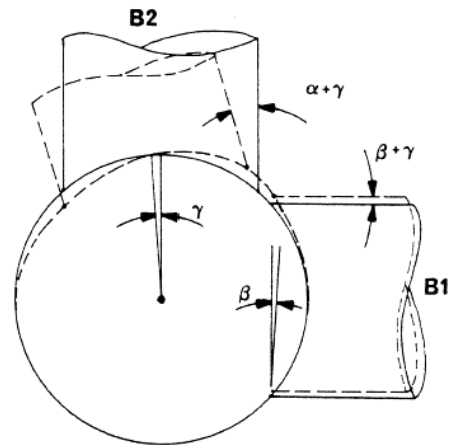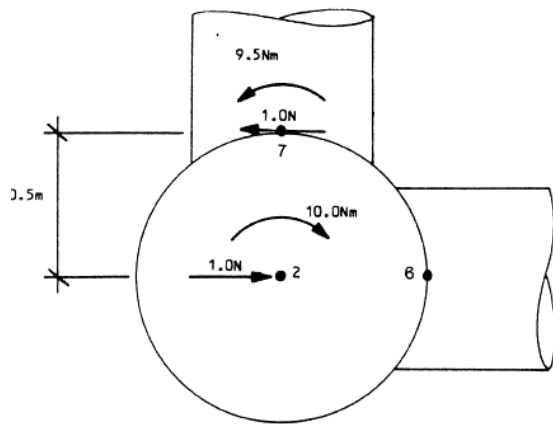
Figure 3.1.2a) Forces acting on the   b)   Rotations of the two bracing
            shell property element   members
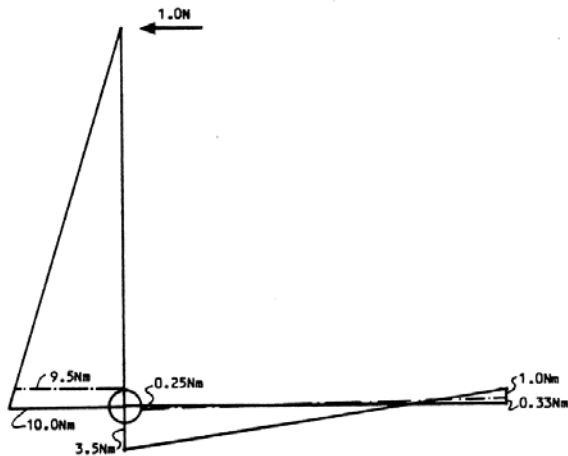

Figure 3.1.3   Moment distribution at tubular joint due to shell element flexibility

To examine the behaviour of the joint flexibility option, the structural system has been analyzed both with and without the use of this option. For this case node 4 is fixed, see Figure 3.1.1a).

For the conventional modelling of the system, the two braces are connected to the cord at the centre node 2. The resulting moment diagram for this case is shown with solid lines in Figure 3.1.3 /7/.

The corresponding bending moment with the shell property element, is shown by dotted lines. A dramatic change in moment is observed for brace element no 3 at the connection to the cord. This may be explained by considering the local deformation of the cord as shown in Figure 3.1.2b). Here γ denotes the torsional rotation of the cord while α and β denotes the local rotation of brace B2 and brace B1 due to shell deformation.

The local rotation of B1 is smaller, but has the opposite direction of the rotation of B2. The total rotation of B2 is $\alpha + \gamma$ while the total rotation of B1 is $\beta + \gamma = 0$ as illustrated in Figure 3.1.2b). This displacement state, strongly influenced by local wall deformations, results in negligible moments in brace B1.

```
HEAD          FRAME -  NODAL FLEXIBILITY TEST
              USFOS progressive collapse analysis
              SINTEF Structures and Concrete
'
'         inpri   outpri  termpri
CPRINT      1      2      1

'         epssol  gamstp  ifunc  pereul  ktrmax  dentsw  cmax  ifysw
CPROPAR  1.0E-20  0.10     2     0.05      5       0      1.2    0
'         kunfal   itmax   isol   koplas
            0        0       1        0
'
'         nloads   npostp  mxpstp    mxpdis
CUSFOS     10       100     1.00      0.20
'         lcomb    lfact   mxld      nstep      minstp
            2       0.2      0        100        0.01
'
'         ncnods
CNODES      1
'         nodex    idof     dfact
            2        1       1.
'
'         matno E-mod     poiss  yield    density  term.expantion
'
'          C1    A1  C2 A2  C3 A3 C4 A4 C5  A5    C6      A6
MISOIEP    1    0.210E+12 0.3   0.330E+09 0.7850E+04 0.0 0.015  0.25
'
'         geono      z-yield
GBOUND      1             0.79
SHELL       2    1   2
```

List 3.1.1   Listing of USFOS control input file

4   SOIL-STRUCTURE INTERACTION

4.1   NONLINEAR JACKUP FOUNDATION

In this section the nonlinear jackup foundation element is verified.The element is an one-node element, and becomes active if the MSPUD card is used instead of the MGSPRING or the MREF card in connection with element type 18.

GEOMETRY AND LOADING:
The verification example used is a three-legged jackup structure. The height of the structure is 140 m, the distance between the legs are 62 m. The legs are modelled as general beams with equivalent stiffness according to /15/. Loads applied to the structure are gravity load and a horizontal load in the node connecting the front leg to the deck structure, see Figure 4-1. The USFOS control file is given in List 4.1.1.
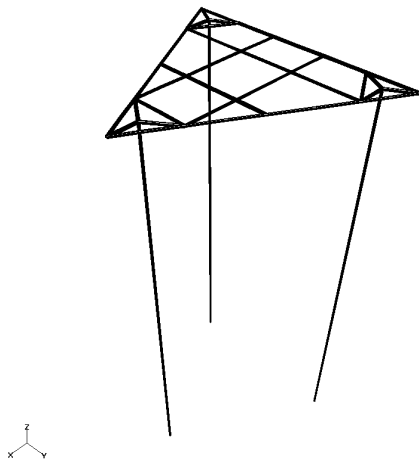

Figure 4-1 Jackup structure used in the examples

```
HEAD                         JACK-UP Model
                  USFOS Progressive Collapse Analysis
                    SINTEF Structures and Concrete
CITER
'         nloads   npostp   mxpstp   mxpdis
CUSFOS    5        250      0.001    1.00
'         lcomb    lfact     mxld      nstep      minstp
          1        1.0      1.0        10         0.001
          3        0.4      20.0       100        0.001
          3        0.2      50.0       200        0.001
'
'         ncnods
CNODES    1
'         nodex    idof    dfact
          51       1       1
'
'      matno E-mod       poiss    yield    density             therm. exp.
MISOIEP  1  0.21E+6      0.3      687      0.49069000E-01      0.12E-4
MISOIEP  2  0.21E+6      0.3      687      0.10000003E-01      0.12E-4
'
' SPUDCAN MATERIAL PARAMETERS :
MSPUD
' Mat_No |R_tot |Apex_ang |E_u_W   |Fr_ang |Cohe  |Pois    |Pre_L
   50     8.5    86.0      .01       35.0    0.0    0.25     175
'  |Gv    |Gh    |Gr      |YFSW  |C8
   40     40     26       0      1.0
```

List 4.1.1   Listing of USFOS control input file.

RESPONSE:

Calculation of effective radius

The effective radius of the spudcan is an important parameter giving the elastic stiffness of the spudcan. R_e is a function of the spudcan geometry and soil parameters. According to /xx/ R_e is given as

$R_e = d \tan \beta$

d is given from

$$Q_v = K_{q\gamma} \, \bar{\gamma} \, d^3 + K_c \, c \, d^2$$

$$K_{q\gamma} = (0.45 \sqrt{\pi} \, (\, N_q - 1) \tan \phi \, \tan \beta + \frac{N_q}{3} (1 + \sin \phi \,)) \, \pi \tan^2 \beta$$

$$K_c = \pi \tan^2 \beta \cot \phi \, ((1 + \sin \phi \,) N_q - 1)$$

$$N_q = e^{\pi \tan \phi} \tan^2 (\, 45^0 + \phi/2 \,)$$

β	=	Apex angle
φ	=	Friction angle
c	=	Cohesion
γ	=	Effective unit weight
Q_v	=	Vertical preload

With the input parameters given, the equations give R_e = 6.1339 m.

USFOS gives the same.

Nonlinear behaviour, the default model

This model is according to H. van Langen, Shell Research . It has both a yield function and a separate plastic potential. With this model a smooth transition between elastic and fully plastic behavior is obtained. The plastic potential enable us to use non-associated flow rule.

The yield function is given as

$$\Gamma = f\,(V, H, M, V_0, \Theta_P\,) = f_e + (\,f_u - f_e\,)\,G$$

G is a function of plastic rotation θ_p, zero plastic rotation gives $f = f_e$, if there is no plastic capacity left, $f = f_u$.

$$f_e = \sqrt{\left(\frac{M}{c_1 M_0}\right)^2 + \left(\frac{H}{H_0}\right)^2} - c_2\left(\frac{V}{V_0}\right)\left(1 - \left(\frac{V}{V_0}\right)^{c_3}\right)$$

$$f_u = \sqrt{\left(\frac{M}{c_4 M_0}\right)^2 + \left(\frac{H}{H_0}\right)^2} - c_5\left(\frac{V}{V_0}\right)\left(1 - \left(\frac{V}{V_0}\right)^{c_6}\right)$$

V_0= vertical capacity (pre-load); $H_0 = V_0$; $M_0 = V_0 D_{eff}$
$c_1 = 0.3$; $c_2 = 0.5$; $c_3 = 1.0$; $c_4 = 0.625$; $c_5 = 0.48$; $c_6 = 1.0$; $c_7 = 1.4$
Using f_u and solving for $M = 0$, one finds that the surface is described by

$$H = 0.48\left(V - \frac{V^2}{V_0}\right)$$

Maximum horizontal base shear capacity is then given for $V = 0.5\,V_0$, $H_{Max} = 0.12 V_0$.
Solving for $H = 0$, one finds that the surface is described by

$$M = 0.6\,R_e\left(V - \frac{V^2}{V_0}\right)$$

Maximum overturning moment capacity is found for $V = 0.5\,V_0$, $M_{Max} = 0.15\,R_e V_0$.
In the example used, $V_0 = 175$ MN. With the given input R_e becomes 6.134 m. In Figure 4.1. global load versus global displacement is plotted.

The vertical load in element 3300 versus global load is plotted in Figure 4-3.
First yield occurred in spudcan-element 3300, at a global load of 5.55 MN. At this time the horizontal base shear load in this element is 2.973 MN, the vertical load is 88.33 MN and the overturning moment load is 88.24 MNm.
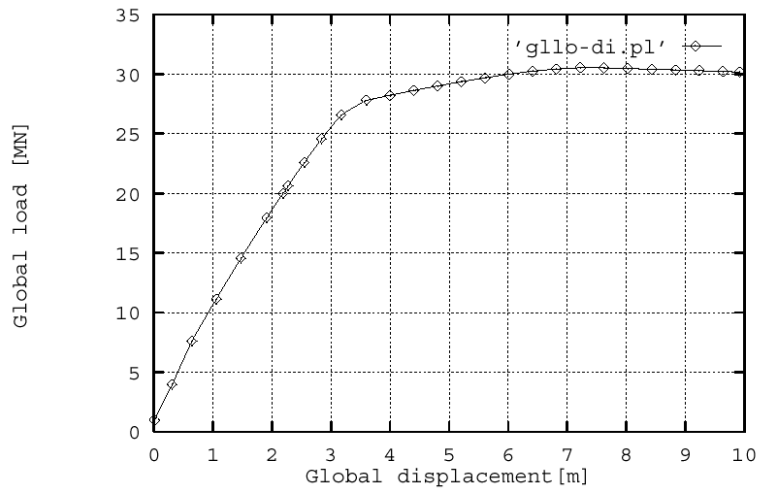
Figure 4-2 Global load versus global displacement
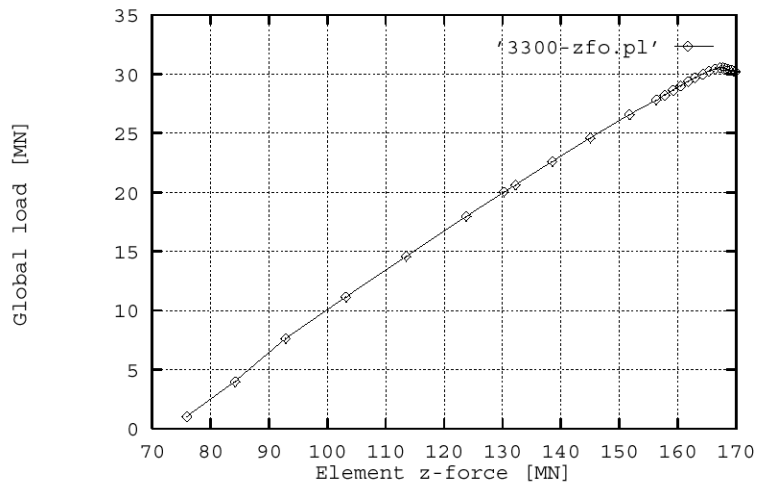
Figure 4-3 Vertical load in element 3300
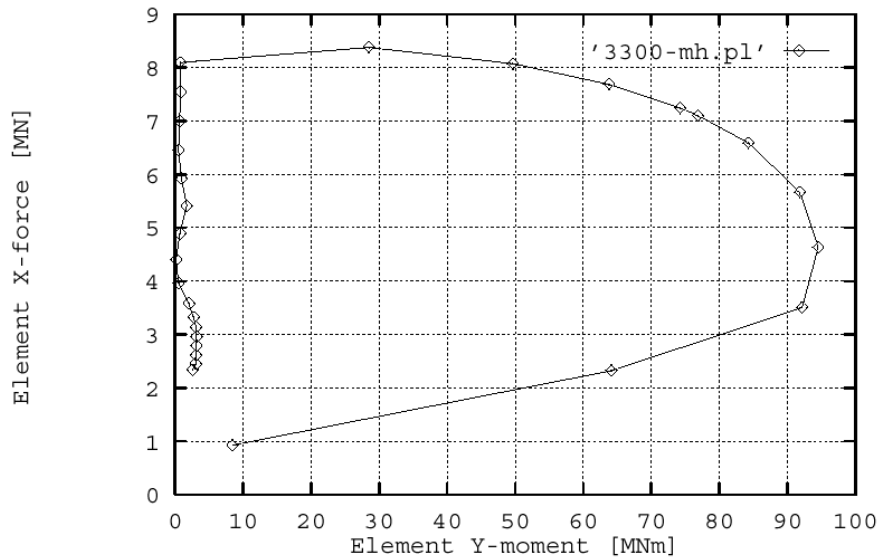
Figure 4-4 Y-moment versus X-force in element 3300.

From Figure 4-4 and Figure 4-5 we see that after the first yield, the vertical load and horizontal base shear load in the element continue to increase. The overturning moment load decreases. This continues until the overturning moment load in the element is zero, then the horizontal base shear load in the element decreases too.

Figure 4-5 Element Z-force versus element X-force in element 3300.

At the point where the overturning moment load reaches zero, the vertical load is 157 MN. Using Eqn. 4.1.1, one finds that this give a horizontal base shear capacity in the element of 8 MN. Figure 4.1.5 shows that USFOS give the same, the horizontal base shear load in the element is 8 MN at this point. Note that this point is where the global stiffness of the structure is most influenced.

Nonlinear behaviour, the optional model

This model is according to Geir Svanø, Sinetef Geotechnical Engineering /xx/. The model has a simple yield surface and no extra plastic potential. This means that it does not give a smooth transition from elastic to fully plastic behaviour. The yield function is given as

$$\Gamma = f(V,H,M,V_0) = \frac{H^{1.2}}{(0.135\,V_0\,)^{1.2}} + \frac{M^{1.2}}{(0.164\,R_e V_0\,)^{1.2}} - \sin(\frac{\pi V}{V_0}\,)^{0.84} = 0$$

Using f and solving for M = 0, one finds that the surface is described by

$$H = 0.135\,V_0 \left(\sin\left(\frac{\pi V}{V_0}\right) \right)^{0.7}$$

Maximum horizontal base shear capacity is then given for $V = 0.5\,V_0$, $H_{Max} = 0.135 V_0$. Solving for
H = 0, one finds that the surface is described by

$$M = 0.164\,R_e V_0 \left(\sin\left(\frac{\pi V}{V_0}\right) \right)^{0.7}$$

Maximum overturning moment capacity is found for $V = 0.5\,V_0$, $M_{Max} = 0.164\,R_e V_0$.
Comparing with the default model, one sees that this model gives slightly higher maximum capacities.
The results of the example analyzed with the optional model are shown below.
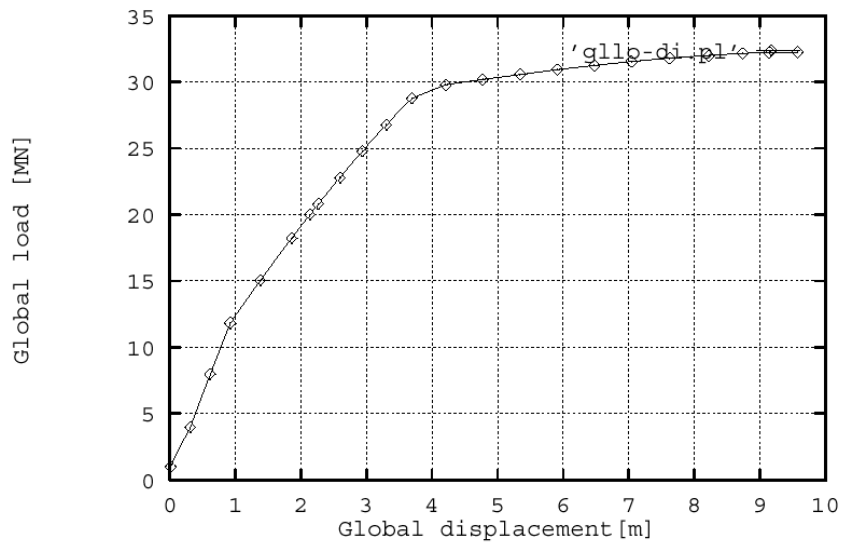
Figure 4-6 Global load versus global displacement
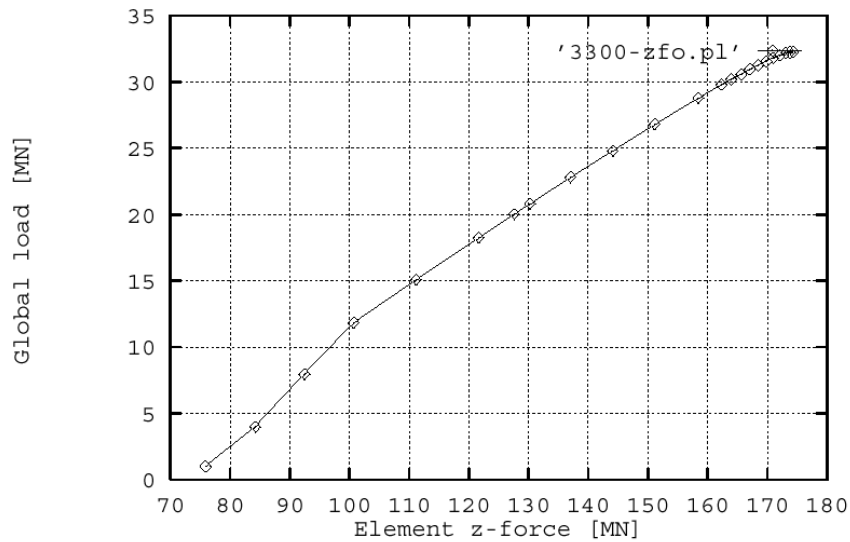
Figure 4-7 Vertical load in element 3300
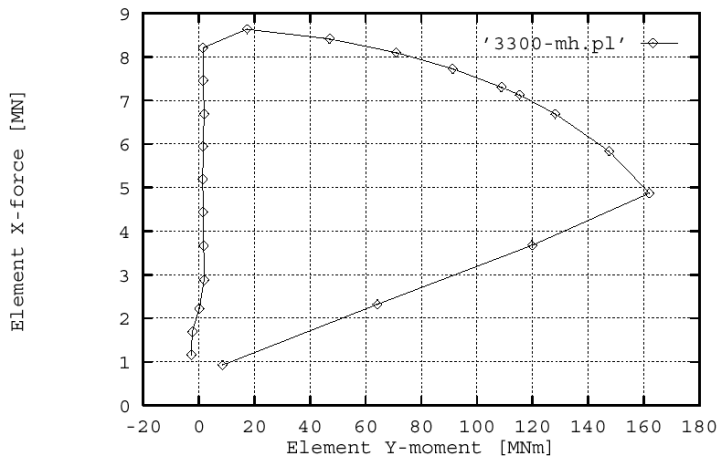
Figure 4-8 Y-moment versus X-force in element 3300

First yield occurred in spudcan-element 3300, at a global load of 11.1 MN. At this time the horizontal base shear load in this element is 4.72 MN, the vertical load is 99 MN and the overturning moment load is 163 MNm.
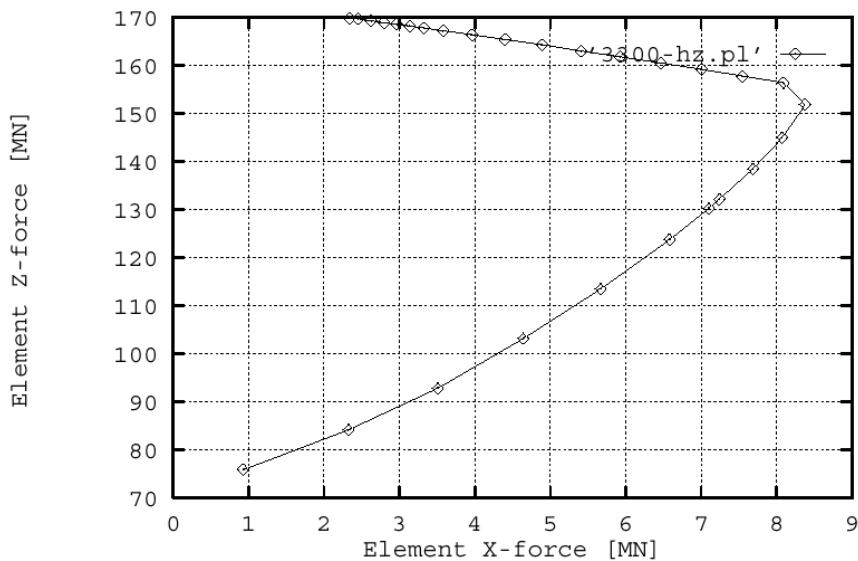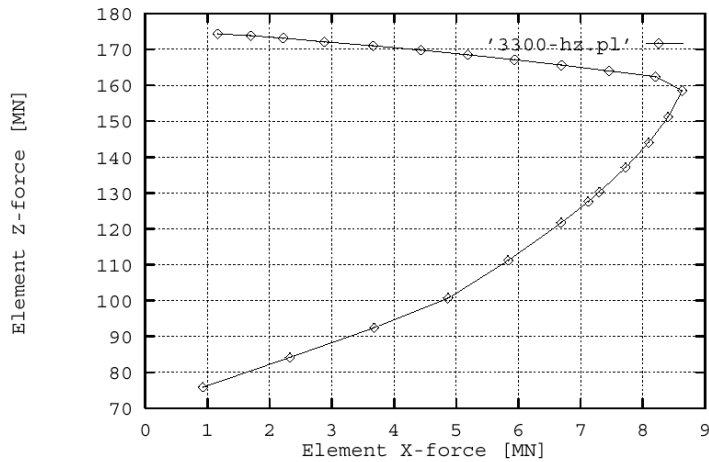

Figure 4-9 Element Z-force versus element X-force in element 3300

Comparing Figure 4-6 with Figure 4-2, one see that the global load - global displacement curve is almost the same for the two models. As seen from the equations above, the maximum capacities given from the two models are almost the same.

The real difference of the two models is the behavior after first yield. The default model gives a smoother transition from elastic to fully plastic behavior. This is best seen comparing Figure 4-4 and Figure 4-8.

5   LOCAL DAMAGE

5.1   DENTED TUBE MODEL

The dented tube model implemented in USFOS is in this example compared to experimental results obtained for pinned columns /8/.

THEORETICAL FORMULATION

In the present model it is assumed that the lateral distortion can be modelled as an initial deflection of the undamaged element whereas the dent is considered to affect only the plastic capacity of the cross section.
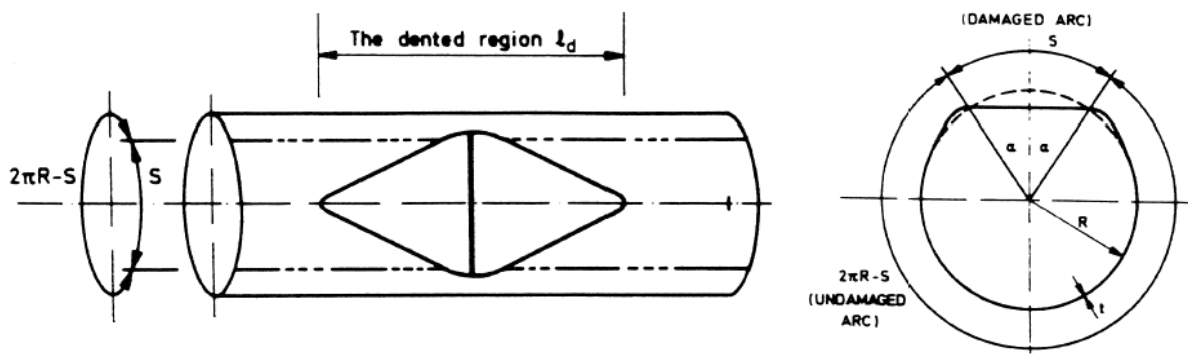
Figure 5.1.1   Dent idealization

The dented section is idealized as shown in Figure 5.1.1. The cross section consists of a dented part and an undamaged part. The load shared by the dented part is assumed to be limited by the force causing yielding at the middle of the dent. Further loading is carried by the undamaged part, alone.
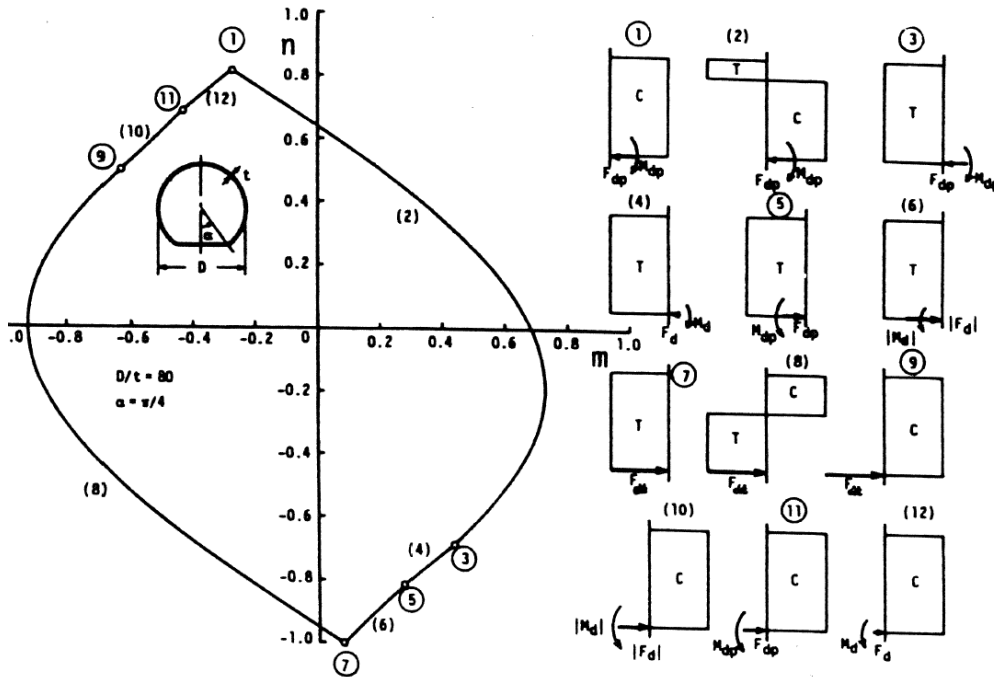
Figure 5.1.2   Plastic interaction curve for dented section

The total capacity of the cross section is expressed by the plastic interaction curve between axial force and bending moment, according to the dent depth and orientation. This is illustrated in Figure 5.1.2 for a dent located on the compressive side.

In the post-collapse range the dent will grow as the load increases, especially for D/t-ratios exceeding 50. On the basis of experiments an empirical dent growth function has been established.

$$D_{dg} = D_d + f(D(t) \cdot D \left[\left(1 - \frac{P}{P_p} \right)^a - \left(1 - \frac{P_u}{P_p} \right) \left(1 - \frac{P}{P_p} \right)^{a-1} \right]$$

where D_d = the initial depth of the dent
D_{dg} = depth of dent after ultimate load has been reached
$f(D/t)$ = D/t dependent function
P_p = the fully plastic axial load
  = $t\sigma_y\pi D$
P_U = the ultimate load
a = constant exponent
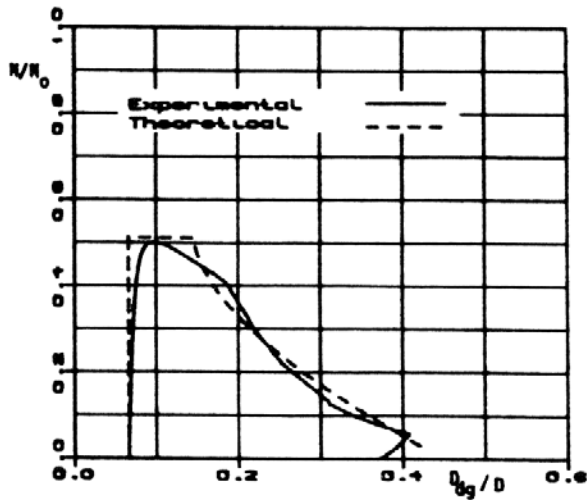
Figure 5.1.3   Axial load/dent growth

Initially undamaged tubes will experience local buckling and subsequent growth of buckle in the post collapse range. This effect which is significant for $D/t > 40$, is handled by the procedure described above.

GEOMETRY AND LOADING:

Figure 5.1.4 shows a pinned column with local dents.

The corresponding geometry and material parameters are given in Table 5.1.1. The compressive axial force is imposed centrically as indicated in Figure 5.1.4.

In the USFOS analyzes the dented tubes are modeled as one single beam element with initial imperfection and local dent. The simple elastic-perfectly-plastic material model is used.

Table 5.1.1   Geometry and material parameters for pinned tube columns with local dents /8/

Spec no	D (mm)	t (mm)	l_k (mm)	σ_y (N/mm^2)	D/t	l_k/r	λ_k	d_o/l	D_d/D
ICIS	109.2	5.1	2000	362	21.2	51.8	0.689	0.0057	0.1185
IAS	118.5	1.5	2000	383	78.2	47.7	0.654	0.0007	0.0480
IIBS	123.2	2.1	2000	224	58.8	45.9	0.481	0.0030	0.1157
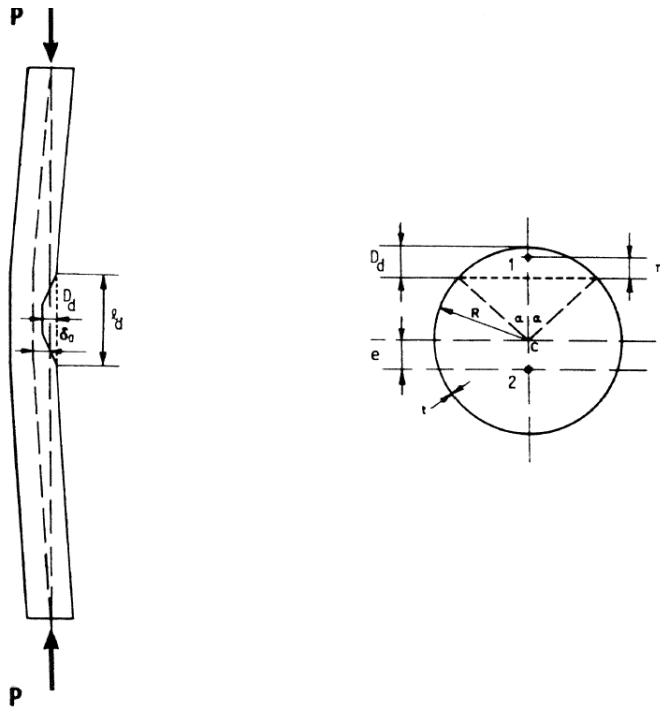
Figure 5.1.4   Dented tube model

RESPONSE:

The response obtained by USFOS is shown in Figure 5.1.5 for the three cases considered, refer Table 5.1.1. The collapse, load normalized with the plastic axial capacity, is plotted versus the axial shortening normalized with the yield shortening.

Experimental results /8/ and numerical simulation performed by the program DENTA /8/ are for comparison shown with dotted lines. USFOS is seen to predict the ultimate load quite well for all cases. This is also the case for the post-collapse behaviour. One of the dotted curves in Figure 5.1.5a) shows the response when the ovalization of the cross section is neglected in the simulation. It is observed that for this case the post-collapse strength is overestimated by over 100 %.
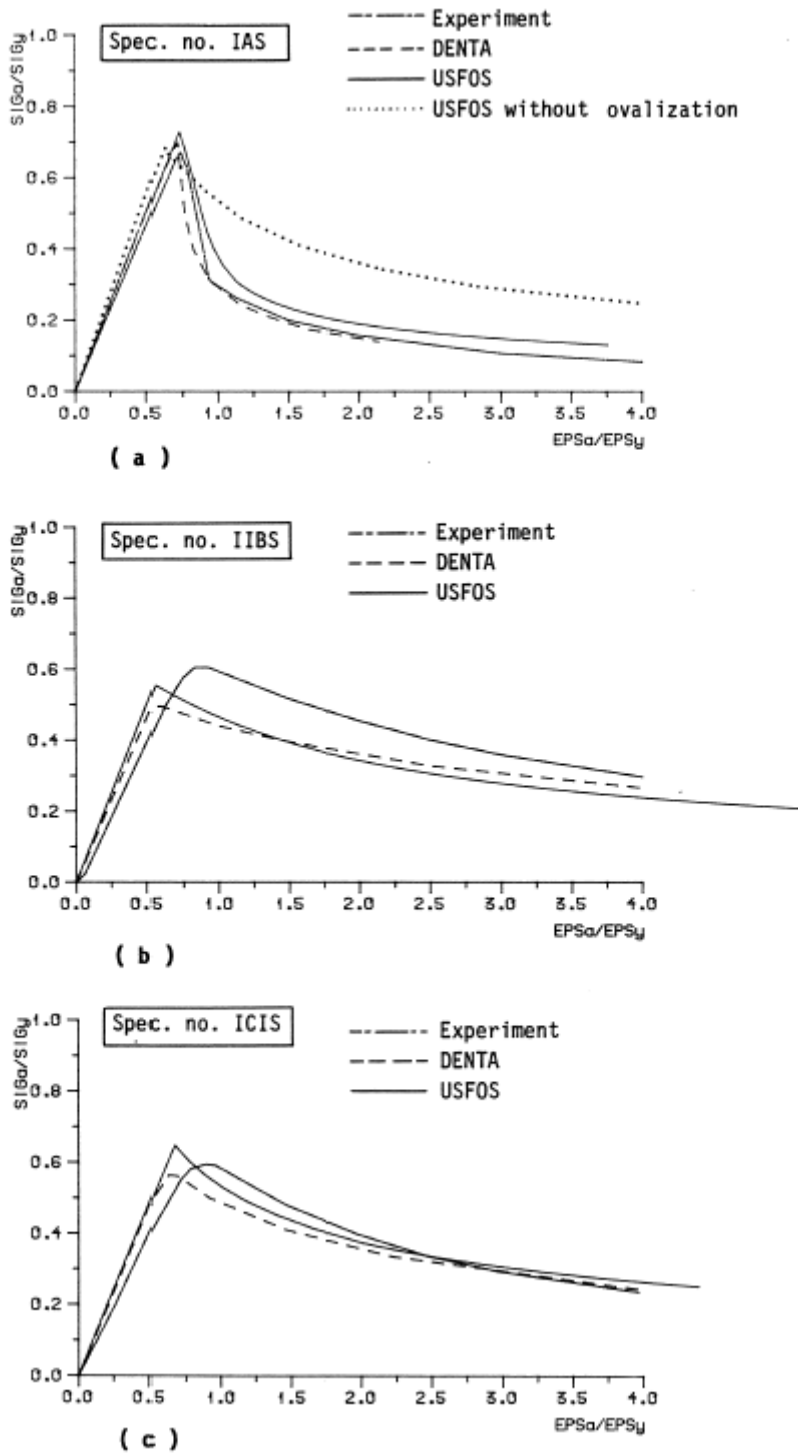
Figure 5.1.5   Axial load versus axial shortening for column

```
HEAD      ELASTO - DENTED TUBE MODEL
          USFOS progressive collapse analysis
          SINTEF Structures and Concrete
'
'
'         inpri    outpri   termpri
CPRINT    1        2        1
'
'         epssol  gamstp  ifunc  pereul  ktrmax  dentsw  cmax  ifysw
CPROPAR   1.0E-20 0.10    2      0.05    5       0       999   1
'
'         nloads  npostp   mxpstp  mxdis
CUSFOS    10      30       0.1     0.05
'         lcomb   lfact    mxld    nstep   minstp
          1       0.25     0.0     40      0.01
'         ncnods
CNODES    1
'         nodex   idof    dfact
          2       1       1.0
'         elnox   impgroup
GELIMP    1       1
'         impgroup impshape angle   offset  dent1  dent2  dentmid
GIMPER    1        0        0       0.005705 0.0    0.0    0.11318
'
'         matno   E-mod    poiss   yield   density   term.expan
MISOIEP   1       0.210E+12  0.3   0.330E+09 0.7850E+04  0.0
'
```

List 5.1.1   Listing of USFOS control input file

6 DYNAMIC ANALYSIS

6.1 EIGENVALUE ANALYSIS

GEOMETRY AND LOADING

A 100 meter long steel pipe is the test case. The pipe is simply supported, and subdiveded into 80 elements. The outer diameter of the pipe is 1.0 meter, wall thickness is 0.05 meter. Gravity load is applied and eigenvalue analysis is performed when the static configuration is reached. The analysis is performed both with the pipe submerged in seawater and free in air. The USFOS control input file is shown in list 6.1.1.

RESPONSE:

The frequencies for the 15 first eigenmodes are compared with results from other program systems and equation 6.x.x . This is shown in figure 6.1.1. The figure shows that the computer programs gives nearly identical results, both in air and water.

The analytical solution differs somewhat from the other results, this is due to the limitations of the formula.

```
HEAD                U S F O S  -  Eigenvalue Analysis
             Verification Example, Simply Supported Beam
                    SINTEF Structures and Concrete
'
'        inprint outprin  termpri
 CPRINT    3       2          1
'        max_step
 CMAXSTEP 10000
'        rest    resu
 CSAVE      0       1
'          lcomb  lstep
 EIGENVAL    1      50
'         alpha  beta      gamma
 CDYNPAR   0.00   0.25      0.50
'         alpha1 alpha2
 RAYLDAMP  0.0    0.2
'        rotmass
 LUMPMASS   0.25
'
'        epssol  gamstp ifunc pereul ktrmax dentsw   cmax   ifysw  detsw
 CPROPAR 1.0E-50 0.10     3    0.05     5      0      999.0    0      0
'
'       ncnods
CNODES   1
'        nodex    idof     dfact
         2        3         1.
'
'        nloads   npostp   mxpstp   mxpdis
CDYNAMIC 80        10        1.00     0.10
'       lcomb    lfact    mxld      nstep     minstp    time incr pr step
'
'        in Air
         1        0.1       1.0       10        0.001     0.100
         1        0.000001 0.0        40        0.001     0.100
'        in Water
'        1        0.01854  0.1854    10        0.001     0.100
'        1        0.000001 0.0        40        0.001     0.100
'
' -- Material definitions --
'   In Air:  rho_steel = 7850 kg/m^3
'
'        matno   E-mod      poiss    yield     density    therm.exp
 MISOIEP  1      0.210E+12  0.0      1.0000E+20 0.7850E+04 1.2E-05
'
'    In Water, Static Analysis: rho_(steel-buoyancy) = 2455.26 kg/m^3
''   In Water, Dynamic Analysis: rho_(steel+added_mass)= 13244.7 kg/m^3
'   static configuration achieved by applying a factor 0.1854 to the
'   total dynamic mass. From this config. the eigenvalue analysis is
'   done.
'
'        matno   E-mod      poiss    yield     density    therm.exp
'MISOIEP  1      0.2100E+12 0.0      1.0000E+20 13244.7    1.2E-05
```

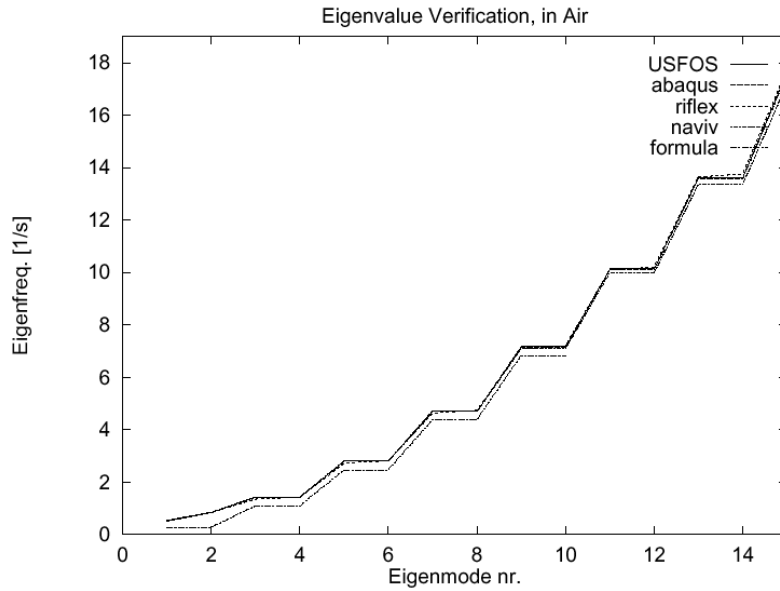List 6.1.1   USFOS control input file

Figure 6.1.1a   USFOS results from eigenvalue analysis compared with results from other program systems and analytic solution
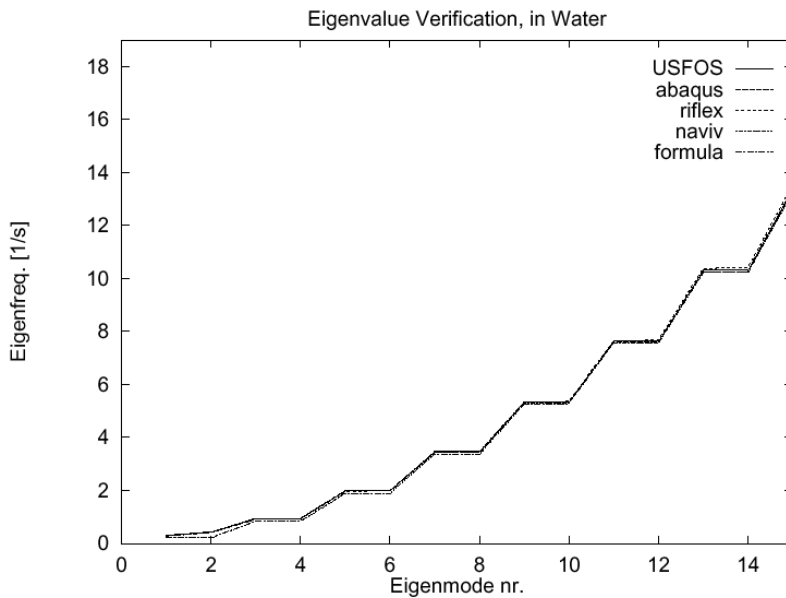

Figure 6.1.1b   USFOS results from eigenvalue analysis compared with results from other program systems and analytic solution

7   CYCLIC ANALYSIS

The plasticity model implemented in USFOS is generally considered to give good results for the case of monotonic loading. However, the model fails to account for cyclic transient material behaviour.

Generally the transient plastic material behaviour is considered to be a function of the accumulated plastic work or accumulated plastic strain.

Experimental cyclic data for cross sections show different characteristics for monotonic and cyclic loading. Thus, the parameters defining the plastification process and material hardening have to be different for cyclic loading as compared to the monotonic loading. Material data for both monotonic and repeated plastic loading are available from standard material tests. Some experimental data are also available for cross sections. This data may be used to calibrate a cyclic material model.

A simplified approach has been implemented in USFOS to account for the cyclic behaviour of steel materials. Two distinct material characteristics are defined:

i)   A monotonic model which reflects the initial loading material behaviour, defined by the relevant plasticity model parameters: Z_{ym}, Z_{bm}, and a_{im} , c_{im}, i = 1,6.

ii)   A stabilized cyclic model reflecting the stabilized cyclic material behaviour, defined by the cyclic plasticity model parameters: Z_{yc}, Z_{bc}, and a_{ic} , c_{ic} , i = 1,6.

where Z_y and Z_b is the extension of the yield and bounding surface, respectively.

The continuous transition from monotonic to stabilized cyclic behaviour is in this simplified approach disregarded, and a instantaneous switch from monotonic to stabilized cyclic behaviour is implemented. Stabilized cyclic parameters are introduced when the plastic work dissipated in a plastic hinge ‚exceeds a certain threshold value.

The accuracy of the plastic hinge model depends largely on a proper selection of the plasticity parameters. The default parameters are calibrated from tests with St52 steel.

7.1 CYCLIC BEAM COLUMN BEHAVIOUR

The accuracy of the cyclic plasticity model implemented in USFOS has been assessed by comparison with cyclic test results obtained by Granli /xx/. In the Granli test series 8 different tubular columns of length 2290 mm with a D/t ratio ranging from 10 to 36 and a yield stress of 380 MPa have been examined. The specimens were subjected to displacement controlled cyclic loading with variable amplitudes. Test 20B from this test series is used here for comparison with USFOS simulation.

GEOMETRY AND LOADING:

Diameter   127.8   mm
Thickness   6.45   mm
Length   2290   mm

The axial load is applied eccentrically , e = 3mm.

The USFOS simulation is done using the default monotonic and cyclic material parameters. Local buckling is not included in this analysis.

List 7.1.1 shows the USFOS input file.

RESPONSE:

Results from the test and the USFOS simulation are shown in figure 7.1.1 - 7.1.4.

It is observed that USFOS predicts the overall axial force - end shortening behaviour with good accuracy. The compressive peak load in the first test cycle is seen to be significantly larger than that predicted by the simulation. This may be caused by some end restraint occurring due to friction in the joints which is primarily of importance in the first cycle. For the subsequent compression peaks the agreement is excellent. The predicted tensile peak load agrees closely with the test results up to cycle no 5. From this point a certain discrepancy occurs. This corresponds with the time local buckling occurred in the test.
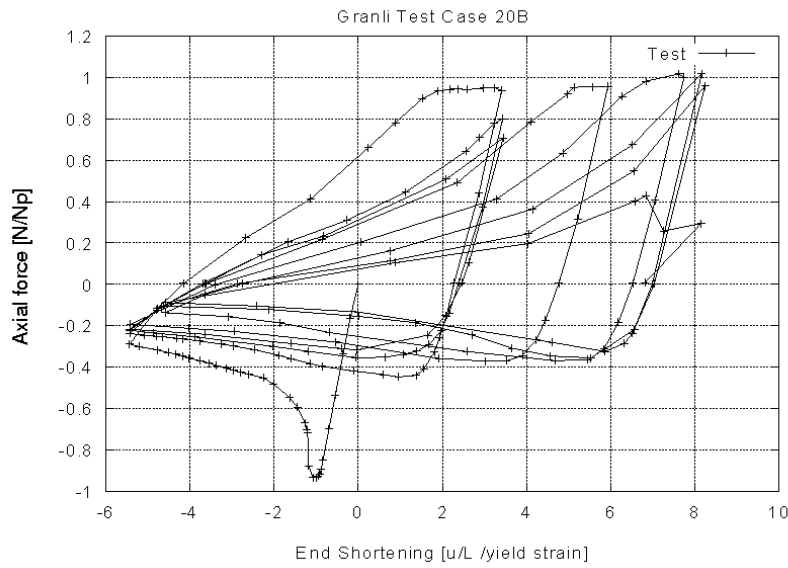
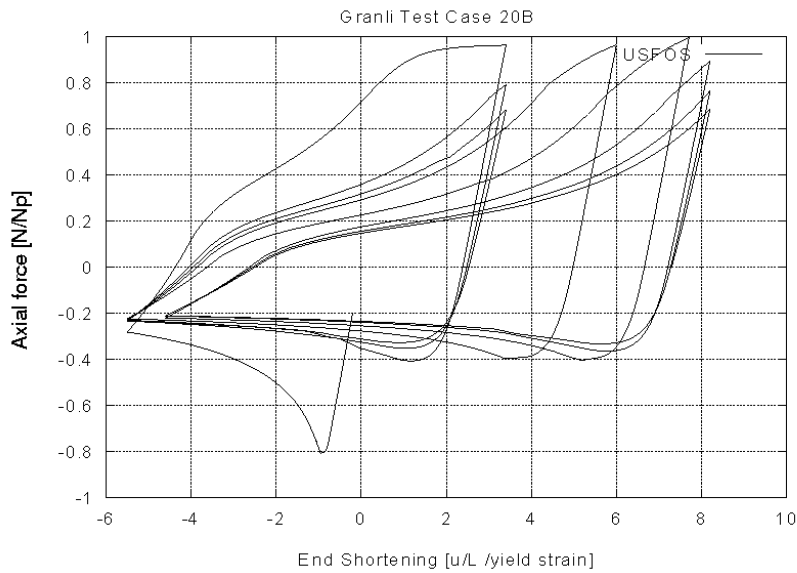*Figure 7.1.1   Axial force - end shortening, Test results*

Figure 7.1.2   Axial force - end shortening, USFOS simulation
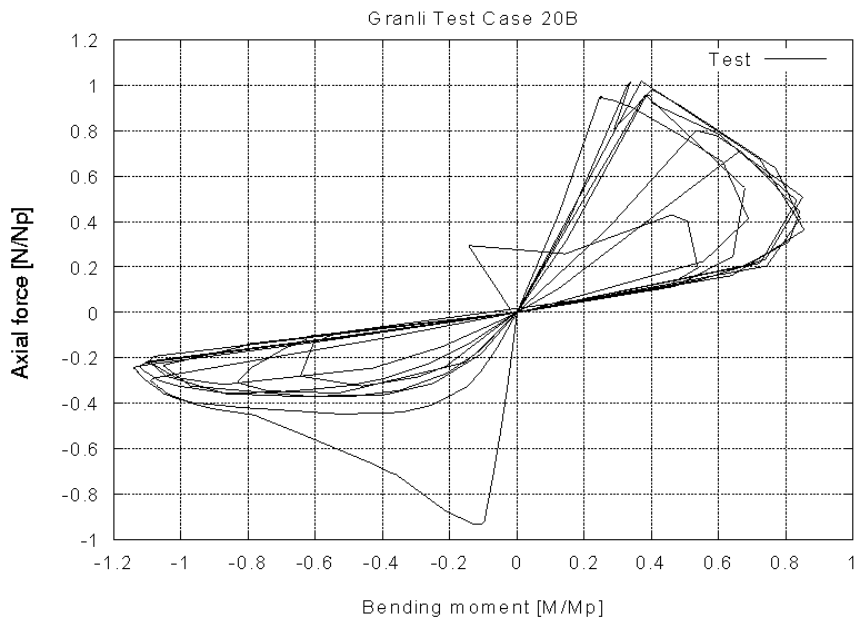
Figure 7.1.3   Bending moment vs axial force, Test results

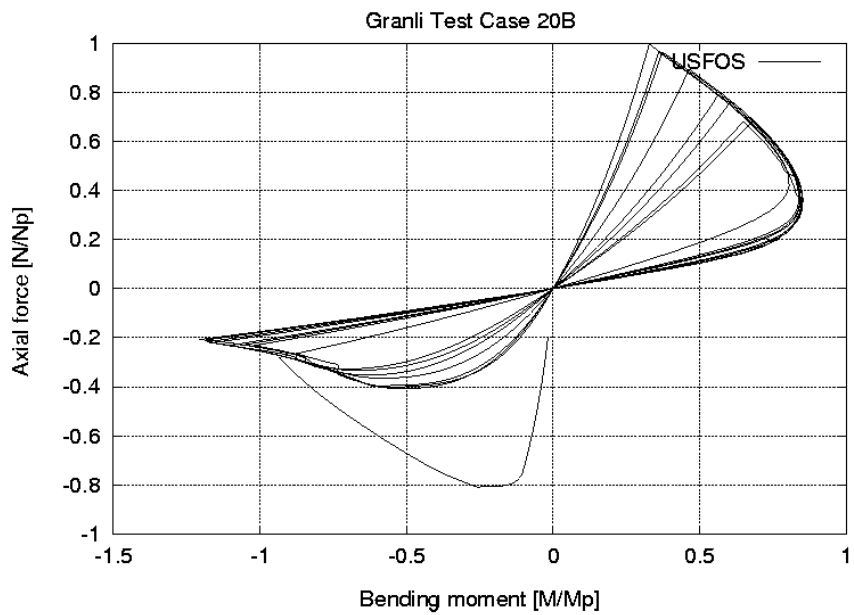

Figure 7.1.4   Bending moment vs axial force, USFOS simulation

```
HEAD             CYCLIC  COLUMN  SIMULATION, TEST CASE 20B
                 One finite element used.  Iterative solution
                 Default material parameters
'
'        inpri    outpri   termpri
CPRINT     1         1        1
'        restart-data  results
CSAVE       0            1
CMAXSTEP 2000
'
'        epssol   gamstp   ifunc    pereul  ktrmax   dentsw    cmax    ifysw
CPROPAR  1.0E-20   0.10      2       0.05      5         0       999       0
'
'        cmin     cneg     itmax     isol    epsit    cmineg
CITER
'
'        nloads   npostp   mxpstp    mxpdis
CICYFOS   10        100     1.00      4.975
'        lcomb    lfact     mxld     mxdisp    nstep    minstp
'          1       0.2      0.0       0.0        0       0.01
' cycle 1
           2      -0.1      -0.7      0.0        0       0.001
           2      -0.025    -0.75     0.0        0       0.001
           2      -0.01     0.0       0.0       15       0.001
           2      -0.05     0.0      -5.5        0       0.001
           2       0.1      0.2       3.4        0       0.001
           2       0.05     0.8       3.4        0       0.001
           2       0.01     0.0       3.4        0       0.001
' cycle 2
           2      -0.1      -0.1     -5.5        0       0.001
           2      -0.025    -0.25    -5.5        0       0.001
           2      -0.01     0.0      -5.5       20       0.001
           2      -0.05     0.0      -5.5        0       0.001
           2       0.1      0.05      3.4        0       0.001
           2       0.05     0.0       3.4        0       0.001
' cycle 3
           2      -0.1      -0.1     -5.5        0       0.001
           2      -0.025    -0.25    -5.5        0       0.001
           2      -0.01     0.0      -5.5       15       0.001
           2      -0.05     0.0      -5.5        0       0.001
           2       0.1      0.05      3.4        0       0.001
           2       0.05     0.0       3.4        0       0.001
' cycle 4
           2      -0.1      -0.1     -5.5        0       0.001
           2      -0.025    -0.25    -5.5        0       0.001
           2      -0.01     0.0      -5.5       15       0.001
```

List 7.1.1 USFOS input file (continues on next page)

```
' cycle 4
        2     -0.1    -0.1    -5.5      0       0.001
        2     -0.025  -0.25   -5.5      0       0.001
        2     -0.01    0.0    -5.5     15       0.001
        2     -0.05    0.0    -5.5      0       0.001
        2      0.1     0.05    6.0      0       0.001
        2      0.05    0.8     6.0      0       0.001
        2      0.01    0.0     6.0      0       0.001
' cycle 5
        2     -0.1    -0.1    -5.5      0       0.001
        2     -0.025  -0.25   -5.5      0       0.001
        2     -0.01    0.0    -5.5     15       0.001
        2     -0.05    0.0    -5.5      0       0.001
        2      0.1     0.05    7.7      0       0.001
        2      0.05    0.0     7.7      0       0.001
' cycle 6
        2     -0.1    -0.1    -4.6      0       0.001
        2     -0.025  -0.25   -5.5      0       0.001
        2     -0.01    0.0    -5.5     15       0.001
        2     -0.05    0.0    -4.6      0       0.001
        2      0.1     0.05    8.2      0       0.001
        2      0.05    0.0     8.2      0       0.001
' cycle 7
        2     -0.1    -0.10   -4.6      0       0.001
        2     -0.025  -0.25   -5.5      0       0.001
        2     -0.01    0.0    -5.5     15       0.001
        2     -0.05    0.0    -4.6      0       0.001
        2      0.1     0.2     8.2      0       0.001
        2      0.05    0.0     8.2      0       0.001
' cycle 8
        2     -0.1    -0.10   -4.6      0       0.001
        2     -0.025  -0.25   -5.5      0       0.001
        2     -0.01    0.0    -5.5     15       0.001
        2     -0.05    0.0    -4.6      0       0.001
        2      0.1     0.2     8.2      0       0.001
        2      0.05    0.0     8.2      0       0.001
'
        2     -0.1    -0.0001  0.0      0       0.001
'
'        ncnods
CNODES   1
'        nodex   idof    dfact
         2       1       241.26
'
'        matno   E-mod   poiss   yield   density   therm.exp.
MISOIEP  1    2.10E+11   0.3    380E+06  7.850E+03    0.0
'
'        matno    C1      A1    ( C2 A2   ..  C6 A6 )
'MPLASCYC
```

List 7.1.1 USFOS input file (continued from previous page)

```
' --------------------------------------------------------------------
' --------    Geometry and load input - U F O format    -----------------
' --------------------------------------------------------------------
'
'          Node ID      X               Y               Z    Boundary code
 NODE          1     -2.290          .000            .000   1 1 1 1 0 1
 NODE          2      .000           .000            .000   0 1 1 1 0 1
'
'          Elem ID   np1 np2   material    geom     lcoor    ecc1     ecc2
 BEAM          1     1   2      1           1         1        1        1
'
'          Geom ID       Do          Thick    Shear_y   Shear_z
 PIPE          1     .12780000   .00645000 1.00      1.00
'
'          Loc-Coo        dx             dy              dz
 UNITVEC       1          .000           .000            1.000
'
'          Ecc-ID         Ex             Ey              Ez
 ECCENT        1          .000           .000           -.003
'
'
'          Load Case  Node ID      Fx           Fy      Fz
 NODELOAD      1          2     -9.34400E+05     0.0     0.0
 NODELOAD      2          2      9.34400E+05     0.0     0.0
'
```

List 7.1.2 Structural Model

8   SHIP IMPACT ANALYSIS

8.1   SHIP IMPACT CALCULATION

This section demonstrates the performance of the ship impact algorithm. The formulation utilizes the dented tube model for calculation of ultimate capacity of dented tubulars. The local deformation of the tube wall is implemented according to curves recommended by DnV. The functions have been modified to account for the axial force in the member, not only the lateral impact load.

The impact load determined by USFOS is incremented until the total impact energy has been dissipated. The structure is then unloaded, with residual forces and permanent displacements saved for further residual strength analyses.

GEOMETRY AND LOADING:

Figure 8.1.1 shows a 10 meter long beam, clamped at both ends. Geometrical data and material properties are listed in the figure. The beam is modelled with two finite elements, with impact loading specified in the middle node.
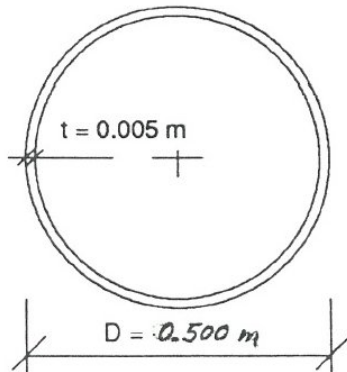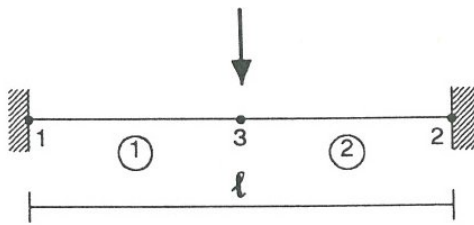
$$\sigma_y = 330 \ \text{MPa}$$
$$E = 2.1 \cdot 10^5 \ \text{N/mm}^2$$
$$N_p = 2565.0 \ \text{kN}$$
$$M_p = 404.31 \ \text{kNm}$$
$$L = 10.000 \ \text{m}$$

Mechanism
load $F_M = 323.4 \ \text{kN}$

Figure 8-1 Impact test beam

RESPONSE:
Based on the beam geometry and cross section parameters, USFOS calculates an initial impact force of 20 kN (6% of the mechanism load). With impact loading specified, first yield occurs at member midspan at 175 kN. The local deformation is then 17.4 % of the beam diameter. A three hinge mechanism is formed at 244 kN. When the specified energy is dissipated, the beam is unloaded. Permanent dent depth was 71 % of the tube diameter. The load deformation curves are shown in Figure 8.1.2.
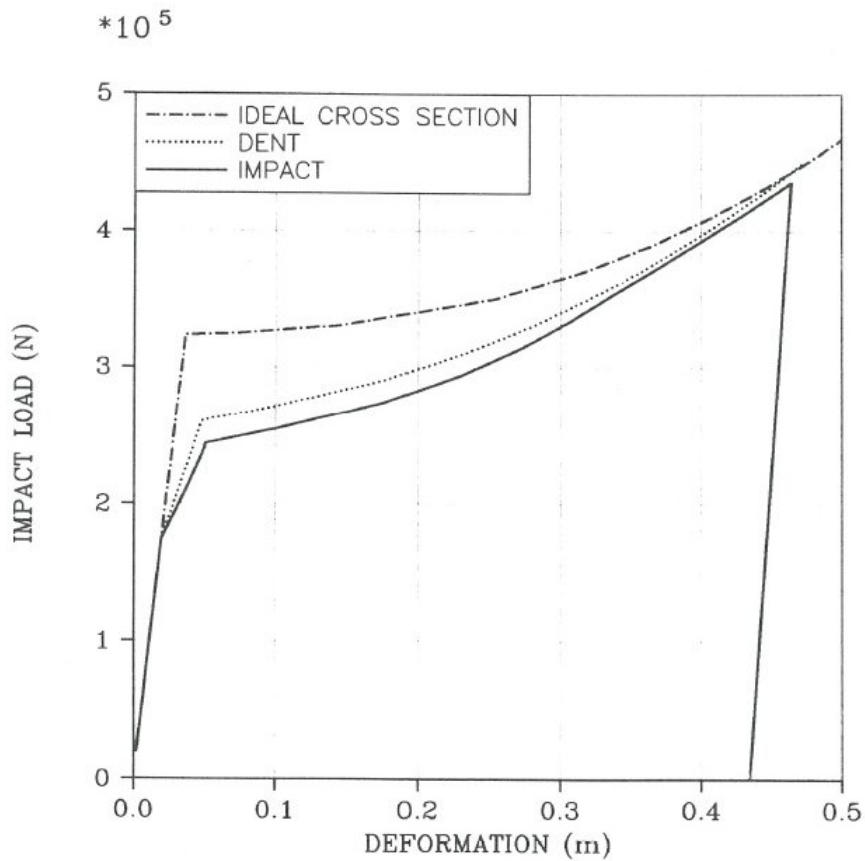
Figure 8-2 Beam Load-Deformation

The dent depth at first yield, predicted by the impact algorithm was then assigned as an initial dent (DENTED TUBE MODEL). First yield is detected at the same load level as the impact algorithm, but the dent growth is not included.

Finally, unloaded beam is reloaded, with restart specified from the last step of the internal unloading load case. Load-deformation curves and moment-axial force interaction is shown in Figure 8.1.3. This indicates that residual forces and permanent deformations are saved for subsequent restart analyses.
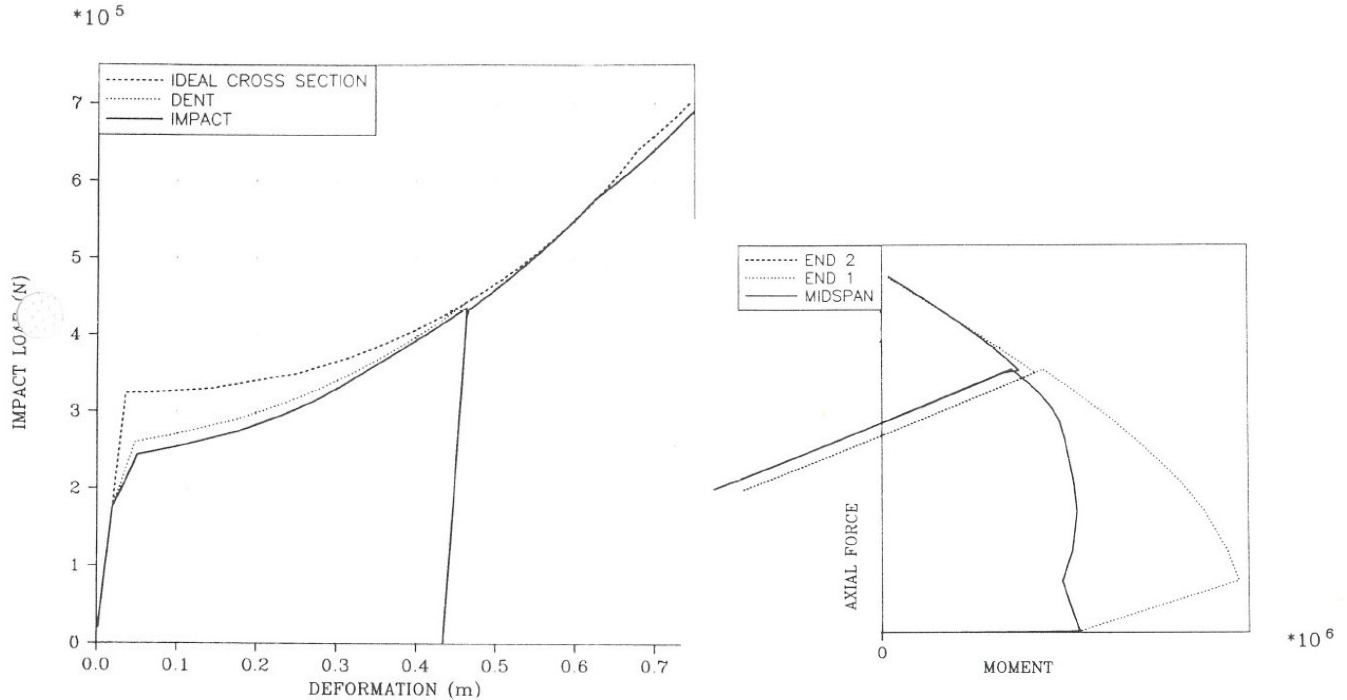
**Figure 8-3   a)   Load – Deformation   b)   Moment – Axial Force
                    impact beam   interaction**

The moment-axial force interaction shows how the moment capacity at beam midspan is reduced due to the local denting of the tube. After first yielding, the dent increases, resulting in a continued reduction in bending moment at beam midspan.

When hinges form at the beam ends, significant membrane forces develop, and the state of forces at midsection follows the yield surface for a dented tube. Residual moments and forces after unloading of the beam is shown in the figure. When the beam is reloaded, yielding takes place at the same position where unloading was performed (disregarding drift-off from the yield surface).

As the membrane force increase, the effect of the midspan dent becomes less and less important. That is, the dent does not influence the membrane capacity of the member.

Finally, a number of analyses were done with one end of the beam free to move axially, and with a constant axial load in the member. Load - deformation curves for the local denting is shown in Figure 8.1.4, for different axial forces.

$*10^5$
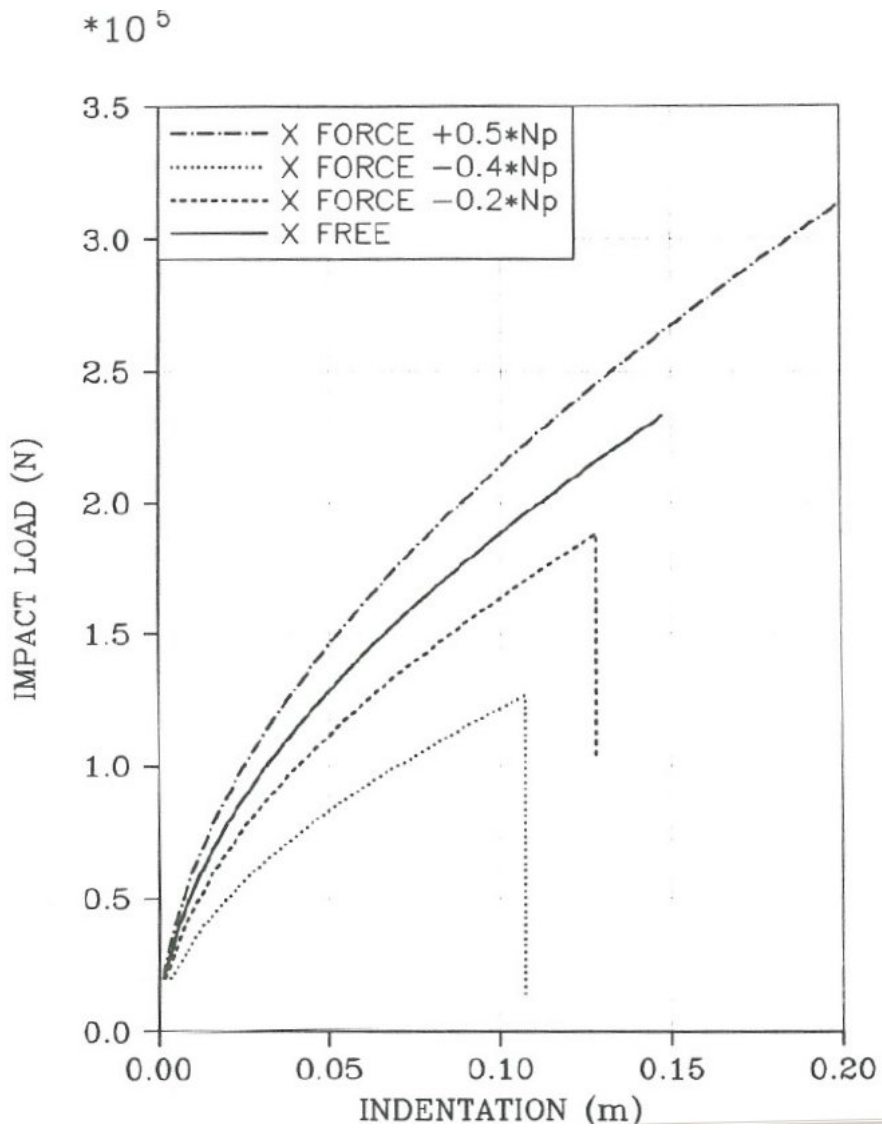
Figure 8-4 Load - Indentation versus axial load

```
HEAD      SHIP  IMPACT  TEST  CASE
          USFOS progressive collapse analysis
          SINTEF Structures and Concrete
'
'
'         inpri    outpri  termpri
CPRINT    3        2  1
'
'         epssol  gamstp  ifunc  pereul  ktrmax  dentsw  cmax  ifysw
CPROPAR 1.0E-20   0.02    2      0.05    5       1       999   1
'
'         nloads  npostp  mxpstp   mxpdis
CUSFOS    10      10      1.00    1.00
'         lcomb   lfact   mxld  nstep    minstp
          4       1.0     0.0   50       0.001
'
'         ncnods
CNODES    1
'         nodex   idof  dfact
          3       2     1.
'
'         ldcs  elnox  elpos  energy   extent  xdir  ydir  zdir  ship
BIMPACT   4     1      2      2.50E+05  0.0     0     -1    0     345
'
'         ship  P1       P2        P3        D1
 MSHIP    345   1.0E+05  1.75E+05  2.5E+05  1.0
 MSHIP    5
'
'      impgroup  impshape  angle  offset  dent1     dent2      dentmid
'GIMPER   1         0       90.0   0.0     0.0   0.1741094      0.0
'
'         elnox  impgroup
'GELIMP   1      1
'
'         matno   E-mod   poiss   yield    density   term. expan
MISOIEP   1     2.10E+11  0.3   .330E+09  .785E+04   0.0
'
```

List 8.1.1   Listing of USFOS control input file

9   FIRE RESPONSE ANALYSIS

Mechanical response due to high temperature exposure may be calculated with USFOS. Temperature loads are given as element-mean-temperature and temperature gradients in local y- and z-direction of the beam section, see figure below.
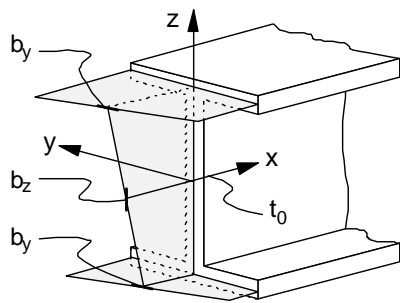
Temperature and gradients are assumed constant in element length direction. The temperature-load input may be given manually or generated by FAHTS /xx/.

By default the Yield-strength and E-module parameters are temperature dependent according to ECCS /xx/ steel curves. The temperature-expansion coefficient is assumed constant. Other temperature - material parameter relationships may be defined, either by using predefined curve-sets for different types of material, or by defining your own temperature dependency curves.

9.1   BEAM COLUMN TEST, UNIFORM HEATING

GEOMETRY AND LOADING:

A simply supported beam column is loaded axially. The load is kept constant while the beam is uniformly heated.

Beam data: *Cross Section:*   *IPE 160*
                Length   *3110.0*   *[mm]*
                Yield: *448.0*   *[MPa]*

The initial lateral deflection at mid-span is 4.21 m at zero load. The axial load is kept constant at 91.2 kN during the test.

Loading arrangement are shown in Figure 10.1.1. The USFOS control input file is shown in list 10.1.1. The default temperature dependency curves from ECCS are used.
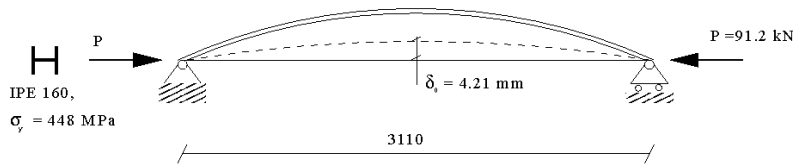
Figure 9-1 Loading arrangement, beam column test

The column is given an initial imperfection of 4.2mm at mid-span, and is buckling about the *"weak"* axis.

RESPONSE:

In Figure 10.1.2, the USFOS results are compared with experimental results /16/. The USFOS analysis shows good agreement with the experimental findings. In the simulation results, the start point of the lateral deflection is adjusted to the measured start point of the heating in order to compare the temperature response.
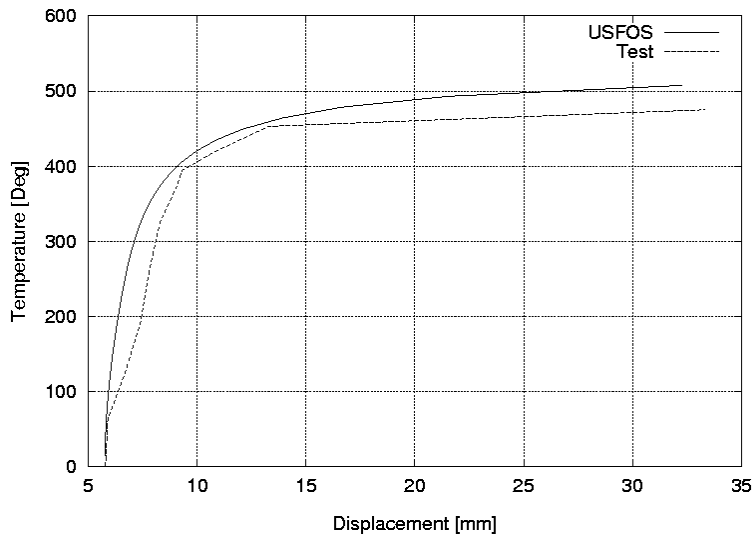
Figure 9-2   Lateral displacement vs temperature.

```
HEAD                            BEAM   FIRE


'     rest resu
CSAVE   0    1
'
'         inpri    outpri   termpri
CPRINT    5        5        1
'         epssol   gamstp   ifunc    pereul   ktrmax   dentsw   cmax    ifysw
CPROPAR   1.0E-20  0.10     2        0.95     5        0        999.0   0
'
CITER
ARC_OFF
DETEROFF
'
'         nloads   npostp   mxpstp   mxpdis
CUSFOS    10       5        1.00     1.0
'         lcomb    lfact    mxld     nstep      minstp
          1        3.0      10.0     30         0.001
          2        1.0      35.0     200        0.001
'         ncnods
CNODES    1
'         nodex    idof     dfact
          5        2        -1.
'       impgroup  impshape  angle    offset   dent1    dent2    dentmid
GIMPER    1        0        0        0.043    0.0      0.0      0.0
'         elnox   impgroup
GELIMP    3        1
'         matno    E-mod    poiss    yield    density    therm. exp.
MISOIEP   1.       0.210E+06  0.3    0.448E+03  0.7850E+04   1.4E-05
'
'         ldcase   elnox    Tempx    gradTy   gradTz
BELTEMP   2        1        3.4      0        0
BELTEMP   2        2        8.7      0        0
BELTEMP   2        3        14.2     0        0
BELTEMP   2        4        14.5     0        0
BELTEMP   2        5        14.5     0        0
BELTEMP   2        6        14.2     0        0
BELTEMP   2        7        8.7      0        0
BELTEMP   2        8        3.4      0        0
```

List 10.1.1   USFOS control input file.

9.2   TWO-PORTAL FRAME

GEOMETRY AND LOADING:

A two-portal frame is loaded with vertical and horizontal nodal loads. These loads are kept constant. Then some of the members are subjected to uniform temperature loading. Frame and loading arrangement are shown in Figure 9-3.

The USFOS control input file is shown in List 9.2.1. Note that the STEELTDEP card is used, with default settings, this means that the material properties are temperature dependent according to Eurocode 3 /xx/.
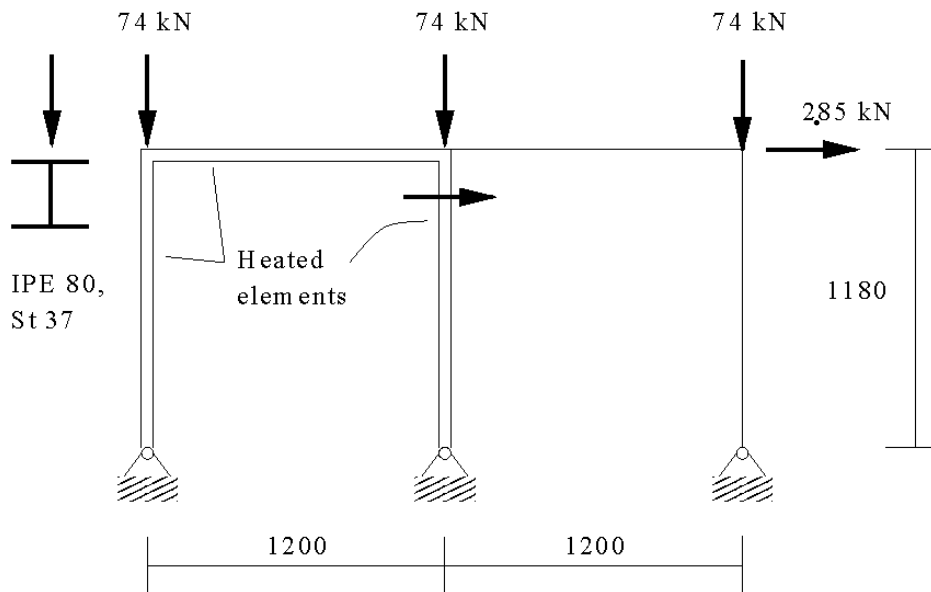
RESPONSE:

Horizontal displacement of the mid node and horizontal reaction forces from the USFOS analysis
are compared with experimental results /xx/. Figure 9-4 and Figure 9-5 show good agreement
between the test and the USFOS analysis.
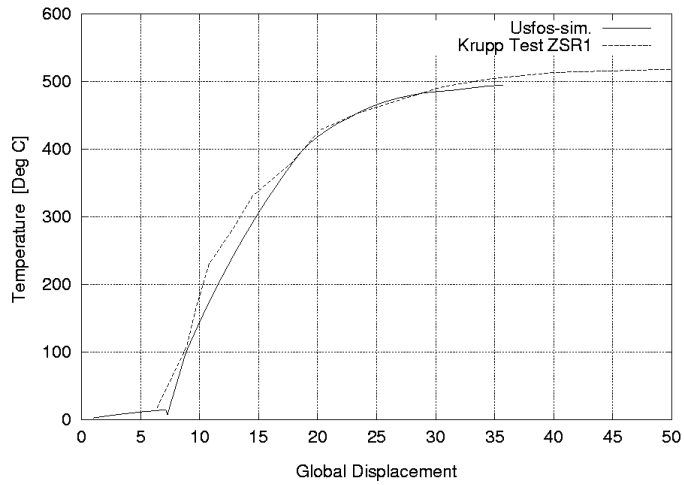
Figure 9-4 Horisontal displacement -Mid node

Figure 9-5 Horizontal reaction forces.

```
HEAD                 UFOS Verification Example
              Temperature analysis of Two-portal-frame
                   Comparison with test results
'
'
'      rest_data   resu_data
CSAVE     0            1
'
'         inpri     outpri   termpri
CPRINT     2          2         1
XFOSFULL
'
'         epssol   gamstp   ifunc    pereul   ktrmax   dentsw   cmax    ifysw
CPROPAR   1.0E-20   0.10      2       0.95      5        0      999.0     0
'
CITER
ARC_OFF
DETEROFF
'
'         nloads   npostp   mxpstp    mxpdis
CICYFOS    10        5        1.00      1.0
'         lcomb    lfact    mxld    mxdis     nstep     minstp
           1        0.2      1.0     0.0       50       0.001
           2        0.5     35.00   35.0      500       0.001
'
'         ncnods
CNODES     1
'         nodex    idof     dfact
           4        1        1.
'
'         matno    E-mod    poiss    yield    density    therm. exp.
MISOIEP    1.    0.210E+06   0.3   0.355E+03  0.7850E+04   1.4E-05
'         matno   Zy_m  Zb_m   Zy_c   Zb_c
GBOUND     1     0.50   1.0    0.50   1.0
'
'        Temperature dependency according to Eurocode 3:
'
'         curve_set   matno_1 .. matno_n
STEELTDEP     1           1
'
'
'         ldcase    elnox    Tempx    gradTy   gradTz
BELTEMP     2         1       15.0       0        0
BELTEMP     2         2       15.0       0        0
BELTEMP     2         3       15.0       0        0
```

List 9.2.1   USFOS control input file.

10 NUMERICAL PROCEDURE VERIFICATION

The present chapter verifies of the solution procedures utilized by USFOS.

10.1 SNAP-THROUGH PROBLEM

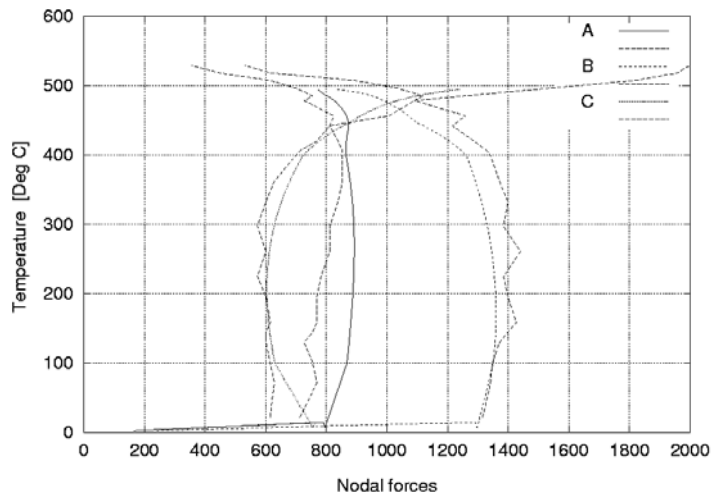The snap through problem represents a simple verification example involving large rotations and instability behaviour. The performance of the current stiffness parameter is demonstrated.

GEOMETRY AND LOADING:

The geometry and loading of a simply supported beam element is shown in Figure 10-1. The beam, pinned at one end and free to slide in one direction at the other, is initially compressed. It is assumed that the beam behaves linearly elastic, and that the strains are small (this will be the case as long as $0 < v < 2H$). The problem thus only involves nonlinear geometry effects.

As Euler-Cauchy incrementation is used, a small loadstep was used to avoid drift from the true solution.
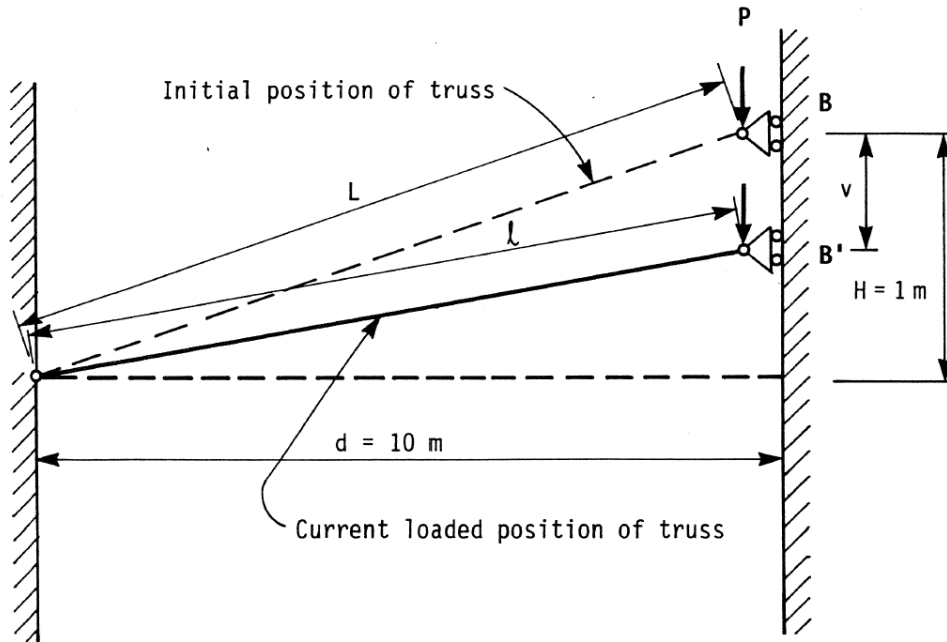
RESPONSE

In the first phase of the loading, the system behaves approximately linearly. As the vertical displacement increases, geometrical stiffness becomes dominating. At the point where the displacement has reached 42% of H, the system becomes unstable and snap-through occurs. The system then unloads with negative stiffness. As the displacement v reaches 158% of H the system again becomes stable resuming the onloading process.

As the structure is modelled as a single-degree-of-freedom system, the response may easily be evaluated on analytical form from equilibrium conditions:

$$P = \frac{EAL}{(L^2 - v^2)}(v - H) \bullet \ln\left(\frac{(L^2 - v^2)^{1/2}}{L}\right) \qquad (10.1.1)$$

The response computed by USFOS shown in Figure 10-2, gives exactly the same solution as Eq 11.1.1. Increasing the load step size will however introduce drift effects.

Figure 10-3 shows the variation of the current stiffness parameter as a function of a normalized vertical displacement at point B. It is observed that at the maximum and minimum point of the load-displacement curve Sp equates zero.

Element Data:
Youngs Modulus   E = 2.1×10^5 [MPa]
Cross Section Area   A =   0.2407   [m^2]
Initial element length L =   10.0   [m]
Initial offset   H =   1.0   [m]

Figure 10-1 Elastic large rotation snap-through problem
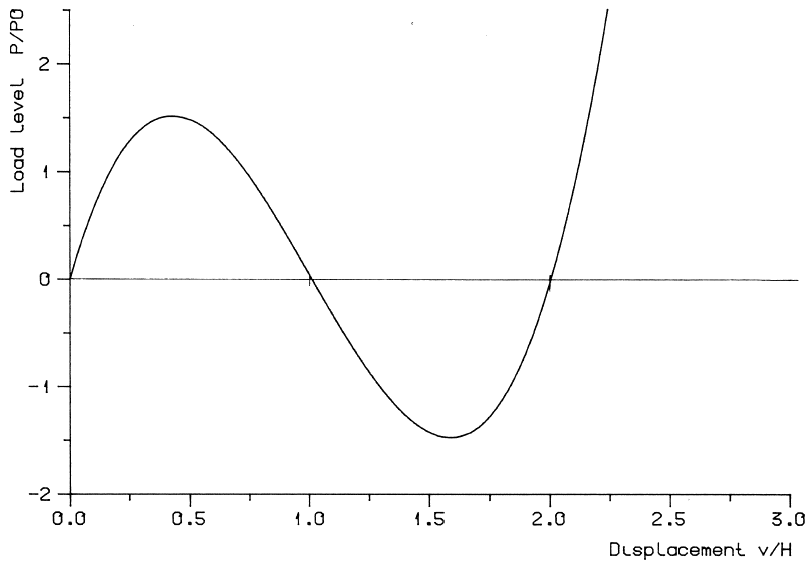
Figure 10-2 Load-displacement response for snap-through problem
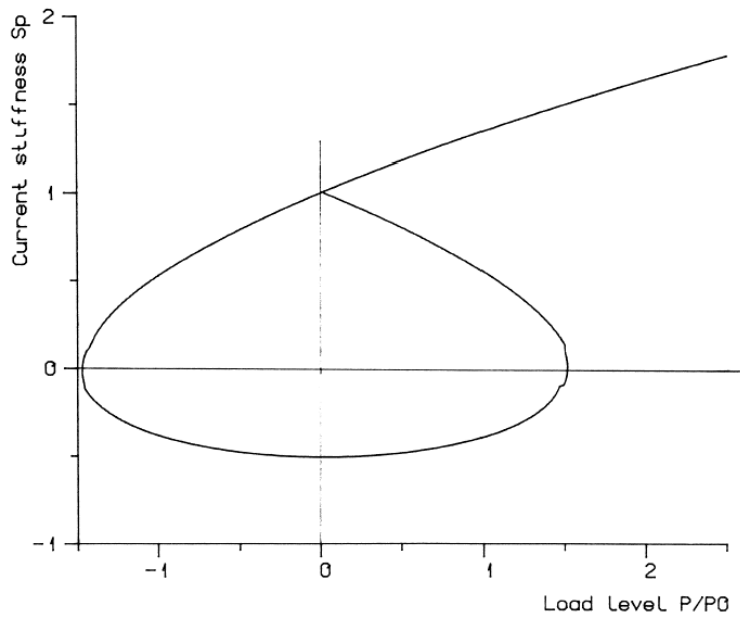

Figure 10-3 Current stiffness parameter for snap-through problem

```
 HEAD        ELASTIC SNAP-THROUGH PROBLEM
        U S F O S  progressive collapse analysis
      S I N T E F  Structures and Concrete
'
'
'        inpri    outpri   termpri
 CPRINT     1        2        1
'
'        epssol   gamstp   ifunc     pereul   ktrmax   dentsw    cmax    ifysw
 CPROPAR  1.0E-20   0.10      2       0.05       5        0        999      0
'
'        nloads   npostp   mxpstp    mxpdis
 CUSFOS    10       100      1.00      0.20
'        lcomb    lfact    mxld     nstep      minstp
          2        0.01      0        200       0.001
'
'        ncnods
 CNODES    1
'        nodex    idof     dfact
          2        1         1.
'
'        matno    E-mod    poiss    yield     density     TermX
 MISOIEP   1      0.210E+12  0.3   0.330E+12  0.7850E+04  0.0
'        matno    C1    A1     C2    A2        ..    C6     A6
 MPLASMON   1     0.015  0.25
'
'        nodeno   ndof     dx dy dz   rx ry rz
 BNBCD    1        6        1  1  1    1  0  0
 BNBCD    2        6        1  1  0    1  0  0
'        geono      z-yield
 GBOUND     1        0.79
```

List 10.1.1   USFOS control input file for snap-through problem

10.2 LINEAR DEPENDENCY TEST CASE

The purpose of this test case is to verify the linear dependency option 'BLINDP2' in USFOS.

GEOMETRY AND LOADING

Figure 10-4 shows geometry and loading of the cantilevers which are considered.
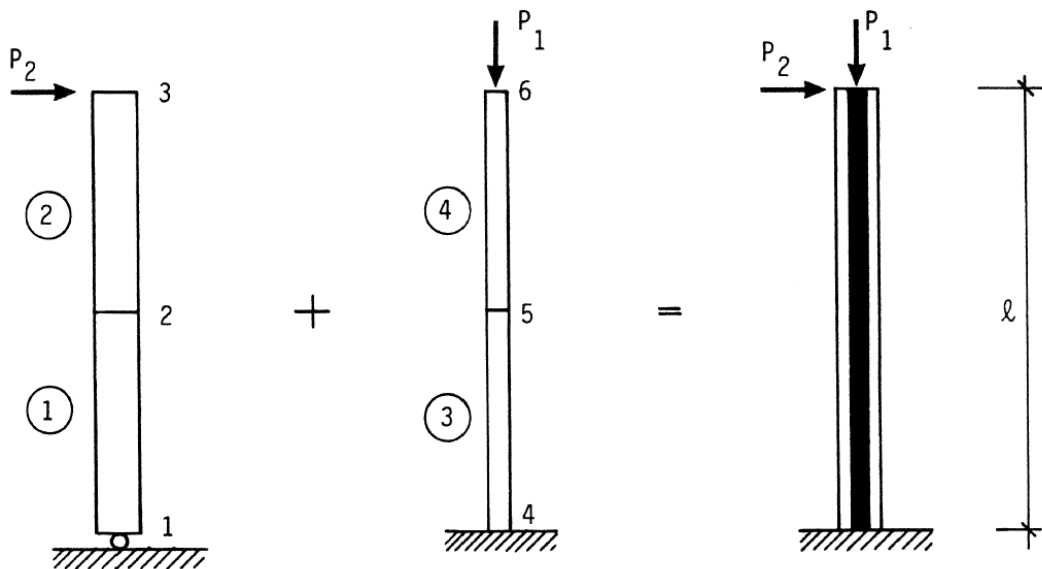

Figure 10-4 Geometry of cantilever with internal and external tube

The cantilever consists of an external and an internal tube, each of which is modelled with two elements. The external tube elements 1 and 2 are connected to nodes 1, 2 and 3 and the tube is free to rotate at node 1.

The internal tube elements 3 and 4 are connected to nodes 4, 5 and 6 and the tube is fixed at node 4. Nodes 1, 4 and 2, 5 and 3, 6 have identical coordinates initially. The load history comprises two cases.

First a vertical load P_1 is applied to the inner tube, and next a horizontal load P_2 is applied to the external tube.

In the first example, node 2 is constrained to follow the local axis of element 3 laterally, and is free to move axially. Node 3 follows local axis of element 4 laterally and is free axially. All rotations are coupled. The linear dependency is according to the previous assumptions modelled as follows:

			Coupled dofs					
'								
'	slave node	master elementi	ix	iy	iz	rix	riy	riz
BLINDP2	2	3	0	1	1	1	1	1
BLINDP2	3	4	0	1	1	1	1	1

A reference example is analysed, where node 2 and node 3 are removed. Element 1 and 2 are connected directly to node 5 and 6 with identical dofs as element 3 and 4.

Geometry and material parameters:

Column length		l	= 12.5	[m]
Young's modulus		E	$= 2.1 \ 10^{11}$	[N/m^2]
Initial load	Vertical	P_1	= 1 106	[N]
	Horizontal	P_2	$= 1 \ 10^5$	[N]
External tube	Outer diameter	D_e	= 0.40	[m]
	Tube thickness	t_e	= 0.07	[m]
	Yield stress	f_y	$= 248 \ 10^6$	[N/m^2]
Internal tube	Outer diameter	D_i	= 0.25	[m]
	Tube thickness	t_i	= 0.05	[m]
	Yield stress	f_y	$= 10^{10}$	[N/m^2]

(The yield stress of the internal tube is set to a high value.)

The test shows how the external (slave) tube follows the internal (master) tube. The displacements are illustrated in Figure 10.2.4. It should be noted that the relative displacements between the internal and external nodes are exaggerated to illustrate that the slave node follows the system line of the master element.

The rotation in the slave nodes are constrained to follow the rotations in the corresponding master nodes adjusted for the position of the slave node along the system axis of the master element.
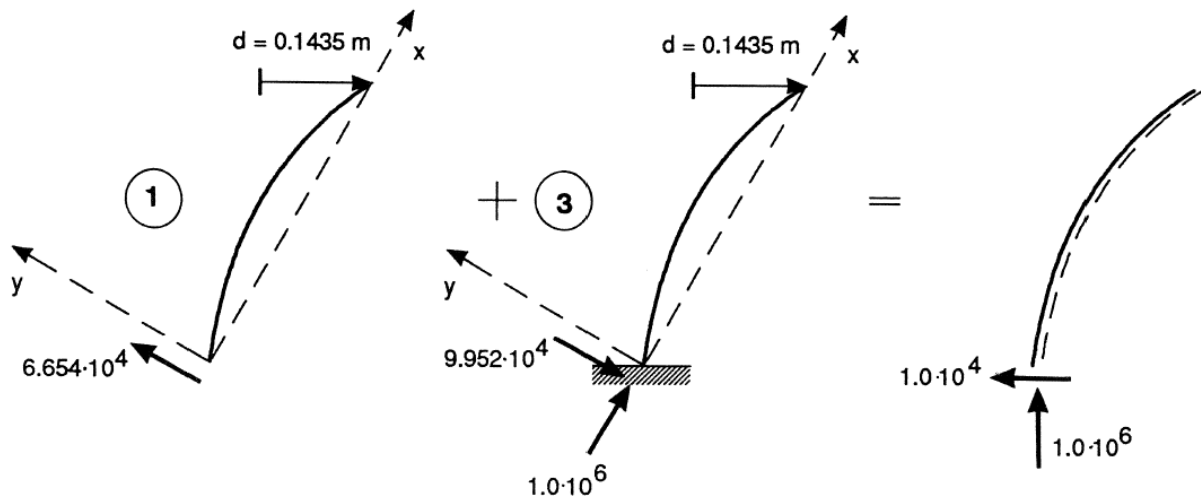
Figure 10-5   **Element force distribution at support for slave element 1 and master element 3 at load level 0.1*P1 and 0.1*P2**

The nodal force distribution for elements 1 and 3 at the support of the cantilever is shown in Figure 10-5. It is verified that the axial force is zero for the slave element 1. The shear force in element 3 is observed to be very large. This is due to the bending of element 1, giving a shear force in the opposite direction of element 3. Transforming the force state from local element system to the global axis system verifies that the internal force state is in equilibrium with the external loads.

For the reference case, when the linear dependencies are removed, the force state at a load level of $0.1 \, P_1$ and $0.1 \, P_2$ at the support of elements 1 and 3 are shown in Figure 10-6.
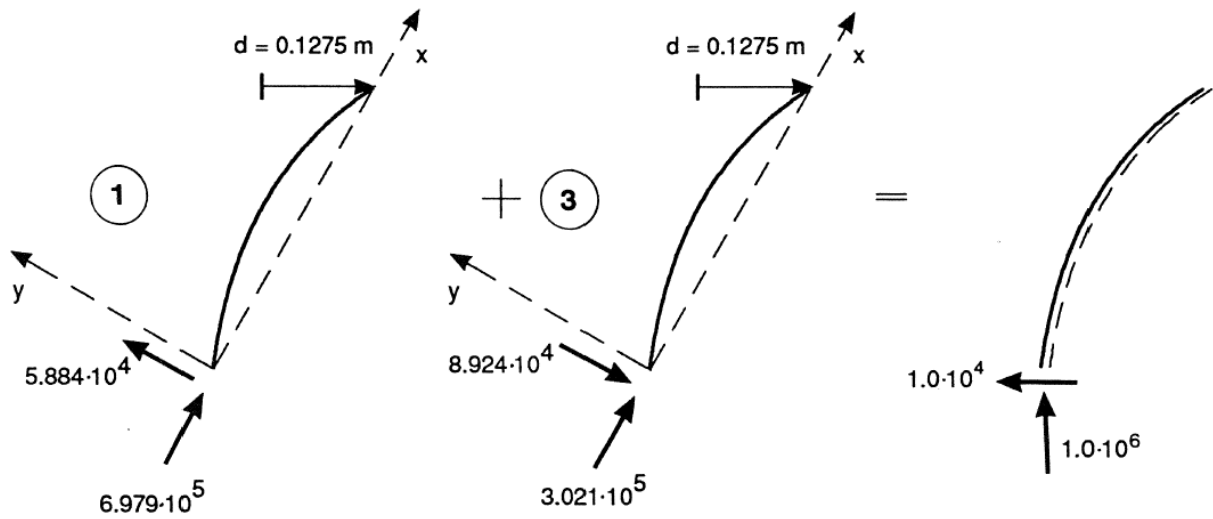
Figure 10-6   Element force distribution at support for the reference case at load level 0.1 P1 and 0.1 P2

As for the previous case, it is observed that bending of the element 1 introduces shear forces of the same magnitude as element 3. Compared to the linear dependency case the shear force distribution is slightly changed.

The nodal forces are transformed to the global axis system to document equilibrium with external loads.

Figure 11.2.5 shows bending moment diagrams for the two piles for load level 0.1 P_1 and 0.1 P_2. For comparison, an analysis where each of the piles are modelled with six elements is performed.

The bending moment diagrams in Figure 11.2.5b) confirm that the linear dependency condition is now active over a greater length. The sudden jumps in the diagrams for the bottom elements are due to the vanishing moment at the external pile support. The resulting bending moments satisfy, however, overall equilibrium.
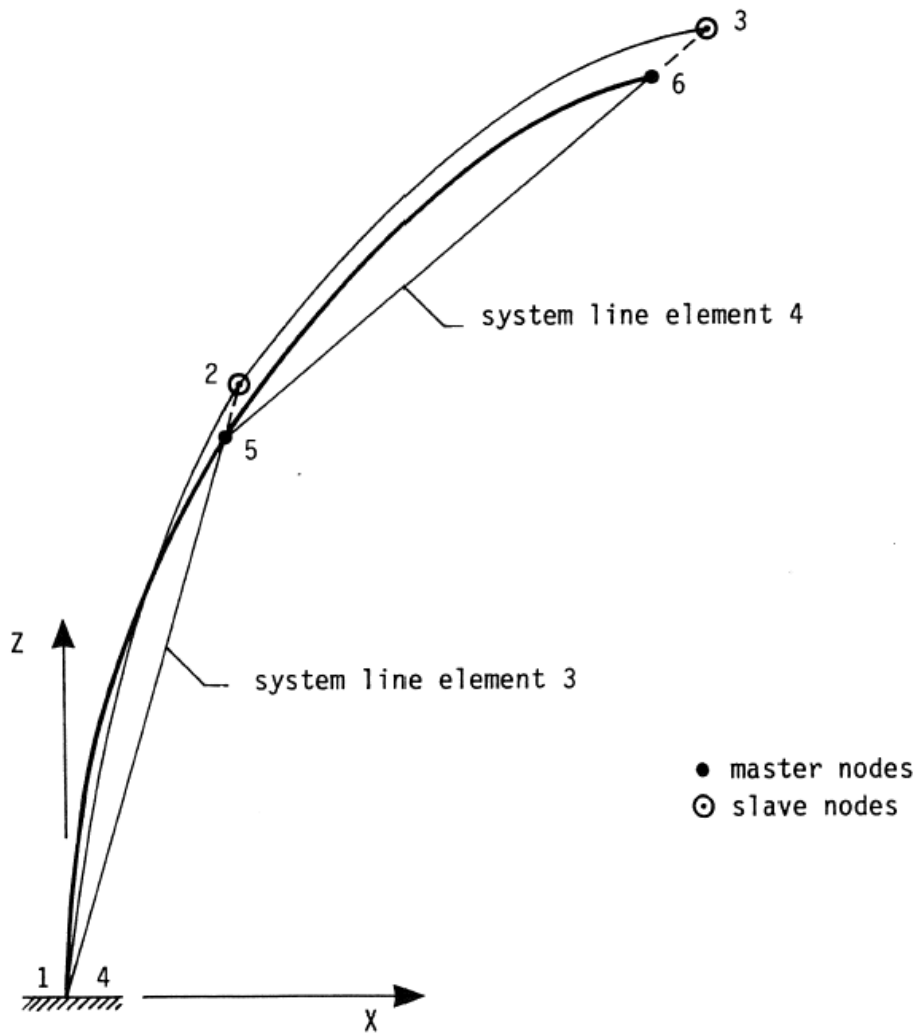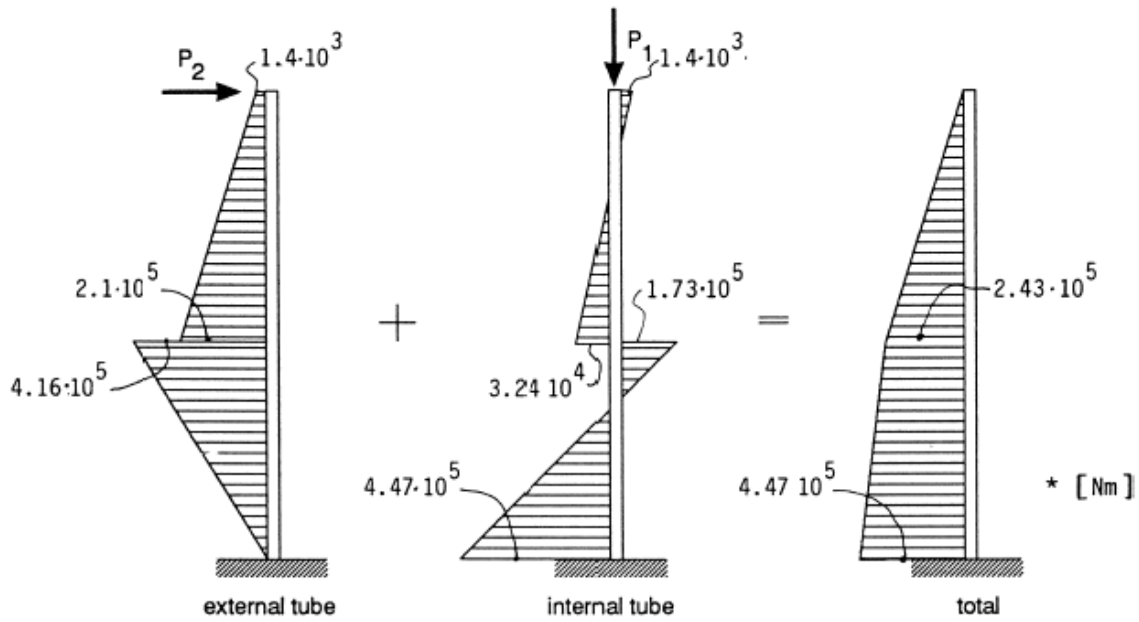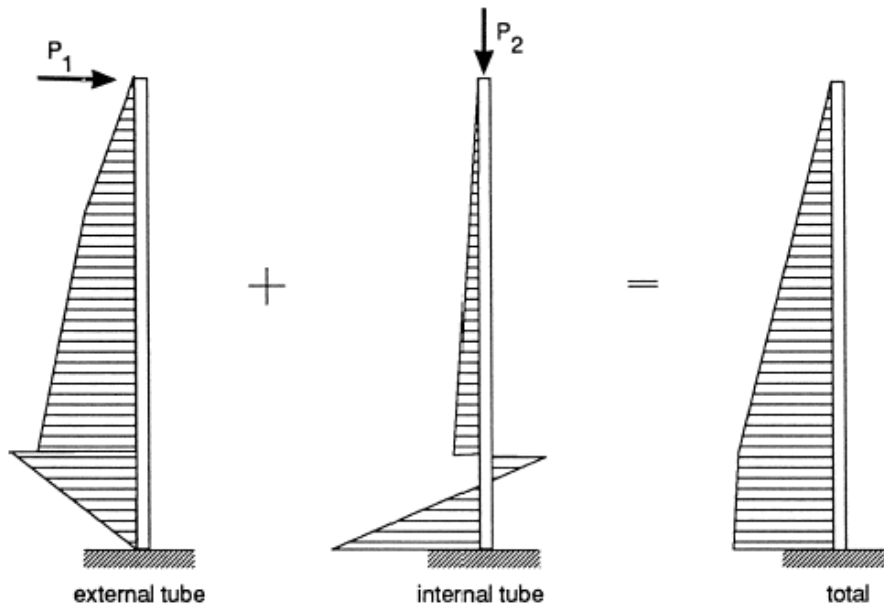
Figure 10-7 Illustration of slave and master node displacements

(a) Model with four elements, two in each pile

(b) Model with twelve elements, six in each pile

Figure 10-8 Bending moment diagrams of the two tubes

```
HEAD            TEST CASE LINEAR DEPENDENCY
        U S F O S  progressive collapse analysis
       S I N T E F  div  of  Structural  Engineering
'
'
'        inpri    outpri   termpri
CPRINT     1        2         1
'
'        epssol   gamstp   ifunc    pereul   ktrmax    dentsw    cmax   ifysw
CPROPAR  1.0E-20   0.10      2       0.05       5         0       999     0
'
'        nloads   npostp   mxpstp    mxpdis
CUSFOS    10       10       1.00       0.10
'        lcomb    lfact    mxld    nstep    minstp
          1        1.0      0.       1       0.001
          2        0.1      0.      10       0.001
'
'        matno    E-mod    poiss    yield    density    termX
MISOIEP    1     0.210E+12   0.3   0.248E+09  0.7850E+04  0.0
MISOIEP    2     0.210E+12   0.3  10.000E+09  0.7850E+04  0.0
'        matno    C1       A1
MPLASMON   1     0.015 0.25
MPLASMON   2     0.015 0.25
'
'        nodeno   ndof     dx dy dz rx ry rz
BNBCD      1        6        1  1  1  0  0  0
BNBCD      4        6        1  1  1  1  1  1
'
'        slave    master    coupled dofs
'        node     element  ix  iy  iz rix riy riz
BLINDP2     2        3       0   1   1   1   1   1
BLINDP2     3        4       0   1   1   1   1   1
```

List 10.2.1   USFOS control input file

11 COLLAPSE ANALYSIS

11.1 COLLAPSE ANALYSIS OF TUBULAR K-BRACE

This section compares USFOS analysis results with experimental test results for a K-braced section. Even though the load situation considered in this example is not comparable with the real load situation in a jacket, the example clearly demonstrates the capabilities of USFOS to realistically simulate the response for such types of subsystems.

The same structure is also analysed with the general FEM program FENRIS.

GEOMETRY AND LOADING

The K-brace consists of three tubular elements, one transverse beam and two diagonal braces. The geometry and dimensions are shown in the laboratory test set-up in Figure 11-1. The transverse beam is constrained against axial displacement and rotation at the supports.

The lower ends of the two diagonals are allowed to rotate freely in the plane of the frame. To prevent buckling out of the plane, the diagonals are clamped in the out-of-plane direction. At the joint, the transverse beam is reinforced by a thick-walled tube section, in order to avoid joint failure.
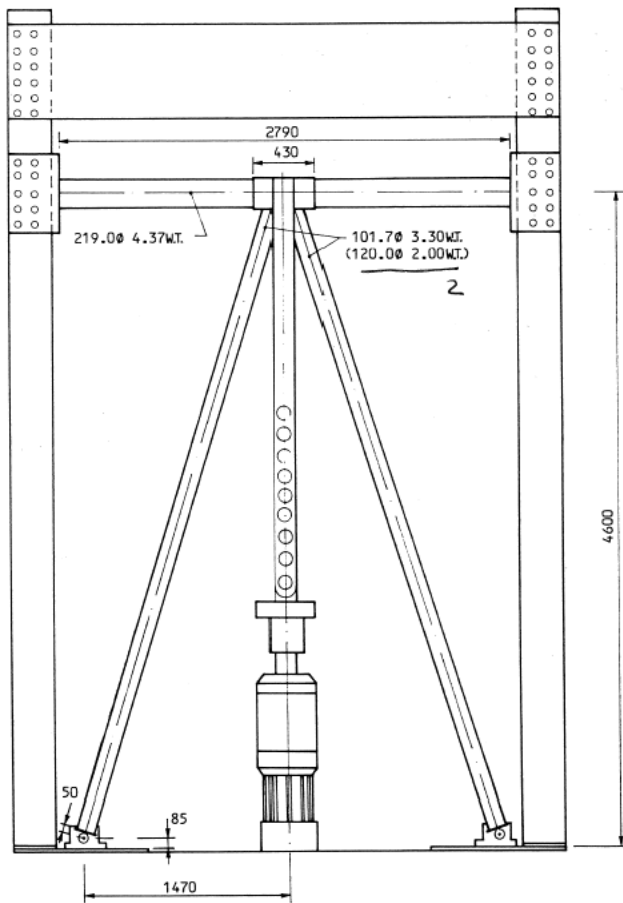
Figure 11-1 K-brace geometry and dimensions

The USFOS model consists of only 6 beam elements, one element for each of the transverse beam halves and two elements for each of the diagonals. Both the simple elastic-perfectly-plastic model and the more realistic model with gradual plastification and strain hardening was used in the simulations.

For the latter model the transition parameter was selected to a = 0.25 and the strain hardening was set to c = 0.015. The yield to bounding surface size ratio was selected to 0.79, the default value for tube cross sections.

The yield stress used is 420 MPa for the transverse beam and 343 MPa for the diagonals. The effect of local tube wall buckling is demonstrated in the simulated responses.

For the FENRIS analyzes the frame is modelled with 24 elements, 8 beam elements per member. The stress-strain relationship input is based on results from tension tests of the members.

RESPONSE

The vertical displacement at the beam/diagonal joint are for the various simulations compared to the experimental results in Figure 11-2 and Figure 11-3.

As the experimental curve shows, the system behaves elastic until local buckling and global instability occurs in the two bracing columns at a ultimate load approximately equal to 0.55 MN.

The system then unloads until equilibrium between external loads and internal resistance is restored. From this state further on-loading of the system is carried by beam bending and increasingly developing membrane action for the beam members.

At this stage large strains develops, leading to noticeable material hardening.
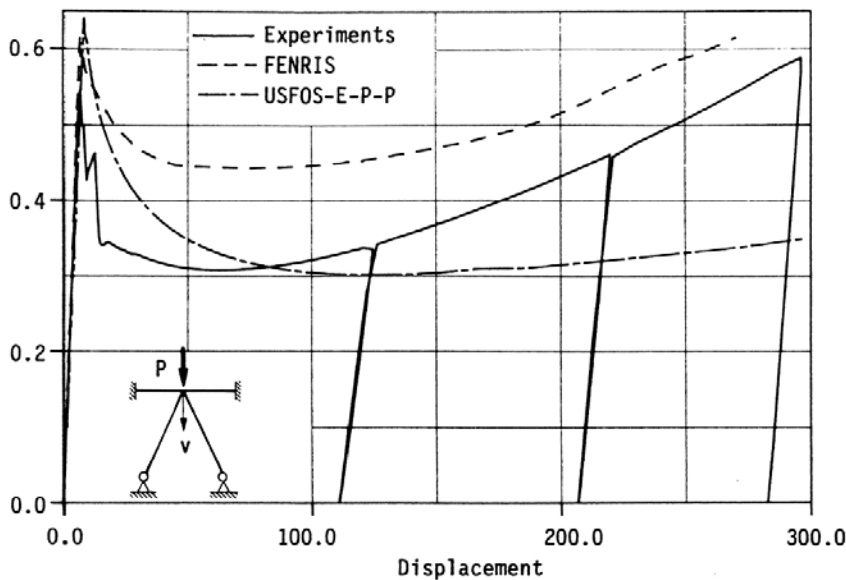

Figure 11-2   K-brace response using the USFOS elastic-perfectly-plastic model
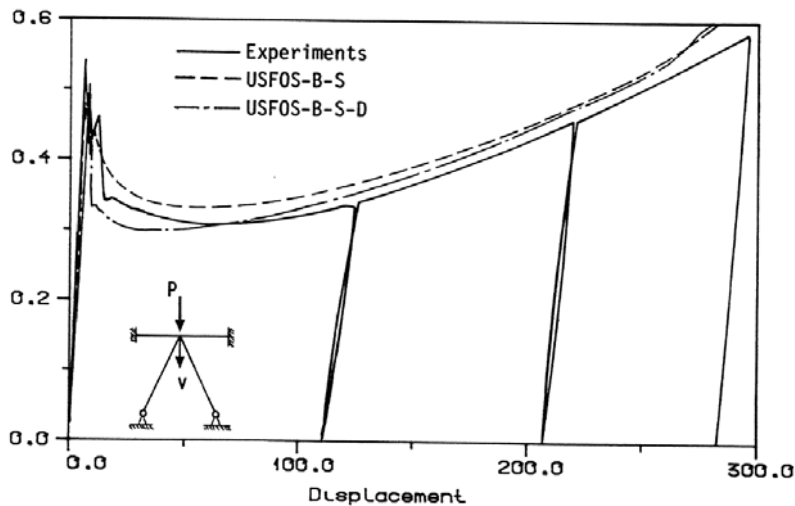
Figure 11-3   K - brace response using the USFOS two-surface model

With the simple elastic-perfectly-plastic material model (E-P-P), USFOS over predicts the ultimate load capacity. This is mainly because initial imperfections are neglected in the analysis and that this material model does not account for gradual plastification of the cross section.

The initial strength loss proceeding the ultimate load does not occur as dramatically as the experimental curve. For larger displacements the simplified USFOS model is observed to largely underestimate the load-carrying capacity. This discrepancy is due to the fact that strain hardening effects are not taken into account.

Figure 11-3 shows the response histories obtained when using the two surface material model, accounting for gradual plastification and kinematic strain hardening. The response history denoted (USFOS-B-S) accounts for initial out-of-straightness for the two bracing. The curve (USFOS-B-S-D) also accounts for local tube wall buckling as well as joint flexibility.

The USFOS simulations correlate well with the experimental results. USFOS predicts yielding at the two bracing members at a slightly to early stage. This is due to the simplifications included in the formulation of the material model.

The yield surface shape is taken as a scaled version of the bounding surface for the cross section instead of a straight line from Np/N=1.0, (see Chapter 3 of the theory manual /1/). Due to this simplification, yielding under pure compression occurs at a axial load equal to 0.79 Np instead of the exact value Np.

Furthermore, the material parameters a and c which shall be specified for each stress resultant are approximately chosen and have not been optimally tuned for the present case.

Without local tube wall buckling, the drop in capacity calculated by USFOS is not as sudden as the experiments indicate. With local buckling, the drop in capacity correlates well with the test, but occur at a slightly lower displacement.

Compared to the experimental results it is observed that USFOS is capable of representing the effect of local buckling in a realistic manner.

From Figure 11-3 it is also concluded that USFOS simulates the experiments very closely during the reloading of the system. The two response histories are seen to be practically parallel to the experimental curve, indicating accurate modelling of strain hardening effects as well as the development of membrane action.

The results obtained by FENRIS is shown in Figure 11-2. The ultimate load predicted by FENRIS is seen to be slightly overestimated, (0.61 MN). The rapid strength loss beyond the ultimate load is not predicted either.

This discrepancy may to some extent be explained by local buckling effects, which are not accounted for by the beam element in FENRIS. For large deformations the capacity is overestimated.

```
HEAD               K - FRAME
        U S F O S  progressive collapse analysis
      S I N T E F  div  of  Structural  Engineering
'
'
'         inpri    outpri   termpri
CPRINT    2        2         1
'         epssol   gamstp   ifunc     pereul   ktrmax   dentsw    cmax   ifysw
 CPROPAR  1.0E-20  0.20      2        0.05      5        1        999     0
'
'         nloads   npostp   mxpstp    mxpdis
CUSFOS    10       70       1.00      0.05
'         lcomb    lfact    mxld  nstep    minstp
          1        0.25     5.0    0       0.005
          1        0.05     0.0    40      0.005
          1        0.25     0.0    75      0.005
'         ncnods
CNODES    1
'         nodex    idof     dfact
          1        3        1.
'      impgroup  impshape  angle   offset    dent1    dent2    dentmid
GIMPER    1        0        0       0.00056   0.0      0.0      0.0
GIMPER    2        0        0       0.00062   0.0      0.0      0.0
'         elnox   impgroup
GELIMP    3        1
GELIMP    4        2
'         matno   e-mod     poiss   yield     density     therm.expan
MISOIEP   1       0.210E+12  0.3   0.420E+09  0.7850E+04  1.45E-5
MISOIEP   2       0.210E+12  0.3   0.343E+09  0.7850E+04  1.45E-5
'         matno   C1        A1
MPLASMON  1       0.015     0.50
MPLASMON  2       0.015     0.50
'         geono    z-yield
GBOUND    1        0.79
SHELL  1.0 1.0  2.0
```

Table 11.1-1 USFOS control input file

11.2 COLLAPSE ANALYSIS OF SPACE FRAMES

This section compares USFOS analysis results with experimental test results for a 3-D X-braced structure. Analysis results obtained by USFOS are also compared to the FEM program FENRIS /11/, /12/.

GEOMETRY AND LOADING:
The chosen structural system may be regarded as a subsystem of a four-legged jacket structure. Many of the important effects associated with inelastic behaviour and force redistribution taking place in a large jacket structure can as well be evaluated studying a smaller subsystem /11/.

The two structural models considered, shown in Figure 11-4 and, have similar geometries but their dimensions are different. The frame structure is seen to have X-braces in the top horizontal plane as well as in the four vertical planes.
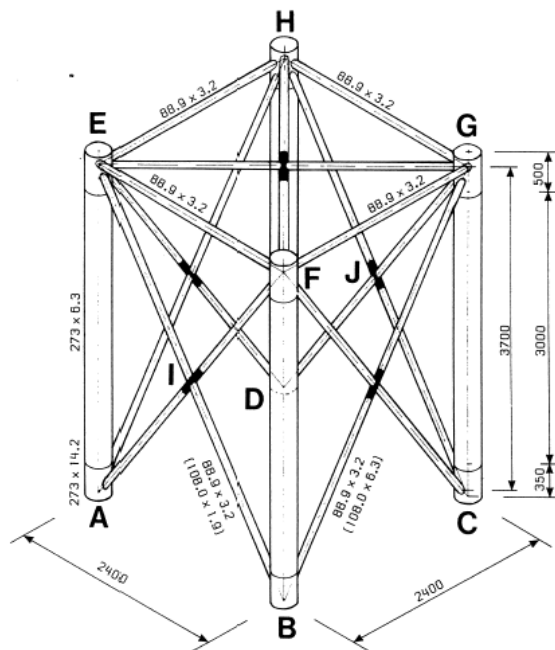
Recorded yiels stresses for test frames

Member D/W.T	Yield stresses σ_y [MPa]	Ultimate stress σ_y [MPa]
273.0/6.3	299	357
88.9/3.2	367	419
88.9/6.6	319	471
120.0/1.9	231	297

Figure 11-4   3D system tested experimentally

Figure 11-4 and Figure 11-5 show the member arrangement, main dimensions and the corresponding member dimensions for the two models, and other key parameters.

Figure 11-4 shows the X-braced frame tested in the laboratory. The member dimensions as well as measured yield and ultimate stresses obtained from tensile tests are given in Figure 11-5.

In order to reduce the influence of nodal joint flexibility and to avoid premature collapse of joints, the wall thickness of the leg tubes was increased locally. Tube EF was fabricated with increased thickness to prevent buckling during load application.

A horizontal load was applied on top of the frame leg AE in the direction of member EF.

The USFOS model consisted of 28 elements. No initial imperfections were given for the analysis because such measurements were not taken prior to testing. The external load was applied incrementally without equilibrium iterations up to the ultimate strength.

The structural system shown in Figure 11-5 has been used in a extensive study of 3-D frame structures /11/ using the non-linear program FENRIS. This frame was also analysed with USFOS, for comparison.

The FENRIS model consisted of 108 beam elements and 93 nodal points. An elastic-perfectly-plastic material law with a yield stress of 330 MPa was used. The USFOS model consisted of on single tubular beam element per structural member, totally 28 elements.

The simplified material model, defining elastic-perfectly-plastic behaviour on the stress resultant level was selected. The loads applied were concentrated forces F_v=30 MN applied in the vertical direction and F_h=120 MN acting horizontally at each of the positions E and F.

The undamaged structure was analysed assuming small imperfections, typically do/L=0.0015 was selected.
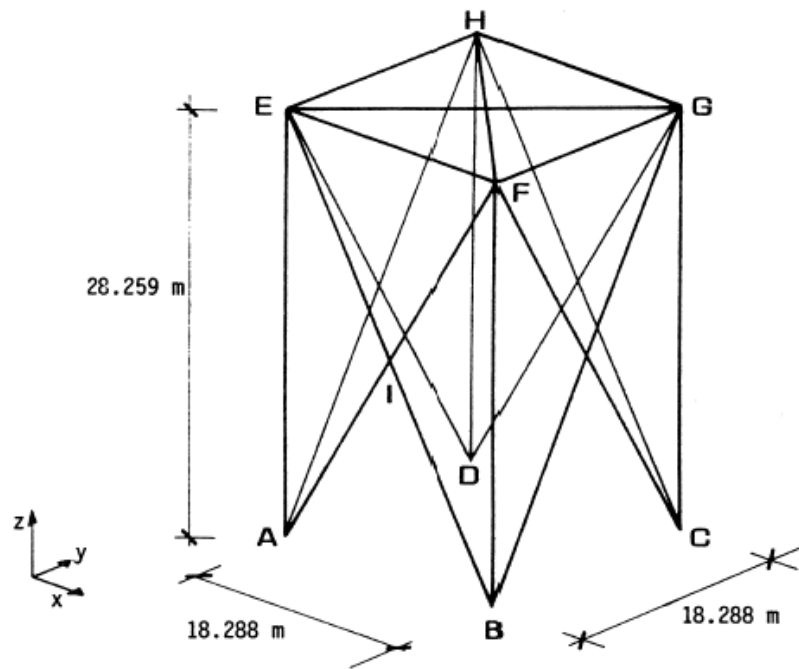
Dimensions for members in 3-D X-braced systems. / 11 /

MEMBER TYPE	SYSTEM	D [m]	t [m]	L [m]	N_p [MN]	M_p [MNm]	D/t	L/r
Legs	S1, S2	2.0	0.060	28.259	120.67	74.54	33	41
Horizontals	S1, S2	1.0	0.040	18.288	39.80	12.17	25	54
Horizontal X-brace	S1, S2	1.0	0.040	25.86	39.80	12.17	25	76
Vertical	S1	1.016	0.038	33.66	38.53	12.00	26.7	97
X-braces	S2	0.508	0.019	33.66	9.63	1.50	26.7	195

Figure 11-5 3D system analysed by FENRIS and USFOS

RESPONSE:

Comparison between USFOS and experiment:

Experimentally obtained response behaviour for the system in Figure 11-4 is shown with dotted lines in Figure 11-6. The external load is plotted versus X-displacement at node E. It is observed that the system experiences a gradually stiffness degradation, and buckling occurs in member EB at a load level about 400 kN.

At this point, fracture also takes place in member IF. This failure is caused by the lack of fusion in the welds at node I. The fracture causes a sudden drop in the external load and during further displacement of the structure some strength is regained. The structure continues to deform until a new fracture occur, this time in member JG at node J. This enforces another drop in the load carrying capacity.

The corresponding response calculated by USFOS /13/, is shown with the solid line in Figure 11-6. The fractures observed during the experiments were in the numerical analyses simulated by introducing a negative yield force once the fully plastic tensile force is reached and the structural member is removed.

Because equilibrium iterations are not performed, a corresponding drop in external load must be expected. The maximum load is predicted reasonably well. However, the displacement at node E differ significantly. This may partly be due to the simplified material model which does not account for partial yielding of the cross section, and thus gives a more abrupt change of stiffness.

Furthermore, initial member imperfections may have been present and gradual fracture of the joint may have taken place. Subsequent to fracture the load level is predicted quite well, although the displacements continues to differ. However, this part of behaviour is sensitive to the choice of fracture criterion, which here is taken as initiation of fully plastic tension.

The axial forces measured in the experiment may differ from the calculated values. However, it is observed that the general behaviour of the structure and of each element is predicted correctly. Furthermore, it should be taken into consideration that the measurements are not "exact" in the sense that uncertainties are associated with the measured elastic modulus, yield stress and tube wall thickness.

It is also observed that the initial stiffness is reasonably well predicted. An exception to this is the braces EB and FA. The reason for this discrepancy is unknown. Buckling of member EB causes redistribution of forces to other members. This process is somewhat delayed in the theoretical calculations due to a more sudden and late buckling of EB. It is noticed that the axial forces remain almost unchanged during fracture.
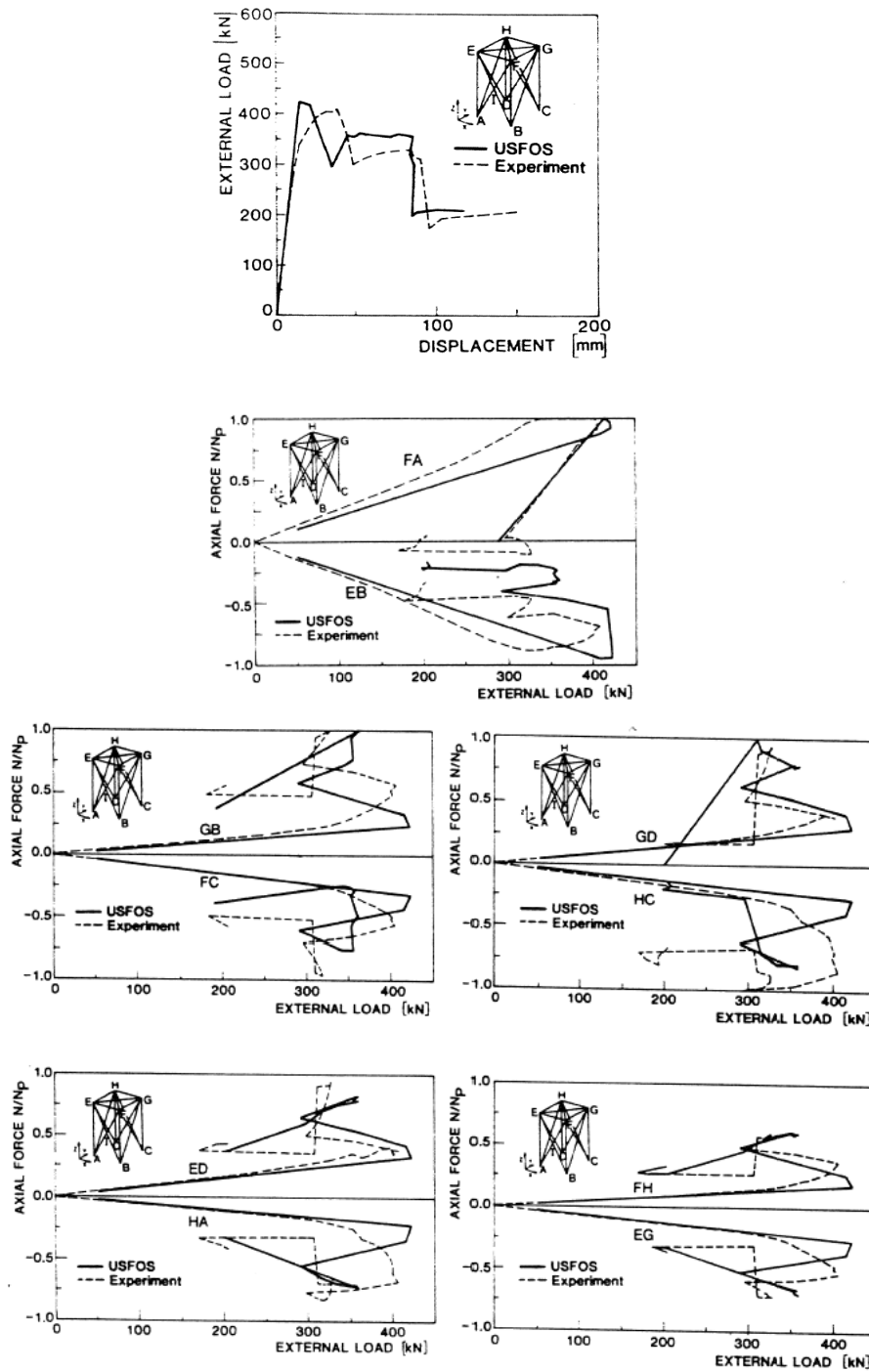
Figure 11-6   Comparison between USFOS predictions and experiments
a)   External load versus x-displacement at node E
b)   Brace axial force versus external load

Comparison between USFOS and FENRIS:

In Figure 11-7the horizontal response calculated by USFOS and FENRIS, for the system shown in Figure 11-5, is compared for the two load-cases considered. The results are observed to be in good agreement regarding the ultimate load capacity.

The initial stiffness in the elastic region calculated by the respective numerical formulations shows some deviations. As observed USFOS overestimates the elastic stiffness slightly compared to FENRIS.
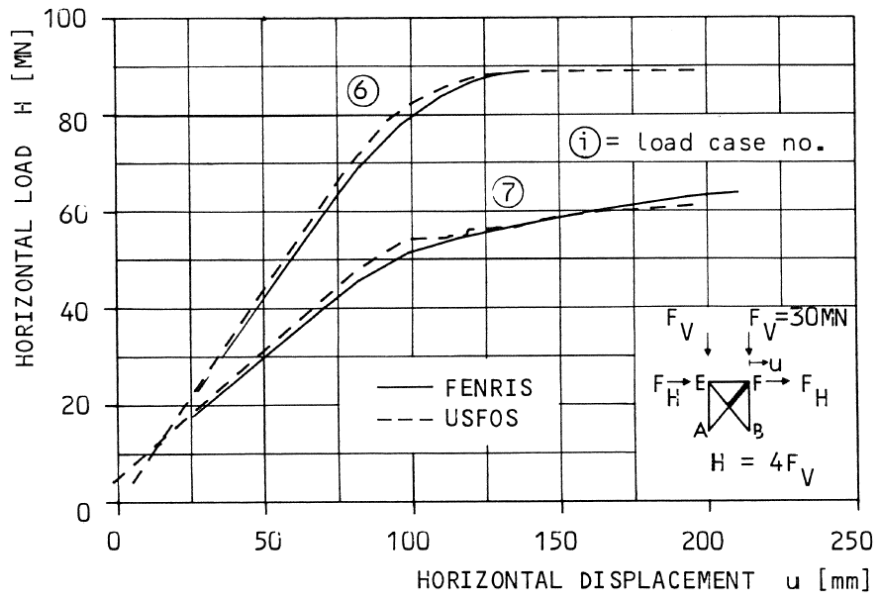
Figure 11-7 Numerically calculated load-displacement curves for 3D system

```
HEAD                 3D - FRAME
        U S F O S  progressive collapse analysis
       S I N T E F  div  of  Structural  Engineering
'
'
'       inpri    outpri    termpri
CPRINT    5         2        1
'       epssol   gamstp   ifunc    pereul   ktrmax   dentsw    cmax ifysw
CPROPAR  1.0E-20   0.30    2        0.01      5        1        999   1
'       nloads   npostp   mxpstp    mxpdis
CUSFOS    10       20      1.00     0.025
'       lcomb    lfact    mxld    nstep     minstp
          1       0.25    0.0       0        0.005
'         1       0.25    0.0      14        0.005
'         1       0.02    0.0      11        0.001
'         1       0.01    0.0      30        0.001
'         1       0.05    0.0      20        0.005
'         1       0.01    0.0       9        0.001
'         1       0.001   0.0      10        0.0001
'         1       0.01    0.0       9        0.001
'         1       0.002   0.0       5        0.0002
'         1       0.05    0.0      50        0.005
'       ncnods
CNODES    1
'       nodex    idof     dfact
          9        1        1.
'     impgroup  impshape  angle   offset   dent1   dent2   dentmid
GIMPER    1         0        0      0.0      0.0     0.0     0.0185
'       elnox   impgroup
GELIMP    7        1
'       matno    E-mod    poiss    yield    density
MISOIEP    1      0.210E+12   0.3   0.299E+09  0.7850E+04
MISOIEP    2      0.210E+12   0.3   0.367E+09  0.7850E+04
MISOIEP    3      0.210E+12   0.3   0.319E+09  0.7850E+04
MISOIEP    4      0.210E+12   0.3   0.231E+09  0.7850E+04
MISOIEP    5      0.210E+12   0.3   0.219E+09  0.7850E+04
```

List 12.2.1   USFOS control input file

12 GROUTED MEMBERS

12.1 CROSS-SECTIONAL PROPERTIES

Example 1

The cross-sectional properties are checked against interaction curves for Durocrit D4 for a D/t = 40. Reference is made to Table 7.2, page 34 in report Development of a Grouted Beam Element for Pushover Analysis. Figure 12-1 shows the interaction curve derived form non-linear shell analysis of the grouted tube. It is noticed that the maximum resistance in compression is 3.2 MN and in bending 74.6 kNm.

The present analyses are carried out for a tubular beam with diameter D = 160 mm, thickness t = 4 mm and length L = 2.4 m. The tube, which is pinned at the ends, is subjected to axial compression. The axial force increases initially until the tube buckles and deforms laterally giving a rapid increase of the bending moment at midspan. The force bending moment interaction is recorded at mid-span and is shown in Figure 12-2. The figure demonstrates that USFOS predictions are in good agreement with the results of the nonlinear shell finite element simulation.

Table 7-2 Comparison between FE analyses and EC4 for Ducorit®D4, D/T 40.

40 - D4					
Grout:	Ducorit®D4				
D/T:	40				

F	EC4		Analysis		Analysis /EC4
	M	N	M	N	
A	0.0	3.3	0	3.2	0.97 (N)
B	44.5	0.0	42.8	0	0.96 (M)
C	44.5	2.6	41.4	2.6	0.93 (M)
D	75.2	1.3	74.6	1.3	0.99 (M)
E	20.0	3.0	-	-	-
F	0	-0.8	0	-0.7	0.92 (N)
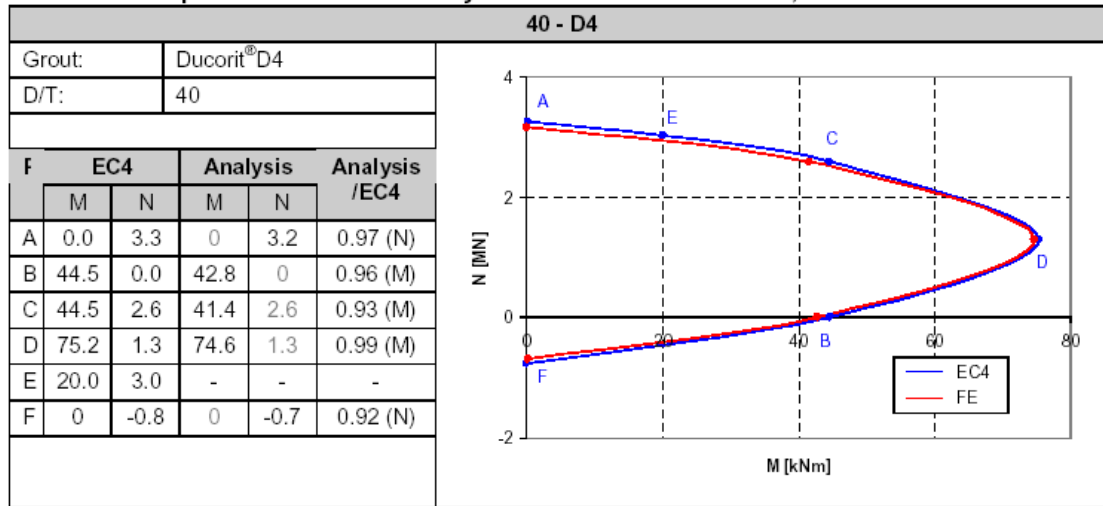
Figure 12-1 Interaction curve for Durocrit D4
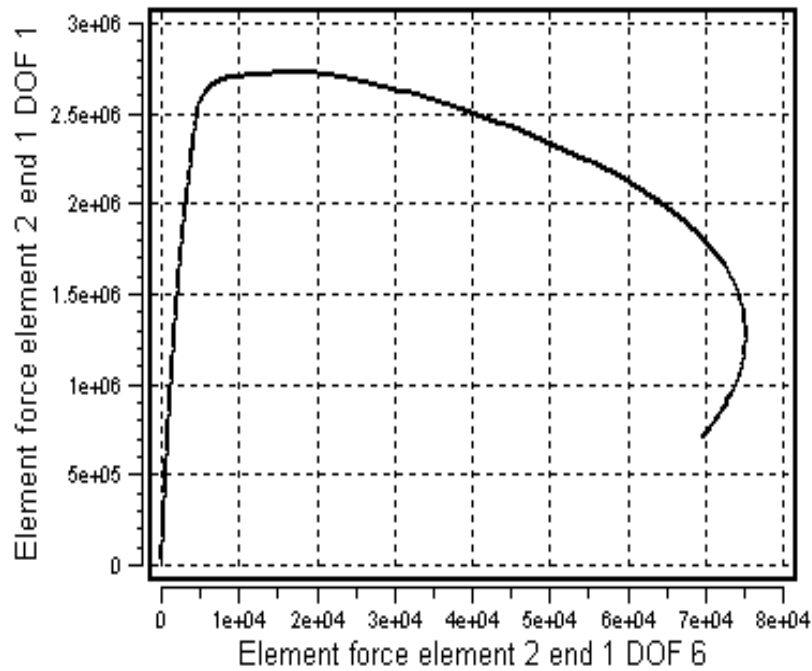

Figure 12-2 Interaction curve simulated with USFOS for Durocrit D4, D/t = 40
        Case 1 M-Red = 1.0

Next, analysis is carried out assuming the grout bending moment factor to M-Red = 0.01. This yields a bending moment resistance of equal to M_B = 43 kNM. The results of the simulation are plotted in Figure 12-3. The behavior is very satisfactory. For small axial force the bending

moment appears to be slightly larger than 43 kNm, but this is due to strain hardening in the steel tube.

Figure 12-4 shows results with the grout bending moment factor M-Red = 0.5. This yields a bending moment resistance $M_D^{'} = M_B = 60\,kNm$ and corresponding axial force $N_D^{'} = 0.39\,MN$. Again, the behavior is very satisfactory. The apparent, slight overprediction of bending moment for small axial force is due to strain hardening in the steel tube.
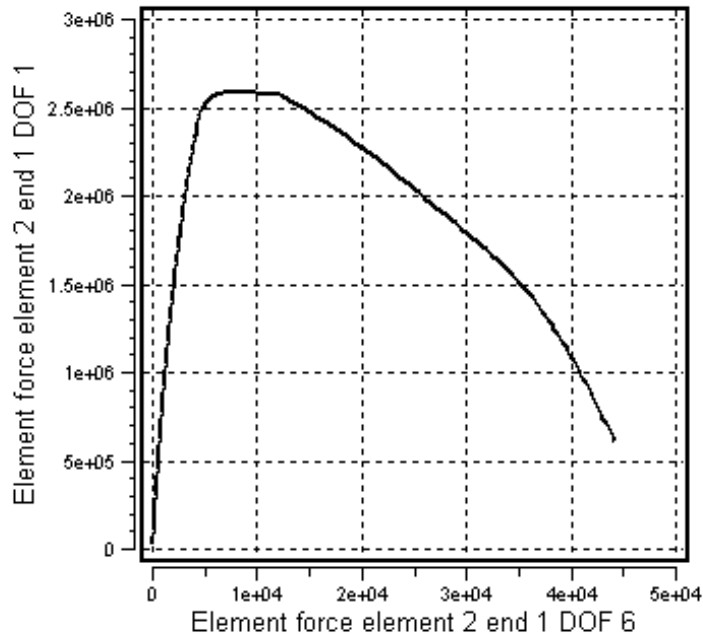

Figure 12-3 Interaction curve for Durocrit D4 – moment reduction factor M-Red = 0.01. Case 2 M-Red = 1.0 Maximum bending resistance $M_D^{'} = M_B = 43\,kNm, \quad N_D^{'} = 0\,MN$
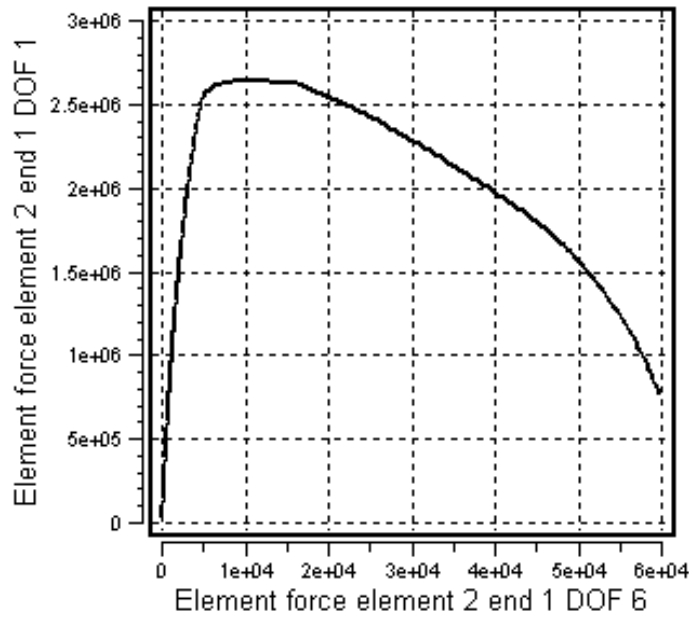
Figure 12-4 Interaction curve for Durocrit D4 – moment reduction factor $c_M = 0.5$.

Case 2 M-Red = 1.0 Maximum bending resistance

$$M_D^{'} = M_B = 60 \, kNm, \quad N_D^{'} = 0.39 \, MN$$

In the case analyzed the elastic modulus of steel is $E_s = 2.1 \cdot 10^5$ MPa and for the grout $E_s = 0.686 \cdot 10^5$ MPa. The area of the steel tube is $A_s = 1.960 \cdot 10^{-3}$ m^2 and the area of the grout is $A_s = 5.930 \cdot 10^{-3}$ m^2. This yields an equivalent area of

$$A_{eq} = A_s + \frac{E_g}{E_s} A_g = 7.89 \cdot 10^{-3} \, m^2$$ This area is identical to the one produced by USFOS.

Correspondingly, the equivalent moment of inertia is calculated to be $$I_{eq} = I_s + \frac{E_g}{E_s} I_g = 1.45 \cdot 10^{-5} \, m^4$$ when the moment of inertia of steel and grout is $I_s = 5.97 \cdot 10^{-6}$ m^4 and $I_g = 8.56 \cdot 10^{-6}$ m^4

The equivalent axial stiffness for the column becomes:

$$K = E_s \, A_{eq} / L = 690 \, MN / m$$

The force level for an end shortening of 3 mm then becomes 2.07 MN. This agrees very well with the force – end shortening relationship for the column calculated with M-Red = 1.0, see Figure 12-5
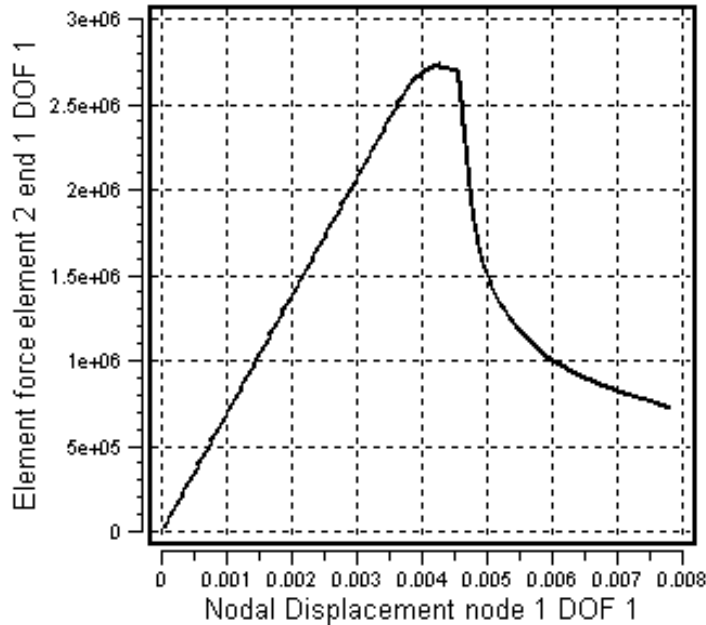
Figure 12-5 Force – end shortening relationship for Case 1 with M-Red = 1.0

Example 2

Figure 12-6 shows the bending moment axial force interaction when the beam, now with *axially fixed ends*, is subjected to a lateral, concentrated force at mid-span. The beam deforms initially in bending, and, as the deformation becomes finite, a tensile axial force develops. When the bending moment- axial force reaches the plastic surface, the axial force becomes compressive for a while. This rather strange behaviour is due to the fact that the steel pipe, which acts in tension, elongates due the plastic straining. This elongation causes the axial force to become compressive. By further loading, the elongation due to lateral deformation overrides the expansion caused by the steel and the beam once again enters the tension region.

The behaviour predicted by USFOS is exactly according to theory and is believed to be a true physical effect.
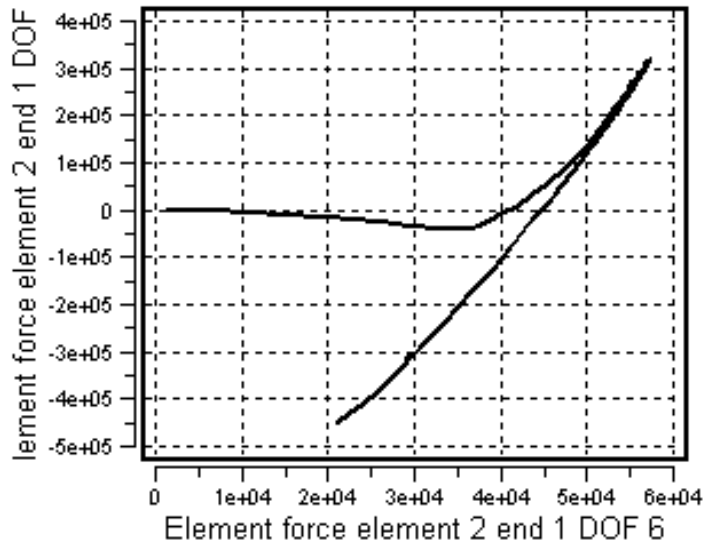
Figure 12-6 Bending moment-axial force interaction for ba beam with a concentrated load at mid span - axially fixed ends. Note the intermediate compressive axial force induced by plastic elongation of the steel during the bending phase.

12.2 COMPARISON WITH GROUTED COLUMN BUCKLING TESTS

In this section the grouted beam model is compared with results from column buckling tests carried out at Chalmers, Chalmers University of Technology (1999). The tests and comparison FE analysis are also described in two reports by Offshore Design, Offshore Design (200) and Haukaas and Yang (2000). The information given in Section 12.2.1 is taken from the report by Haukaas and Yang.

12.2.1 Description of the experimental study

The tests specimens consist of a circular pipes with diameter D = 160 mm, thickness t = 4.5 mm and length L = 2500 mm. The pipes are filled with various types of grout. At the ends the specimens are supported by roller bearings located eccentrically to the pipe axis, thus producing an end moment in addition to axial compression, refer Figure 12-7.

Figure 12-7 Test geometry

The tests set-up and post-buckling shape of a test specimen are illustrated in Figure 12-8 while Figure 12-9 shows a close view of the support arrangement.

Figure 12-8 Test set-up and column in post-buckled condition

Figure 12-9 Support arrangement for the columns

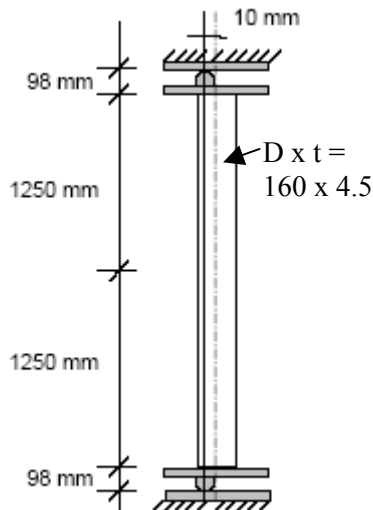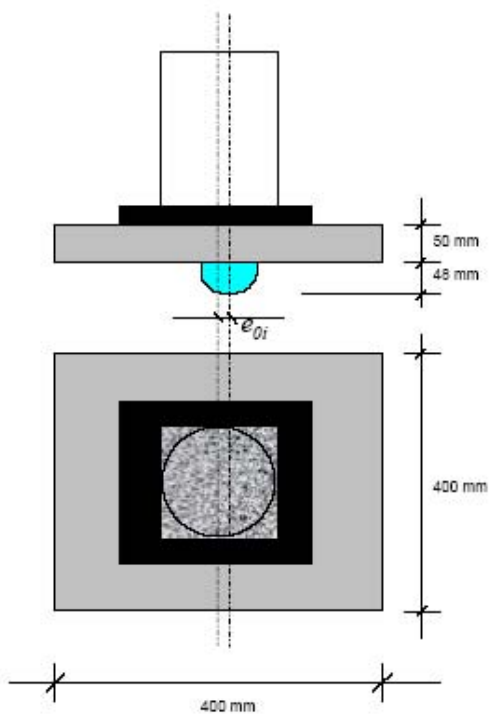Tests are carried out for two steel materials ("High" and "Low" yield stress) and with three types of grout; Durocrit D4, Durocrit S5 and Densiphalt. In addition a few tests are carried out with ungrouted specimens. The test matrix is shown in Figure 12-10.

Results from tension coupon tests for the steel and grout material are shown in Figure 12-11 and Figure 12-12, respectively. The quoted values of the yield stress and elastic modulus are used in the simulations. He steel exhibits significant strain hardening.

Table 8-3   Test specification for test series 4 – Column capacity. Unit [mm]

TEST No	Column dim. (1)	Steel type	Grout Type	Concrete mix.
1a	160.0 x 4.50	A	No	No
1b	160.0 x 4.50	B	No	No
1c	160.0 x 4.50	B	No	No
2a	160.0 x 4.50	B	Ducorit® D4	2 vol.% steel fibres
2b	160.0 x 4.50	B	Ducorit® D4	2 vol.% steel fibres
2c	160.0 x 4.50	B	Ducorit® D4	2 vol.% steel fibres
3a	160.0 x 4.50	A	Ducorit® D4	No
3b	160.0 x 4.50	B	Ducorit® D4	No
3c	160.0 x 4.50	B	Ducorit® D4	No
4a	160.0 x 4.50	B	Ducorit® S5	2 vol.% steel fibres
4b	160.0 x 4.50	B	Ducorit® S5	2 vol.% steel fibres
4c	160.0 x 4.50	B	Ducorit® S5	2 vol.% steel fibres
5a	160.0 x 4.50	B	Ducorit® S5	No
5b	160.0 x 4.50	B	Ducorit® S5	No
5c	160.0 x 4.50	B	Ducorit® S5	No
6a	160.0 x 4.50	B	Ducorit® S5	5 % SKT
6b	160.0 x 4.50	B	Ducorit® S5	5 % SKT
6c	160.0 x 4.50	B	Ducorit® S5	5 % SKT
7a	160.0 x 4.50	A	Densiphalt	No
7b	160.0 x 4.50	B	Densiphalt	No
7c	160.0 x 4.50	B	Densiphalt	No

Notation
Steel type   Steel type A : σ_{fy} = 491 MPa, Steel type B : σ_{fy} = 344 MPa
SKT   Shrinking compensated concrete

Note

(1)   It should be noted that new material tests for the steel sections have been done. These tests were done on cut out from the tested columns. The cut out was performed in section which has not been subjected to yielding near the column ends.

Figure 12-10 Test matrix (ref. Haukaas and Yang, 2000)

Table 8-4   Stress – strain curves as applied in the analyses. The "bold" numbers have been "defined" as the yield stress. Note that this do not comply with the general definition of yield stress, i.e., the stress which corresponds to 0.2% plastic strain.

1A		1B		3A		3B/3C	
Strain [%]	Stress [MPa]	Strain [%]	Stress [MPa]	Strain [%]	Stress [MPa]	Strain [%]	Stress [MPa]
0.00	0	0	0	0.00	0	0	0
0.16	325	0.11	240	0.30	415	0.11	230
0.28	**415**	**0.23**	**275**	**0.30**	**415**	**0.24**	**292**
0.46	424	0.73	280	0.91	440	1.15	310
0.91	435	1.91	333	2.27	575	2.65	320
2.28	565	4.19	389	4.33	690	5.18	385
5.35	721	8.21	440	8.38	790	10.2	450
10.41	820	17.21	500	13.4	836	22.4	500
30.40	820	20.26	550	30.4	836		
		30.26	550				

Table 8-4 (Cont).

5A/5B/5C		7A		7B		7C	
Strain [%]	Stress [MPa]	Strain [%]	Stress [MPa]	Strain [%]	Stress [MPa]	Strain [%]	Stress [MPa]
0.00	0	0	0	0.00	0	0	0
0.10	208	**0.21**	**450**	0.12	245	**0.14**	**300**
0.23	275	0.32	455	**0.32**	**262**	3.65	310
0.30	**295**	1.52	455	1.63	270	5.16	340
0.74	296	2.25	534	4.17	360	10.2	410
2.14	300	4.31	648	8.20	410	20.2	460
4.18	357	8.35	737	13.2	455	30.2	460
8.20	425	13.4	793	17.2	480		
30.26	550	17.4	820				

Figure 12-11 Stress-strain relationships for steel

Table 8-5   Grout properties as applied in the FE analysis

TEST No	Grout Type	Poisson ratio	Compressive Strength	Tensile Strength	E-modulus
3A/B/C	Ducorit®D4	0.19	215.2 MPa	11.3 MPa	71 000 MPa
5A/B/C	Ducorit®S5	0.19	132.3 MPa	9.0 MPa	56 300 MPa
7A/B/C	Ducorit®S1	0.18	115.1 MPa	7.5 MPa	29 000 MPa

Table 8-6 Grout properties as given as FE input

TEST No	Grout Type	Shear modulus	Bulk modulus	Compressive Pressure	Tensile Pressure	Volumetric strain at yield
3A/B/C	Ducorit®S5	23655 MPa	30269 MPa	44.1 MPa	3.0 MPa	0.146 %
5A/B/C	Ducorit®D4	29832 MPa	38172 MPa	71.7 MPa	3.8 MPa	0.188 %
7A/B/C	Ducorit®S1	12288 MPa	15104 MPa	38.4 MPa	2.5 MPa	0.254 %

Figure 12-12 Grout material properties

12.2.2   USFOS simulation of buckling tests

For the USFOS simulation the column is modelled with two beam elements. The ends are modelled as simply supported. The eccentricity is taken into account by applying an end moment corresponding to the moment produced by the eccentricity. The axial force and end moment are increased proportionally.

The column is given an initial shape distortion of 0.001 times the column length, i.e. 2.5 mm in the "high" yield stress analyses and 0.002 times the column length , i.e. 5 mm in the low yield stress analyses. The difference was not aimed at, but has a moderate influence on the results.

The shape distortion is applied as a displaced (middle) node in the direction of the displacement caused by the end eccentricity.

All analyses are run assuming full plastic bending capacity, i.e. $M_{Red} = 1.0$

The axial force − lateral displacement relationships for the tests are compared with USFOS simulations in Figure 12-14 for tests with high yield stress and in Figure 12-16 for tests with low yield stress. The test curves are reconstructed from Figure 12-13 and Figure 12-15, taken from the report by Haukaas and Yang (2000).

The results form USFOS simulations are in very good agreement with the tests where the pipes are grouted with either Durocrit D4 or Durocrit S5. The accuracy is comparable to the one obtained with nonlinear finite element shell analysis of the tests, as reported by Haukaas and Yang (2000).

As concerns the tests with Densiphalt as grout material, the agreement is fairly poor. This is attributed to poor properties of Densiphalt, not deficiency of the developed calculation model as such. The disagreement with tests results are also observed for the nonlinear shell analyses.

A significantly better agreement with the Densiphalt tests may be obtained using a reduced value of the Densiphalt yield stress. No attempt is, however, made in the present investigation to determine such a reduced yield stress.

The USFOS cross-sectional model is based on a two-surface yield hinge concept. The inner surface represents initial yielding and the outer surface the fully developed plastic surface. For ungrouted pipes, the default value is 0.79 corresponding to the ratio on initial yield moment and fully plastic moment.

In case of grouted section it is likely that the grout starts "yielding" prior to yielding of the pipe, hence the yield surface should be smaller than the one used for ungrouted sections. On the basis of the results shown in Figure 12-14 and Figure 12-16, it seems that a yield surface size of 0.6 is a reasonable default value as concerns back-calculation of tests.
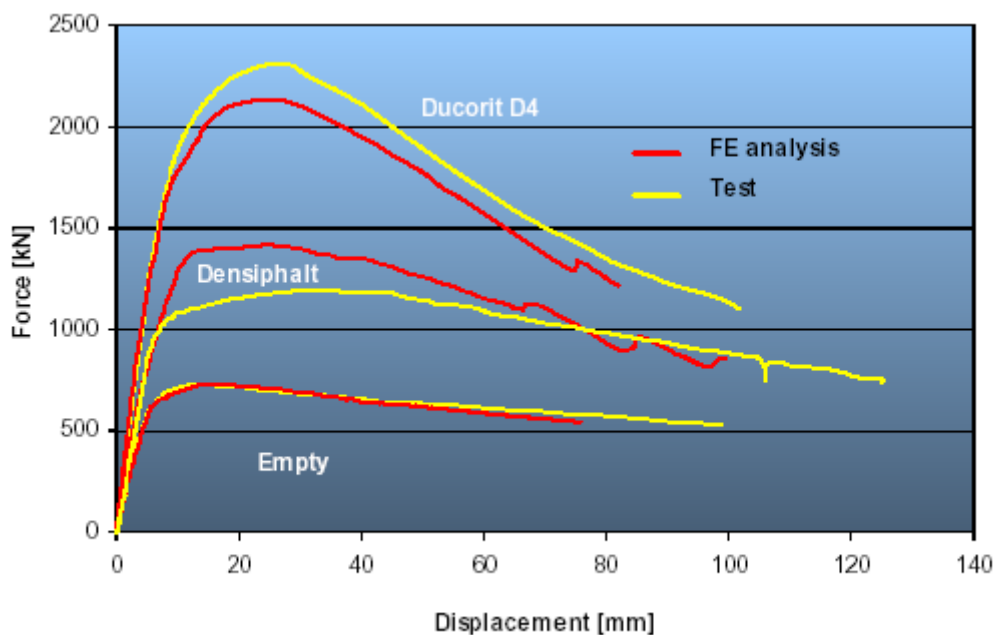

Figure 12-13 Force versus lateral displacement - tests with high yield stress, Haukaas and Yang (2002)
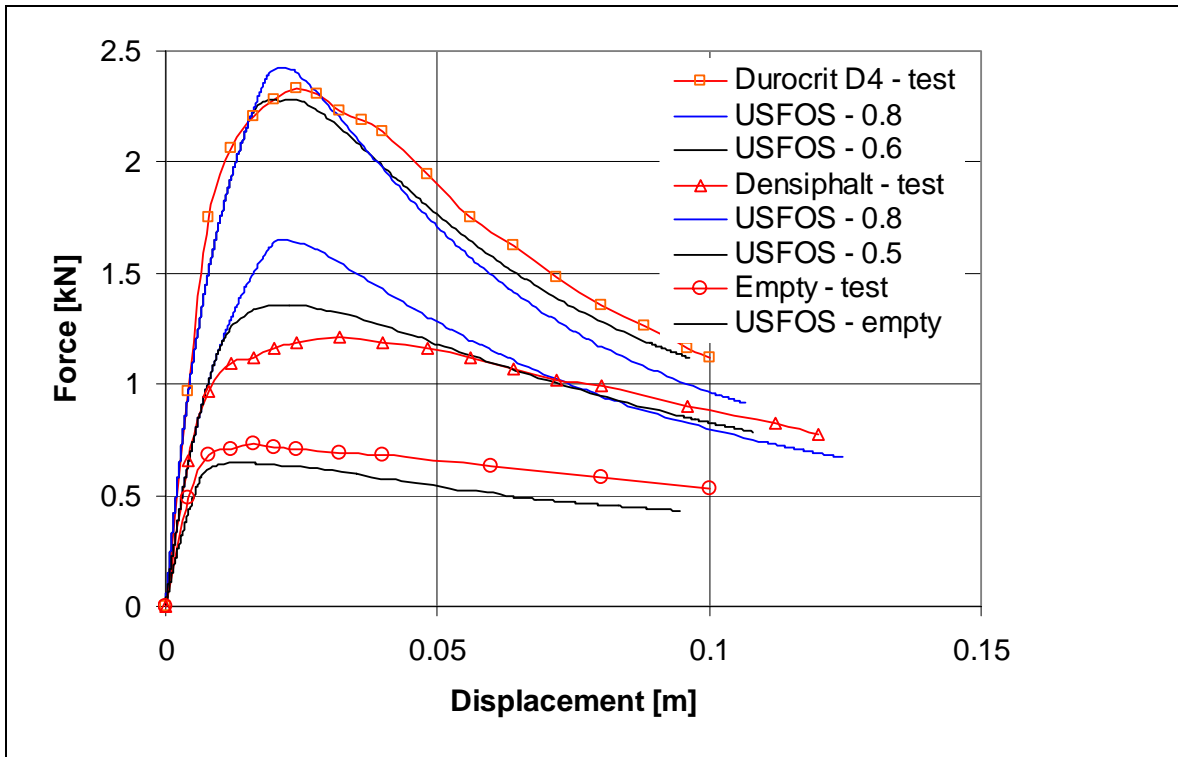
Figure 12-14 Force versus lateral displacement - tests with high yield stress and USFOS simulation
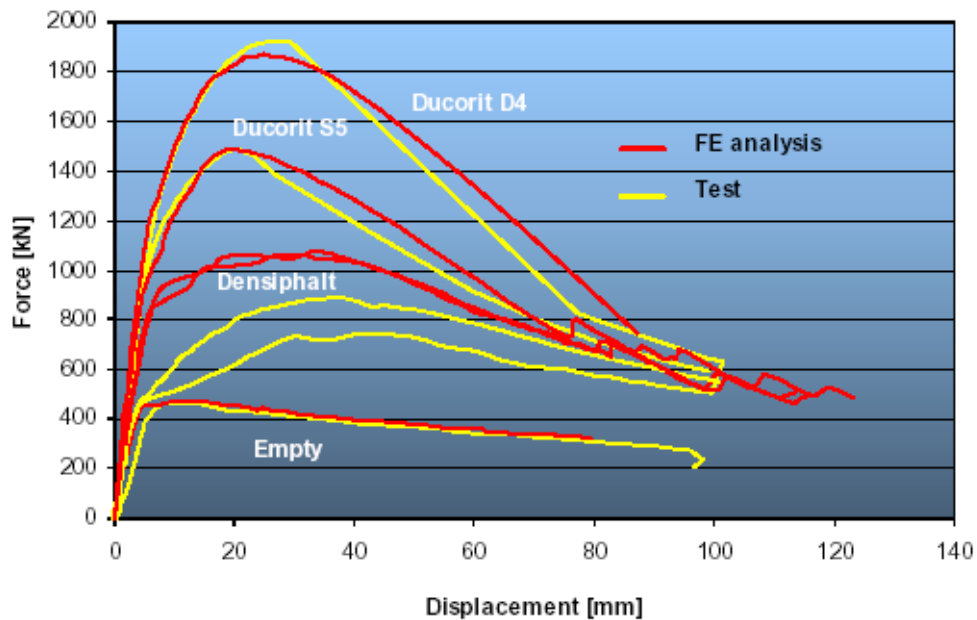

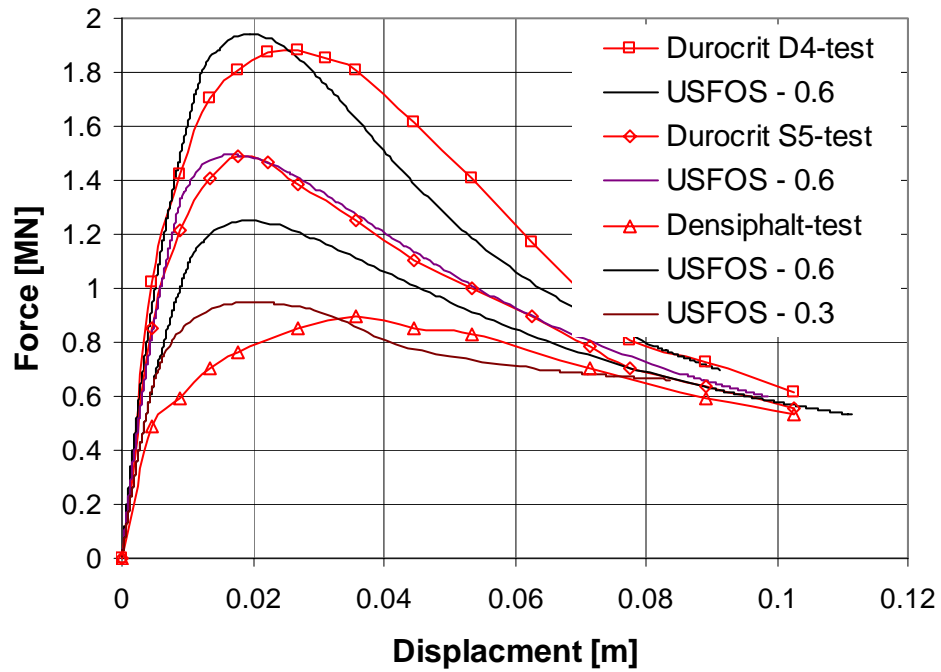**Figure 12-15 Force versus lateral displacement - tests with low yield stress, Haukaas and Yang (2002)**

Figure 12-16 Force versus lateral displacement - tests with low yield stress and USFOS simulation

12.3 ANALYSIS OF PLANE FRAME WITH GROUTED MEMBERS

The so-called Zayas frame, which is often used for verification/benchmarks studies, is used to test the effect of grouting members. The frame is shown in Figure 12-18. For details about structure dimensions it is referred to USFOS User Manuals.

The diagonal members have yield stress 248 MPa, while the grout applied is assumed to have a yield stress of 80 MPa and elastic modulus of $0.71 \cdot 10^5$ MPa.

The load versus lateral displacement at the top of the frame is depicted in Figure 12-17. When no members are grouted the ultimate load factor is approximately equal to 5 and failure takes place when the K-brace compressive members buckle, as shown in Figure 12-18. When the K-braces are grouted the axial capacity in compression exceeds the tension capacity (which is 1.12 times the steel yield force). The compression braces do not buckle and the resistance increases significantly beyond 5. Failure occurs once the upper horizontal compression member buckles. This causes an intermediate drop in the resistance, but the resistance increases again until the lower horizontal brace buckles. Afterwards the resistance is fairly constant above a load factor of 8.

When also the horizontal members (which buckled) are grouted buckling no longer takes place in the frame. It deforms by yielding of the tensile members and the resistance in the large deformation range increases continuously due to geometric stiffening effects. Yielding of tensile braces initiates at a load level of 6.5 and is identified by a drop in the stiffness of the resistance curve, see Figure 12-17.

In both cases with grouted members the resistance of the frame is dramatically increased and apparently is not limited. In practice the resistance will be limited because the tension member is subjected to significant straining. Ultimately the tension member will be subjected to fracture, implying collapse of the frame.

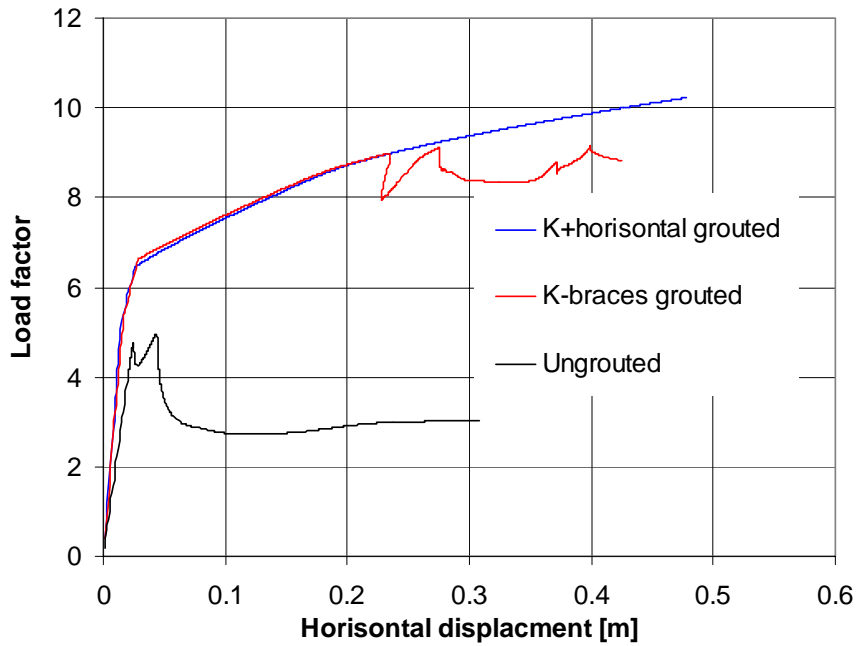**Figure 12-17 Load factor versus lateral displacement of frame**
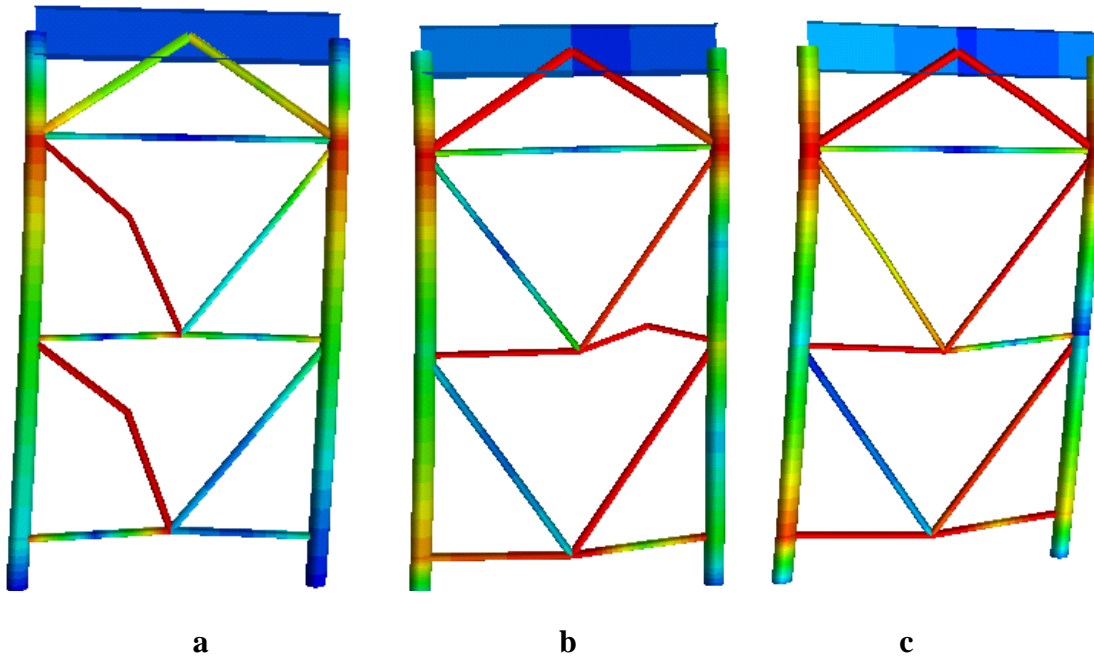

a   b   c

Figure 12-18 Displaced shape of frame with a) No grouted members b) K-braces grouted and c) K-braces and horizontals in centre grouted

12.4 CONCLUSIONS

It is verified that the model works correctly by comparing axial force-bending moment interaction relationships obtained in simulations of column buckling with analytical relationships.

The grouted column tests carried out at Chalmers University of Technology (1999) have been simulated. Very good agreement between tests results and numerical predictions are obtained when Durocrit D4 and Durocrit S5 are used as grout material. When Densiphalt is used the accuracy is fairly poor, but this is due to poor behaviour of the Densiphalt as such. A significantly better agreement may be obtained by using reduced yield stress of Densiphalt.

Best correspondence between *buckling tests* and simulations are obtained when the yield surface size is set to 0.6 of the fully plastic surface. This is smaller than the default value 0.79 for ungrouted pipes.

When *design or reassessment analysis* is performed it is recommended to introduce imperfections calibrated to column curves, e.g. to *Eurocode 3, curve a*. Then the default value 0.79 for the yield surface size may be used, i.e. no modification is necessary (GBOUND command)

13 RELATED PAPERS

USFOS General

Moan, T, Amdahl, J, Engseth, A G and Granli, T:
Collapse behaviour of trusswork steel platforms
Int. conf. on Behaviour of Offshore Structures (BOSS '85), Delft, The Netherlands, July 1985

Søreide, T.H., Amdahl, J., Granli, T. and Astrup, O.C.:
Collapse Analysis of Framed Offshore Structures
OTC 5302, Houston, Texas, May 1986.

Søreide, T.H., Amdahl, J. and Astrup, O.C.:
Progressive Collapse Analysis of Offshore Deck Structures
International Conference on Steel Structures - Recent Research Advances and their
Applications to Design, Budva, Jugoslavia, September, 1986.

Søreide, T.H., Amdahl, J. and Brodtkorb, B.B.:
The Idealized Structural Unit Method on Concrete Structures
OTC 5488, Houston, Texas, April 1987.

Amdahl, J., Taby, J. and Granli, T.:
Progressive Collapse Analysis of Mobile Platforms
3rd International Symposium on Practical Design of Ship and Mobile Units, Prads '87.
Trondheim, Norway, June 22-26, 1987.

Søreide, T.H., Amdahl, J. and Rembar, H.:
The Idealized Structural Unit Method on Space Tubular Frames
The International Conference on Steel and Aluminium Structures", Cardiff, Wales, July 1987.

Amdahl, J and Hellan, Ø:
Progressive Collapse Analysis of Steel and Aluminium Structures Subjected to Fire Loads
Int. Conf. on Structural Design for Hazardous Loads - The Role of Physical Testing, Brighton,
UK, 17-19 April, 1991.

Moan, T, Amdahl, J, Granli, T and Hellan, Ø:
Collapse Behaviour of Offshore Structural Systems
2nd Int. Conf. on Advances in Marine Structures,
Dunfermline, Scotland, 21-24 May, 1991.

USFOS Design

Hellan, Ø., Moan, T. and Drange, S.O.:
Use of Nonlinear Pushover Analyses in Ultimate Limit State Design and Integrity Assessment of Jacket Structures
Int. Conf. on the bahviour of Offshore Structures, BOSS '94, Boston, July 12-15, 1994

Hellan, Ø. and Moan, T.:
Second-Order Inelastic Analyses in Ultimate Limit State design of Frame Structures
EUROSTEEL '95, Athens, Greece, May 1995

USFOS Cyclic Reassessment

Hellan, Ø, Skallerud, B, Amdahl, J and Moan, T:
Reassessment of Offshore Steel Structures: Shakedown and Cyclic Nonlinear FEM Analyses
1st Int. Conf. on Offshore and Polar Engineering - ISOPE-1991, Edinburgh, Scotland, 11-16 August, 1991

Hopperstad, O. S., Eberg, E. and Skallerud, B.:
Plastcity Models for Cyclic Behaviour of Steel Frames
Third Int. Conf. on Computational Plastcity, Barcelona, 1992

Stewart G., Moan T., Amdahl J. and Eide O.:
Nonlinear Reassessment of Jacket Structures Under Extreme Cyclic Loading: Part I - Philosophy and Acceptance Criteria
12th Int. Conf. on Offshore Mech. and Arctic Engineering, OMAE '93, Glasgow, June, 1993.

Stewart G. and Tromans, P.S.:
Nonlinear Reassessment of Jacket Structures Under Extreme Cyclic Loading:
Part II - Representative Environmental Load Histories.
12th Int. Conf. on Offshore Mech. and Arctic Engineering, OMAE '93, Glasgow, June, 1993

Eberg, E., Hellan, Ø. and Amdahl, J.:
Nonlinear Re-assessment of Jacket Structures under Extreme Storm Cyclic Loading
Part III - The development of structural models for cyclic response
Proc. Offshore Mechanics and Arctic Engineering conference (OMAE), 1993, Glasgow

Hellan, Ø., Tandberg, T. and Hellevig, N.C.:
Nonlinear Re-assessment of Jacket Structures under Extreme Storm Cyclic Loading
Part IV - Case Studies on Existing North-Sea Platforms
Proc. Offshore Mechanics and Arctic Engineering conference (OMAE), 1993, Glasgow

Eide, O.I., Amdahl, J. and Skallerud B.H.
Reassessment of Jacket Structures under Extreme Cyclic Loading
Part I - Methodology - background and overview
14th Int. Conf. on Offshore Mech. and Arctic Engineering, OMAE'95, Copenhagen, June,
1995

Amdahl, J., Skallerud B.H., Eide O.I., and Johansen A.
Reassessment of Jacket Structures under Extreme Cyclic Loading
Part II - Cyclic Capacity of Tubular Members
14th Int. Conf. on Offshore Mech. and Arctic Engineering, OMAE'95, Copenhagen, June,
1995

Skallerud B.H., Eide O.I., Amdahl J. and Johansen A.
On the Capacity of Tubular T-joints Subjected to Severe Cyclic Loading
14th Int. Conf. on Offshore Mech. and ASrctic Engineering, OMAE'95, Copenhagen, June,
1995

USFOS Soil

Amdahl J. Johansen A. and Svanø G.:
Ultimate Capacity of Jack-ups Considering Foundation Behaviour
Int. Conf. on the behaviour of Offshore Structures, BOSS '94, Boston, July 12-15, 1994

USFOS Probabilistic

Amdahl, J., Leira, B. and Wu, Yu-Lin:
On the Application of a Nonlinear Finite Element Formulation in Structural Systems
Reliability.
1st IFIP Working Conference on Reliability and Optimization of Structural Systems, Aalborg,
Denmark, May 6-8, 1987.

Amdahl, J and Leira, B:
Probabilistic Identification of Failure Modes for Nonlinear Structures,
10th Int. Conf. on Offshore Mechanics and Arctic Engineering - OMAE 1991, Stavanger,
Norway, 23-28 June, 1991.

Sigurdsson G., Skallerud B., Skjong R. and Amdahl J.:
Probabilistic Collapse Analysis of Jackets
13th. Int. Conf. on Offshore Mech. and Arctic Eng., OMAE' 94, Houston, Feb. 27-March 3.,
1994

USFOS Fire

Amdahl, J and Hellan, Ø:
Progressive Collapse Analysis of Steel and Aluminium Structures Subjected to Fire Loads,
Int. Conf. on Structural Design for Hazardous Loads - The Role of Physical Testing, Brighton, UK, 17-19 April, 1991.

Amdahl, J and Eberg, E:
Progressive Collapse Analysis of Steel and Aluminium Structures Subjected to Fire Loads,
Course material "Brann og Eksplosjonssikring Offshore", Norwegian Soc of Chartered Engineers , Trondheim, Norway, 30 March -1 April, 1992.

Eberg, E, Amdahl, J, Holmås, T and Hekkelstrand, B:
Integrated Analysis of Offshore Structures Subjected to Fire,
Conf. on Structural Design against Accidental Loads - as Part of the Offshore Safety Case, London, UK, 23-24 September, 1992

USFOS Ship Collision

Amdahl, J:
Consequences of Ship Collision,
Seminar on Collide II Project - Risk Assessment - Collision of Ships with Offshore Platforms, RINA, London, UK, 24 October, 1991.

Amdahl J. and Eberg E.:
Ship Colision with Offshore Structures
2nd Eur. Conf. on Structural Dynamics, Eurodyn '93, Trondheim, June 21-23, 1993

14 REFERENCES

1   *Søreide, T H and Amdahl, J :*
        USFOS - A Computer Program for Progressive Collapse Analysis of Steel
        Offshore Structures. Theory Manual.
        SINTEF Report STF71 F88038. Trondheim, October 1988

2   *Hellan, Ø and Amdahl, J:*
        USFOS - A Computer Program for Progressive Collapse Analysis of Steel
        Offshore Structures. User's Manual.
        SINTEF Report STF71 F88039. Trondheim, December 1988

3   *Hellan, Ø, Auflem, L and Adam, J:*
        POSTFOS - A Computer Program for Interactive Presentation of USFOS
        Analysis Results. User's Manual.
        SINTEF Report STF71 F89050. Trondheim, October 1989

4   *Astrup, O C:*
        Cyclic Plasticity Modelling in Force Space.
        Dr Ing Thesis. Division of Structural Engineering, NTH, Trondheim 1988

5   *Timoshenko, S P and Woinowsky-Krieger, S:*
        Theory of Plates and Shells, 2 edition.
        McGraw-Hill, New York 1959

6   *Hilmy, S I:*
        Adaptive Nonlinear Dynamic Analysis of Three-dimensional Steel Framed
        Structures with Interactive Computer Graphics.
        Department of Structural Engineering, Report No 84-8, Cornell University

7   *Holmås, T:*
        Implementation of Tubular Joint Flexibility in Global Frame Analysis.
        Dr Ing Thesis. Report No. 87-1, Division of Structural Engineering, NTH,
        Trondheim 1987

8   *Taby, J:*
        Ultimate and Post-Ultimate Strength of Dented Tubular Members.
        Report No UR-86-50, Division of Marine Structures, NTH, Trondheim 1986

9   Søreide, T H:
        Ultimate Load Analysis of Marine Structures.
        TAPIR, Trondheim 1981

10   *ECCS - European Convention of Constructional Steelwork:*
        Manual on Stability of Steel Structures.
        June 1976

11   *Engseth, A:*
        Finite Element Collapse Analysis of Tubular Steel Offshore Structures
        Dr Ing Thesis, Division of Marine Structures, NTH, Trondheim 1986

12   FENRIS - Finite Element Nonlinear Integrated System. User Manual.
        Det Norske Veritas, Høvik, Norway

13   *Moan, T, Amdahl, J, Engseth, A G and Granli, T:*
        Behaviour of Offshore Structures.
        Proceedings of the 4th International Conference on Behaviour of Offshore
        Structures (BOSS '85), Delft, The Netherlands, July 1985

14   *Ueda, Y and Rashed, S M H:*
        An Ultimate Transverse Strength Analysis of Ship Structures.
        Journal of the Soc of Nav Arch of Japan, Vol 136, 1974

15   Det Norske Veritas
        Self Elevating Units
        classification notes ,note no.31.5, May 1984

16   *Bjorn Asen*
        An experimental study on steel column behavior at elevated temperatures
        Division of steel Structures, Norwegian Institute of Technology, 1985